ÇUKUROVA UNIVERSITY
INSTITUTE OF NATURAL AND APPLIED SCIENCES

PhD. THESIS

Sertaç ÖZTÜRK

SEARCH FOR NEW PARTICLES DECAYING TO DIJET IN 7 TEV PROTON-PROTON COLLISIONS AT CMS

DEPARTMENT OF PHYSICS

ADANA, 2011

ÇUKUROVA UNIVERSITY
INSTITUTE OF NATURAL AND APPLIED SCIENCES

SEARCH FOR NEW PARTICLES DECAYING TO DIJET IN 7 TEV PROTON-PROTON COLLISIONS AT CMS

Sertaç ÖZTÜRK

PhD THESIS
DEPARTMENT OF PHYSICS

We certify that the thesis titled above was reviewed and approved for the award of degree of the Doctor of Philosophy by the board of jury on 08/03/2011.

.... Prof.Dr. Gülsen ÖNENGÜT SUPERVISOR	.... Prof.Dr. Ayşe POLATÖZ MEMBER	.... Prof.Dr. Sefa ERTÜRK MEMBER
.... Prof.Dr. Aysel KAYIŞ TOPAKSU MEMBER	.... Asst.Prof.Dr. Nuri EMRAHOĞLU MEMBER	

This PhD Thesis is performed in Department of Physics of Institute of Natural and Applied Sciences of Cukurova University
Registration Number:

Prof.Dr. İlhami YEĞİNGİL
Director
Institute of Basic and Applied Sciences

To my mother Lebabe, my beloved wife Filiz and my adorable daughter Derin Mavi.

ABSTRACT

PhD. THESIS

SEARCH FOR NEW PARTICLES DECAYING TO DIJET IN 7 TEV PROTON-PROTON COLLISIONS AT CMS

Sertaç ÖZTÜRK

UNIVERSITY OF ÇUKUROVA
INSTITUTE OF NATURAL AND APPLIED SCIENCES
DEPARTMENT OF PHYSICS

Supervisor: Prof.Dr. Gülsen ÖNENGÜT
Year: 2011, Pages: 132
Jury : Prof.Dr. Gülsen ÖNENGÜT
Prof.Dr. Ayşe POLATÖZ
Prof.Dr. Sefa ERTÜRK
Prof.Dr. Aysel KAYIŞ TOPAKSU
Asst.Prof.Dr. Nuri EMRAHOĞLU

This thesis presents a measurement of the dijet invariant mass spectrum and search for new particles decaying to dijets at CMS in 7 TeV pp collisions using data corresponding to an integrated luminosity of 2.875 pb^{-1}. The measured dijet mass distribution is compared to QCD prediction from PYTHIA . It is required the pseudorapidity separation of the two jets to satisfy $|\Delta\eta| < 1.3$ with each jet inside the region of $|\eta| < 2.5$. The observed dijet mass spectrum is fitted by a smooth function to search for dijet resonances. Since there is no evidence for dijet resonances, the upper limits at 95% Confidence Level (C.L.) on the resonance cross section are set. These generic cross section limits are compared with theoretical predictions for the cross section for several models of new particles: string resonances, axigluons, colorons, excited quarks, E_6 diquarks, Randall-Sundrum gravitons, W' and Z'.

It is excluded at 95% C.L. string resonances in the mass range $0.50 < M(S) < 2.50$ TeV, excited quarks in the mass range $0.50 < M(q^*) < 1.58$ TeV, axigluons and colorons in the mass ranges $0.50 < M(A) < 1.17$ TeV and $1.47 < M(A) < 1.52$ TeV, and E_6 diquarks in the mass ranges $0.50 < M(D) < 0.58$ TeV, $0.97 < M(D) < 1.08$ TeV, and $1.45 < M(D) < 1.60$ TeV. These exclusions extend previously published limits on all models.

Key Words: CMS, Jets, LHC, QCD, Excited Quark

ÖZ

DOKTORA TEZİ

7 TEV PROTON-PROTON ÇARPIŞMALARINDA CMS' TE İKİ-JETE BOZUNAN YENİ PARÇACIKLARIN ARANMASI

Sertaç ÖZTÜRK

ÇUKUROVA ÜNİVERSİTESİ
FEN BİLİMLERİ ENSTİTÜSÜ
FİZİK ANABİLİM DALI

Danışman: Prof.Dr. Gülsen ÖNENGÜT
Yıl: 2011, Sayfa: 132
Jüri : Prof.Dr. Gülsen ÖNENGÜT
Prof.Dr. Ayşe POLATÖZ
Prof.Dr. Sefa ERTÜRK
Prof.Dr. Aysel KAYIŞ TOPAKSU
Yrd.Doç.Dr. Nuri EMRAHOĞLU

Bu tezde 2.875 pb^{-1}' lik toplam ışıklılığa karşılık gelen 7 TeV' lik proton-proton çarpışma verisini kullanarak CMS' te iki-jet invariyant kütle spektrumu ölçümü ve iki-jete bozunan yeni parçacık arama sonuçları sunulmuştur. Ölçülen iki-jet kütle dağılımı PYTHIA' dan gelen QCD öngörüsü ile kıyaslanmıştır. İki jet arasındaki pseudorapidite ayrımının her bir jetin $|\eta| < 2.5$ bölgesinin içinde bulunması ile birlikte $|\Delta\eta| < 1.3$ olması gerekmektedir. Ölçülen iki-jet kütle dağılımı, iki-jet resonanslarını araştırmak için düz bir fonksiyon ile bağdaştırılmıştır.. İki-jet resonanslarının varlığına dair herhangi bir kanıt olmadığı için, 95% lik güvenirlik seviyesindeki tesir kesitlerinin üst limitleri hesaplanmıştır. Bu modellerden bağımsız jenerik tesir kesiti limitleri, yeni parçacıkları öngören bir kaç modelin tesir kesitinin teorik öngörüsü ile kıyaslanmıştır: sicim resonansı, aksigluon, koloron, uyarılmış kuark, E_6 iki-kuark, Randall-Sundrum graviton, W' ve Z'.

95% lik güvenirlik seviyesindeki sicim resonansı için dışarlama kütle aralığı $0.50 < M(S) < 2.50$ TeV, uyarılmış kuark için dışarlama kütle aralığı $0.50 < M(q^*) < 1.58$ TeV, aksigluon ve koloron için dışarlama kütle aralığı $0.50 < M(A) < 1.17$ TeV ve $1.47 < M(A) < 1.52$ TeV, ve E_6 iki-kuark için dışarlama kütle aralığı $0.50 < M(D) < 0.58$ TeV, $0.97 < M(D) < 1.08$ TeV ve $1.45 < M(D) < 1.60$ TeV' dir. Bu dışarlamalar bütün modellerdeki önceki yayınlanmış limitleri genişletmiştir.

Anahtar Kelimeler: CMS, Jetler, BHÇ, KRD, Uyarılmış Kuark

ACKNOWLEDGMENTS

I would like to thank my supervisor Gülsen Önengüt for her great encouragement and advise during my graduate studies. She always showed me the best ways for my carrier. It was a great chance for me to have her as a supervisor.

I owe a great debt of gratitude to Robert M. Harris for his extraordinary support and guidance throughout the thesis work. It was a great opportunity for me to work with him and his help and encouragement was of great value throughout this analysis.

I thank all of the members of the LPC (LHC Physics Center) at Fermilab for their help and friendship. I am grateful to Dan Green for the opportunity to come and work at Fermilab. I wish to thank Konstantinos Kousouris and Marek Zelinski for their helping to understand jets; Chiyoung Jeong, Kalanand Mishra, Jim Hirschauer, Jason St. John, Seema Sharma for their help and friendship during my visit at Fermilab. I would like to special thank to Shuichi Kunori for his guidance and help. I have learned a lot of things about HCAL from him.

I owe Yaşar Önel for his support during my graduate study; Selda Esen and Taylan Yetkin for their help and guidance with sharing their experience, and Selçuk Cihangir for his hospitality.

I would like to express my gratitude to my group at Cukurova University, Ayşe Polatöz, Eda Eşkut, Aysel Kayış Topaksu and İsa Dumanoğlu.

I thank Sefa Ertürk and Nuri Emrahoğlu for their kindly reading and evaluating my thesis.

I wish to thank to my friends and colleagues Numan Bakırcı, Hüseyin Topaklı, Salim Çerçi, Deniz Sunar Çerçi and Pelin Kurt for their support and contributions to keep my moral and motivation high.

My deepest thanks go to my mother Lebabe Yücel for her encouragement and support throughout my lifetime, my beloved wife Filiz Yüce Öztürk for her love, support and encouragement which made this journey possible, and my one year old adorable daughter Derin Mavi Öztürk for making everything more meaningful and more beautiful in my life.

CONTENTS **PAGE**

LIST OF TABLES PAGE

LIST OF FIGURES PAGE

ABBREVIATIONS

ALICE : A Large Ion Collider Experiment
ATLAS : A Toroidal LHC Apparatus
CDF : Collider Detector at Fermilab
CERN : Conceil Europeenne pour la Recherche Nucleaire
CL : Confidence Level
CMS : Compact Muon Solenoid
CTEQ : Coordinated Theoretical-Experimental project on QCD
DAQ : Data AcQusition
ECAL : Electromagnetic CALorimeter
HCAL : Hadronic CALorimeter
HF : Hadronic Forward
HLT : High Level Trigger
JES : Jet Energy Scale
JER : Jet Energy Resolution
LEP : Large Electron Positron Collider
LHC : Large Hadron Collider
LHCb : Large Hadron Collider Beauty Experiment
MC : Monte Carlo
PDF : Parton Density Function
QCD : Quantum Chromo Dynamics
QED : Quantum Electro Dynamics
SM : Standard Model

1. INTRODUCTION

The particle physics addresses the basic question; ”What is the matter made of?”. In the fifth century B.C., Democritus proposed that everything is composed of indivisible particles called ”atoms”. In the 19th century when John Dalton formulated his atomic theory. His atomic theory, stated that elements consisted of tiny particles called atoms and all atoms of an element were identical and that in particular they had the same mass. In 1897, The physicist J. J. Thomson discovered the electrons that were a component of every atom. In 1911, Ernest Rutherford showed based on the experimental results that the atom was made up of a central charge surrounded by a cloud of orbiting electrons. The discovery of the neutron, a neutral-charged particle with a mass similar to the proton, was made by James Chadwick in 1932. In 1938, Otto Hahn, Lise Meitner and Fritz Strassmann showed the result of the first experimental nuclear fission. In the 1950s, the improvement of particle accelerators and particle detectors allowed scientists to study matter at high energies. The Standard Model of particle physics was developed to explain the properties of sub-atomic particles and the forces that govern their interactions.

The first step towards the Standard Model was taken by Sheldon Glashow in 1960 by combining the electromagnetic and weak interactions. In 1967, Steven Weinberg and Abdus Salam incorporated the Higgs mechanism into Glashow’s electroweak theory, giving it its modern form. The predictions of the Standard Model have been tested with many precise measurements. The W and Z bosons were discovered experimentally at CERN in 1983, and their masses were found to be as the Standard Model predicted. The observation of gluons was done in 1979 at DESY in Hamburg. The top quark was discovered at Fermilab in 1995.

However the Standard Model is not a complete theory due to several open questions. These unanswered questions predict new physics beyond the Standard Model. There are theories that try to address these questions and they often predict extremely short-lived particles called resonances. In this thesis, the new particles decaying to two-jets (dijets) which are predicted by the theories beyond the Standard Model were investigated. These new particles were searched in dijet mass distribution. If a dijet resonance exists, it can show up as a bump in dijet mass spectrum.

Chapter 2 gives detailed information on the theoretical motivation behind this study. First, the jet production in the Standard Model will be covered and then the dijet resonance models will be introduced. Brief overviews of the LHC and CMS detector are given in Chapter 3. Then jet reconstruction methods in the CMS experiment are introduced in Chapter 4. The measurement of dijet mass spectrum in this analysis is covered in Chapter 5. Then search new particles is given in Chapter 6.

2. THEORETICAL MOTIVATION

In this chapter theoretical motivation behind this study will be given. Firstly Standard Model will be discussed. Then Quantum Chromo Dynamis (QCD) and jet production in a hadron collision will be explained. The properties of the dijet resonance models which are considered in this study will be covered.

2.1 The Standard Model

The properties of all elementary particles and their interactions are described by the Standard Model (SM) (Nakamura, 2010; Novaes, 2000). Basically, the SM consists of two parts: particles which are quarks and leptons; interactions that are known as electromagnetic, weak and strong forces. The gauge symmetry group of the SM is the

$$SU(3) \times SU(2) \times U(1) \tag{2.1}$$

group in which the $SU(3)$ is the group of strong interaction described by the QCD and $SU(2) \times U(1)$ is the group of electroweak interaction described by Electroweak Theory. The Standard Model includes six quarks (u, d, c, s, b and t) and six leptons with spin-$1/2$ known as fermions. There is an anti-particle of each fermion. Pairs of quarks and leptons are grouped together to form a family (generation). There are three families as:

$$\begin{pmatrix} u \\ d \end{pmatrix} \quad \begin{pmatrix} c \\ s \end{pmatrix} \quad \begin{pmatrix} t \\ b \end{pmatrix}$$
$$\begin{pmatrix} e \\ \nu_e \end{pmatrix} \quad \begin{pmatrix} \mu \\ \nu_\mu \end{pmatrix} \quad \begin{pmatrix} \tau \\ \nu_\tau \end{pmatrix}$$

Fermions interact through the exchange of the gauge bosons with integer spin. The photon is the propagator of the electromagnetic force. $W^{\pm}$ and Z bosons mediate the weak interaction. The gluons are the force carriers of the strong interaction. In additional, the SM predicts a scalar boson, the Higgs (H^0), to account for the masses of the fermions and the vector bosons. The parameters of the fermions and bosons are listed in Table 2.1 and Table 2.2.

Leptons			Quarks		
Flavor	Charge	Mass (MeV)	Flavor	Charge	Mass (MeV)
ν_e	0	$< 3 \times 10^{-6}$	up	$+2/3$	$1.5 - 4.5$
e	-1	0.511	down	$-1/3$	$5 - 8.5$
ν_μ	0	< 0.19	strange	$-1/3$	$80 - 155$
μ	-1	106	charm	$+2/3$	$1000 - 1400$
ν_τ	0	< 18.2	bottom	$-1/3$	$4000 - 4500$
τ	-1	1777	top	$+2/3$	174300 ± 5100

Table 2.1. The particles of the Standard Model.

Force Carrier	Charge	Mass (GeV)
Photon (γ, Electromagnetic)	0	0
$W^\pm$ (Weak)	±1	80.423 ± 0.039
Z^0 (Weak)	0	91.1876 ± 0.0021
Photon (g, Strong)	0	0

Table 2.2. The gauge bosons of the Standard Model.

2.2 Quantum Chromodynamics

Quantum Chromodynamics (QCD) (Ellis, 1996; Narison, 2004) is the theory of strong interactions that describes the interaction of colored quarks and gluons. The QCD theory is a non-Abelian gauge theory of $SU(3)$ symmetry group. Quarks carry a color charge (red, blue or green) and antiquarks have anti-color. Gluons exchanged between quarks hold the quarks together. The gluons interact themselves, unlike the photons or the vector bosons of weak interaction. It makes the QCD theory very different from Electroweak theory which has the symmetry of the $SU(2) \times U(1)$ gauge group.

2.2.1 QCD Lagrangian

The Lagrangian of QCD can be given by (Ellis, 1996)

$$\mathcal{L}_{QCD} = \mathcal{L}_{classical} + \mathcal{L}_{gauge-fixing} + \mathcal{L}_{ghost}. \tag{2.2}$$

The expression for the classical Lagrangian density is

$$\mathcal{L}_{classical} = -\frac{1}{4} F^{A}_{\alpha\beta} F^{\alpha\beta}_{A} + \sum_{flavours} \bar{q}_a (i \not{D} - m)_{ab} q_b. \tag{2.3}$$

These terms describe the interaction of spin-$\frac{1}{2}$ quarks of mass m and massless spin-1 gluons. $F^{A}_{\alpha\beta}$ is the field strength tensor derived from the gluon filed A^{A}_{α},

$$F^{A}_{\alpha\beta} = [\partial_\alpha A^{A}_{\beta} - \partial_\beta A^{A}_{\alpha} - g f^{ABC} A^{B}_{\alpha} A^{C}_{\beta}], \tag{2.4}$$

and the indices A, B, C run over the eight color degrees of freedom of the gluon field. The g factor in Eq.2.4 is the coupling constant that determines the strength of interaction between colored quanta and f^{ABC} $(A, B, C = 1, ..., 8)$ are the structure constants of the $SU(3)$ group. The quark field q_a are in the triplet representation of the colored group, $(a = 1, 2, 3)$ and D is the covariant derivative. The covariant derivative acting on the triplet and the octet fields takes the form

$$(D_\alpha)_{ab} = \partial_\alpha \delta_{ab} + ig(t^{C} A^{C}_{a})_{ab} \tag{2.5}$$

$$(D_\alpha)_{AB} = \partial_\alpha \delta_{AB} + ig(T^{C} A^{C}_{a})_{AB} \tag{2.6}$$

where t and T are 3×3 matrices. There are 8 such matrices, and therefore there are 8 gluons. The symbols f are defined by

$$[t^A, t^B] = if^{ABC}t^C \tag{2.7}$$

$$[T^A, T^B] = if^{ABC}T^C \tag{2.8}$$

$$(T^A)_{BC} = -if^{ABC}. \tag{2.9}$$

The $SU(3)$ color matrices obey the following relations (Ellis, 1996):

$$\sum_A t^A_{ab}t^A_{bc} = C_F\delta_{ac}, \qquad C_F = \frac{N^2-1}{2N} = \frac{4}{3} \tag{2.10}$$

$$C_F = \frac{N^2-1}{2N} = \frac{4}{3} \tag{2.11}$$

$$Tr(T^C T^D) = \sum_{A,B} f^{ABC}f^{ABD} = C_A\delta^{CD} \tag{2.12}$$

$$C_A = N = 3. \tag{2.13}$$

Perturbation theory cannot be performed with the Lagrangian of Eq.2.2 without making a choice of gauge. The choice

$$\mathcal{L}_{gauge-fixing} = -\frac{1}{2\lambda}(\partial^\alpha A^A_\alpha)^2 \tag{2.14}$$

fixes the class of covariant gauges with the gauge parameter λ. This covariant fixing term must be supplemented by a ghost Lagrangian which is given by

$$\mathcal{L}_{ghost} = \partial_\alpha \eta^{A\dagger}(D^\alpha_{AB}\eta^B) \tag{2.15}$$

where η^A is a complex scalar field.

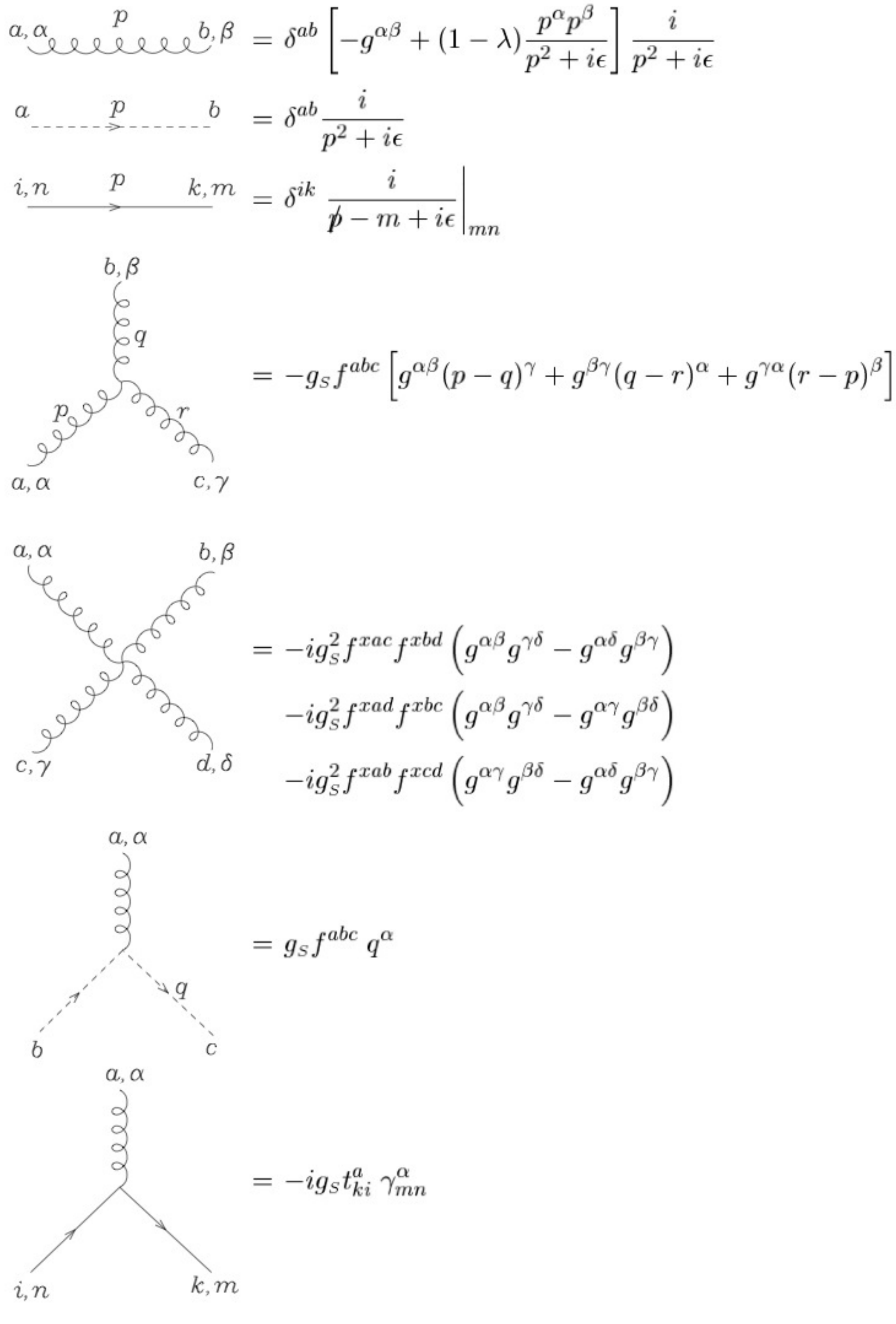

$$= \delta^{ab}\left[-g^{\alpha\beta} + (1-\lambda)\frac{p^\alpha p^\beta}{p^2+i\epsilon}\right]\frac{i}{p^2+i\epsilon}$$

$$= \delta^{ab}\frac{i}{p^2+i\epsilon}$$

$$= \delta^{ik}\left.\frac{i}{\not{p}-m+i\epsilon}\right|_{mn}$$

$$= -g_S f^{abc}\left[g^{\alpha\beta}(p-q)^\gamma + g^{\beta\gamma}(q-r)^\alpha + g^{\gamma\alpha}(r-p)^\beta\right]$$

$$\begin{aligned} &= -ig_S^2 f^{xac} f^{xbd}\left(g^{\alpha\beta}g^{\gamma\delta} - g^{\alpha\delta}g^{\beta\gamma}\right)\\ &\quad -ig_S^2 f^{xad} f^{xbc}\left(g^{\alpha\beta}g^{\gamma\delta} - g^{\alpha\gamma}g^{\beta\delta}\right)\\ &\quad -ig_S^2 f^{xab} f^{xcd}\left(g^{\alpha\gamma}g^{\beta\delta} - g^{\alpha\delta}g^{\beta\gamma}\right)\end{aligned}$$

$$= g_S f^{abc}\, q^\alpha$$

$$= -ig_S t^a_{ki}\, \gamma^\alpha_{mn}$$

Figure 2.1. QCD Feynman rules (Ellis, 1996).

2.2.2 The Running Coupling Constant

A coupling constant determines the strength of an interaction. As in the case of Quantum Electrodynamics (QED), strong coupling constant is defined as following.

$$\alpha_s = \frac{g^2}{4\pi} \tag{2.16}$$

When calculating the cross section for a certain interaction, higher-order term generally lead to divergences (infinite values). The renormalization must be implemented in the theory in order to obtain physically meaningful (finite) results. This renormalization procedure introduces a new dimensional scale, the renormalization scale (μ). The running coupling constant α_s is determined by the renormalization group equations with β-functions (Ellis, 1996).

$$\frac{\mu^2}{\alpha_s(\mu^2)}\frac{\partial\alpha_s(\mu^2)}{\partial\mu^2} = -\frac{\alpha_s(\mu^2)}{4\pi}\beta_0 - (\frac{\alpha_s(\mu^2)}{4\pi})^2\beta_1 - (\frac{\alpha_s(\mu^2)}{4\pi})^3\beta_2 + \ldots \tag{2.17}$$

where β is dependent of the number quark flavours, n_f. At leading order, retaining only coefficient β_0, α_s after solving Eq.2.17 is

$$\alpha_s(\mu^2) = \frac{1}{b\ln(\frac{\mu^2}{\Lambda^2})} \tag{2.18}$$

where

$$b = \beta/4\pi = \frac{33-2n_f}{12\pi}. \tag{2.19}$$

The normalization scale can be different for each divergent diagram. The minimal subtraction scheme ($\overline{MS}$) (Hofft, 1973) which is used to absorb the infinities that arise in perturbation calculations beyond leading order, requires the constant μ for all diagrams and usually $\mu \propto Q$. Q is the magnitude of momentum transferred in the interaction. QCD coupling constant is given by

$$\alpha_s(Q^2) = \frac{12\pi}{(33 - 2n_f)\ln(\frac{Q^2}{\Lambda^2})} \tag{2.20}$$

where

$$\Lambda^2 = \mu^2 exp(\frac{-12\pi}{(33 - 2n_f)\alpha_s(\mu^2)}). \tag{2.21}$$

At sufficiently short distances or large exchanges of momentum, high values of Q^2, α_s becomes arbitrarily small. This is called ”asymptotic freedom”. This indicates that QCD asymptotically converges to zero at high energies or short distances. When $Q^2 \to \infty$, quarks become free particles.

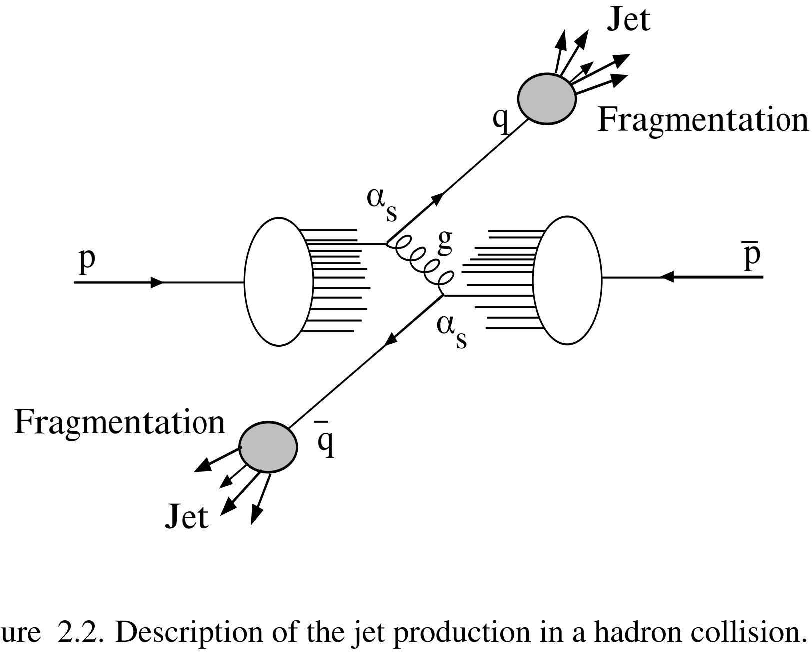

Figure 2.2. Description of the jet production in a hadron collision.

While the coupling strength decreases with Q^2, the color force increases with the distance between quarks. When two quarks are separated, a new quark-antiquark pair (a meson) spontaneously is created from vacuum.This phenome is called color confinement in QCD theory. This process of additional quark-antiquark pairs creation by the color force and the reorganization of quarks into hadrons is called ”hadronization” or ”fragmentation”. The tight cone of particles created by hadronization of a single quark is called as a ”Jet” (Fig.2.2).

2.2.3 Parton Distribution Functions

According to Quark-Parton Model, an energetic hadron consists of three valence quarks which carry its quantum numbers and a neutral sea of gluons and virtual quark-antiquark pairs (sea quarks). The lifetime of the virtual partons are limited by the Heisenberg uncertainty principle.

These constituents carry a fraction of total hadron momentum given by parton distribution function (PDF). The function $f_i(x_i)$ is the probability for a parton, i, in the hadron carries a fraction, x_i, of the total hadron momentum. For example, if a proton travels at 3.5 TeV as in LHC, an x value of 0.1 means that the quark carries 350 GeV by itself. The parton distribution functions for the leading proton constituent is shown Fig.2.3.

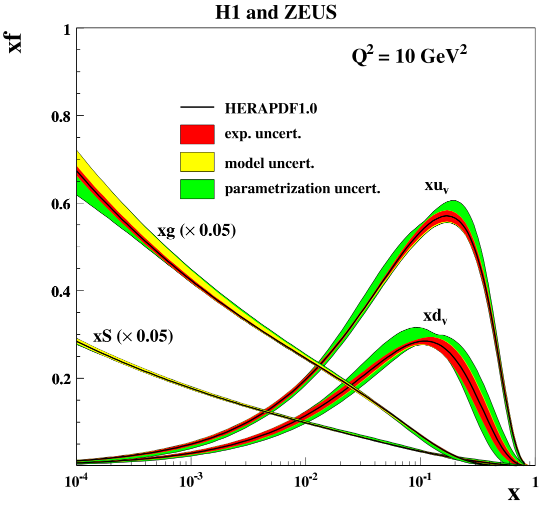

Figure 2.3. The parton distribution functions from the HERAPDF1.0 at $Q^2 = 10$ GeV^2 for gluons(g), sea quarks (S), the up valance quarks (u_μ) and the down valance quarks (d_μ). The gluon and sea quarks distributions are scaled down by a factor 20 (Petrukhin, 2010).

2.3 Jet Production in a Hadron Collision

The Feynman rules are used to calculate many predictions of QCD,such as, the probability of a given process between an initial state and a final state. This probability is called as cross section, σ. The cross section for a hard scattering process initiated by two hadrons with four-momenta P_1 and P_2 is given by (Ellis, 1996)

$$\sigma(P_1,P_2) = \sum_{i,j} \int dx_1 dx_2 f_i(x_1,\mu_F^2) f_j(x_2,\mu_F^2) \hat{\sigma_{ij}}(p_1,p_2,\alpha_s(\mu^2),Q^2/\mu^2). \tag{2.22}$$

where the momenta of the partons which are engaged in the hard interaction are $p_1 = x_1 P_1$ and $p_2 = x_2 P_2$, x_1 and x_2 are fraction of hadron momentum carried by interacting partons. The function $f_i(x,\mu_F^2)$ are the quark gluon parton distribution functions (PDFs) defined at a factorization scale μ_F. Q is a hard scattering scale. σ_{ij} is the short-distance (partonic) cross section for the scattering of partons of type i and j.

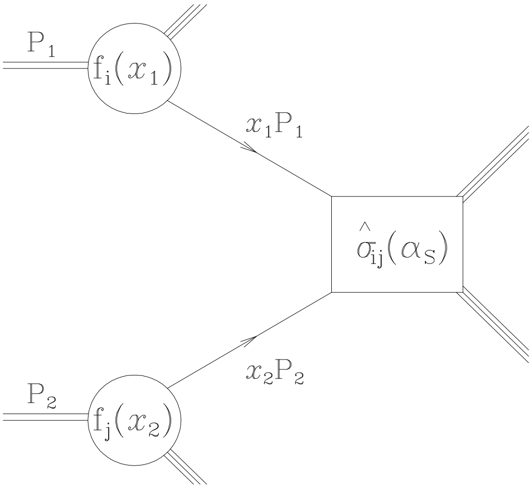

Figure 2.4. Schematic of a hard scattering process.

2.4 Two-Jet Cross Section

Two-jets events result when incoming parton from one hadron scatters from an incoming parton from the other hadron to produce two high transverse momentum partons which are observed as jets. Because of conservation of momentum, the two final-state partons have equal and opposite momenta in the center-of-mass frame. For a 2 → 2 scattering process

$$parton_i(p_1) + parton_j(p_2) \rightarrow parton_k(p_3) + parton_l(p_4) \tag{2.23}$$

described by a matrix element M, the parton cross section is given by (Ellis, 1996)

$$\frac{E_3E_4d^6\hat{\sigma}}{d^3p_3d^3p_4} = \frac{1}{1\hat{s}}\frac{1}{16\pi^2}\overline{\sum}|M|^2\delta^4(p_1+p_2-p_3-p_4) \tag{2.24}$$

where $\overline{\sum}$ is the average and sum over the initial an final state spins and colours. Fig.2.5 shows diagrams of jet production. At leading-order level, matrix elements squared are given in Table2.3, where $\hat{s} = (p_1+p_2)^2$, $\hat{t} = (p_1-p_3)^2$ and $\hat{u} = (p_2-p_3)^2$.

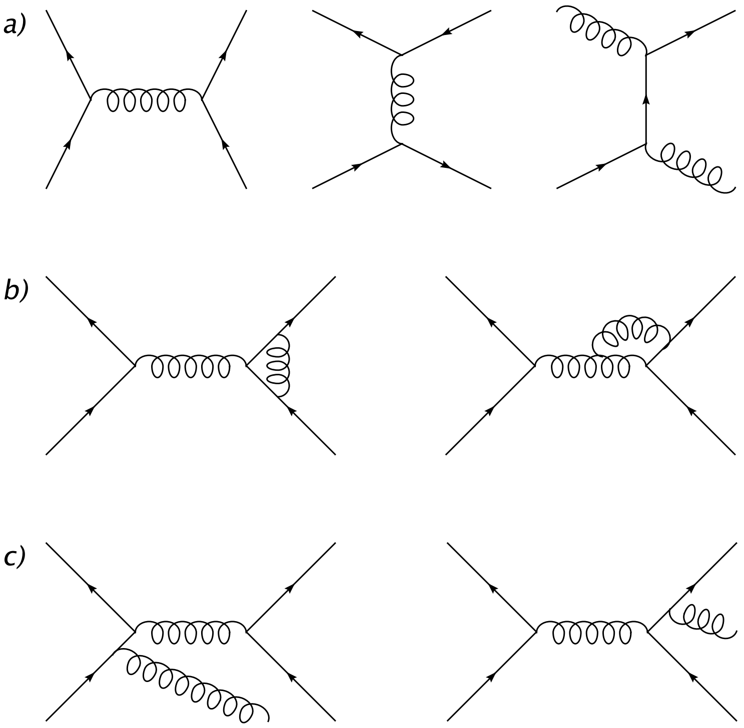

Figure 2.5. Feynman diagrams which contribute to jet production. (a) Leading order (LO) diagrams, (b) next-to-leading order (NLO) diagrams with virtual gluon loops, (c) NLO diagrams with initial state radiation (ISR) and final state radiation (FSR).

Process	$\overline{\sum}\|M\|^2/g^4$
$qq' \rightarrow qq'$	$\frac{4}{9}\frac{\hat{s}^2+\hat{u}^2}{\hat{t}^2}$
$q\bar{q}' \rightarrow q\bar{q}'$	$\frac{4}{9}\frac{\hat{s}^2+\hat{u}^2}{\hat{t}^2}$
$qq \rightarrow qq$	$\frac{4}{9}(\frac{\hat{s}^2+\hat{u}^2}{\hat{t}^2}+\frac{\hat{s}^2+\hat{t}^2}{\hat{u}^2})-\frac{8}{27}\frac{\hat{s}^2}{\hat{u}\hat{t}}$
$q\bar{q} \rightarrow q'\bar{q}'$	$\frac{4}{9}\frac{\hat{t}^2+\hat{u}^2}{\hat{s}^2}$
$q\bar{q} \rightarrow q\bar{q}$	$\frac{4}{9}(\frac{\hat{s}^2+\hat{u}^2}{\hat{t}^2}+\frac{\hat{t}^2+\hat{u}^2}{\hat{s}^2})-\frac{8}{27}\frac{\hat{u}^2}{\hat{s}\hat{t}}$
$q\bar{q} \rightarrow gg$	$\frac{32}{27}\frac{\hat{t}^2+\hat{u}^2}{\hat{t}\hat{u}}-\frac{8}{3}\frac{\hat{t}^2+\hat{u}^2}{\hat{s}^2}$
$gg \rightarrow q\bar{q}$	$\frac{1}{6}\frac{\hat{t}^2+\hat{u}^2}{\hat{t}\hat{u}}-\frac{3}{8}\frac{\hat{t}^2+\hat{u}^2}{\hat{s}^2}$
$gq \rightarrow gq$	$-\frac{4}{9}\frac{\hat{s}^2+\hat{u}^2}{\hat{s}\hat{u}}+\frac{\hat{s}^2+\hat{u}^2}{\hat{t}^2}$
$gg \rightarrow gg$	$\frac{9}{2}(3-\frac{\hat{t}\hat{u}}{\hat{s}^2}-\frac{\hat{s}\hat{u}}{\hat{t}^2}-\frac{\hat{s}\hat{t}}{\hat{u}^2})$

Table 2.3. Matrix element fot 2 → 2 parton subprocess (Ellis, 1996).

The result for two-jet inclusive cross section from a particular combination of incoming (i, j) and outgoing (k, l) partons is written using Eq.2.24;

$$\frac{d^3\sigma}{dy_3 dy_4 dp_T^2} = \frac{1}{16\pi^2 s}\sum_{i,j,k,l=q,\bar{q},g}\frac{f_i(x_1,\mu^2)}{x_1}\frac{f_j(x_2,\mu^2)}{x_2}\overline{\sum}|M(ij \rightarrow kl)|^2\frac{1}{1+\delta_{kl}} \tag{2.25}$$

where the $f_i(x,\mu^2)$ are the distributions for partons of type i ($i = u,\bar{u},d,\bar{d},g,...,etc.$), estimated at momentum scale μ, with rapidity of outgoing partons; y_3, y_4. The momentum fractions x_1, x_2 are

$$x_1 = \frac{1}{2}x_T(e^{y_3}+e^{y_4}), \qquad x_2 = \frac{1}{2}x_T(e^{-y_3}+e^{-y_4}) \tag{2.26}$$

where $x_T = 2p_t/\sqrt{s}$. The laboratory rapidity ($\bar{y}$) of the two parton system and the equal and opposite rapidities ($\pm y^*$) of the two jets in the parton-parton centre-of-mass system are given in terms of the observed rapidities by

$$\bar{y} = (y_3+y_4)/2, \qquad y^* = (y_3-y_4)/2. \tag{2.27}$$

For a massless parton the centre-of-mass scattering angle θ^* is given by

$$\cos\theta^* = \frac{p_z^*}{E^*} = \frac{\sinh y^*}{\cosh y^*} = \tanh(\frac{y_3 - y_4}{2}), \tag{2.28}$$

and the longitudinal momentum fraction of incoming partons x_1 and x_2 are given by

$$x_1 = x_T e^{\hat{y}} \cosh y^*, \quad x_2 = x_T e^{-\hat{y}} \cosh y^*, \quad \hat{y} = \frac{1}{2} ln(\frac{x_1}{x_2}). \tag{2.29}$$

$\hat{t}$ and $\hat{u}$ as a function of $\hat{s}$ and the center-of-mass scattering angle are written as

$$\hat{t} = -\frac{1}{2}\hat{s}(1 - \cos\theta^*), \qquad \hat{u} = -\frac{1}{2}\hat{s}(1 + \cos\theta^*). \tag{2.30}$$

Rapidity and pseudorapidity are identical with neglecting parton masses and determined by the following equation.

$$y = -log(tan\frac{\theta}{2}). \tag{2.31}$$

2.5 Dijet Resonances Models

The Standard Model is the current theory of quarks and leptons and their electromagnetic, weak, and strong interactions. However, it is not a complete theory due to unanswered questions, such as: Why do quarks come in different flavors? Why are the quarks arranged in generations? Why are there four different forces? How do we unify gravitation with the other forces? Why is gravity so weak?

There are new theories that try to address these questions and they often predict extremely short-lived particles called resonances. These particles are produced as narrow resonances, X, decaying to dijet as illustrated in Fig.2.6. The properties of the models which are considered in this thesis are summarized in Table 2.4.

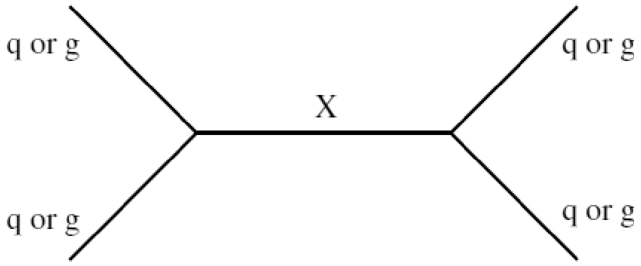

Figure 2.6. Feynman diagram of dijet resonance.

Model Name	X	Color	J^P	$\Gamma/(2M)$	Chan
Excited Quark	q*	Triplet	$1/2^+$	0.02	qg
E_6 Diquark	D	Triplet	0^+	0.004	qq
Axigluon	A	Octet	1^+	0.05	$q\bar{q}$
Coloron	C	Octet	1^-	0.05	$q\bar{q}$
RS Graviton	G	Singlet	2^+	0.01	$q\bar{q}$, gg
Heavy W	W'	Singlet	1^-	0.01	$q\bar{q}$
Heavy Z	Z'	Singlet	1^-	0.01	$q\bar{q}$
String	S	mixed	mixed	$0.003-0.037$	$qg, q\bar{q}, gg$

Table 2.4. Properties of some resonance models.

Axigluons (Bagger, 1998) or colorons (Chivikula, 1996) are the consequence of an additional color interaction. Compositeness explains the reason behind quark families by proposing a composite structure for quarks and postulates the existence of excited quarks (Baur, 1990). Grand unified theories address the question why there are different forces and require new heavy Z and W bosons. The unification of gravity with other fundamental forces is generally deal with by string theories. Some superstring models predict that at low energies the SM originates from the E_6 gauge group that contains diquarks (Hewett, 1989). The theory of extra dimensions attempts to explain the reason why gravity is so weak. It postulates that the strength of gravity is reduced by leaking into an extra dimension and predicts a new particle called Randall-Sudrum graviton (Randall, 1999), with coupling $k/M_{PL} = 0.1$. The model of string resonances is Regge excitations of the quarks and gluons in open string theory, which includes resonances in three parton-parton channels (predominantly qg at LHC but also some $q\bar{q}$ and gg) with multiple spin states and quantum numbers (Anchordoqui, 2008).

More details about few of these models will be briefly discussed in the following sections.

2.5.1 Excited Quark

Quarks are the fundamental objects without internal structure in the SM. There are three generations of fermions and it looks like a periodic table of atoms. It is suggested that quark may not be a fundamental particle. Compositeness explains the reason behind quark families by proposing a composite structure for quarks and postulates the existence of excited quarks. Spin and isospin of the excited quark are set to $1/2$ to limit the number of parameters. The assignment of left and right-handed components to isodoublets for the first generation as

$$\begin{bmatrix} u \\ d \end{bmatrix}_L , \quad \begin{matrix} u_R \\ d_R \end{matrix} \begin{bmatrix} u^* \\ d^* \end{bmatrix}_L , \begin{bmatrix} u^* \\ d^* \end{bmatrix}_R \tag{2.32}$$

allows for nonzero masses prior to $SU(2) \times U(1)$ symmetry breaking. The coupling of excited fermion states f^* to gluons, γ, $W^{\pm}$ and Z is given by the Lagrangian (Baur, 1990)

$$\mathcal{L}_{gauge} = \bar{f}^* \gamma^{\mu} [g_s \frac{\lambda^a}{2} G^a_{\mu} + g \frac{\tau}{2} W_{\mu} + g' \frac{Y}{2} B_{\mu}] f^* \tag{2.33}$$

The weak hypercharge Y of the excited states is -1 and $\frac{1}{3}$ in the lepton and quark sector respectively; $g_s, g = \frac{e}{\sin\theta_W}$ and $g' = \frac{e}{\cos\theta_W}$ are the strong and electroweak gauge couplings. G^a_{μ}, W_{μ} and B_{μ} describe the gluon, $SU(2)$ and $U(1)$ gauge field. Gauge bosons can also mediate transitions between left-handed (ordinary) and right-handed (excited) fermions. The effective Lagrangian describing these transitions is given by

$$\mathcal{L}_{transition} = \frac{1}{2\Lambda} \bar{f}^*{}_R \sigma^{\mu\nu} [g_s f_s \frac{\lambda^a}{2} G^a_{\mu\nu} + g f \frac{\tau}{2} W_{\mu\nu} + g' f' \frac{Y}{2} B_{\mu\nu}] f_L + H.C. \tag{2.34}$$

where $G^a_{\mu\nu}$, $W_{\mu\nu}$ and $B_{\mu\nu}$ are the field-strength tensor of the gluons, $SU(2)$ and the $U(1)$ gauge fields. f_s, f, and f' are parameters determined by composite dynamics. For a pure strong interaction these will be set to 1. Λ is the composite scale. Heavy excited fermions will decay into light fermions plus gauge bosons. For the decay of excited quark into ordinary quark and gluons the partial width is given by (Baur, 1990)

$$\Gamma(q^* \rightarrow qg) = \frac{1}{3}\alpha_s f_s^2 [\frac{m^*}{\Lambda}]^2 m^*. \tag{2.35}$$

Excited quarks can be produced in pp collisions in many different ways. One way is gluonic excitation of quark via $q+g \rightarrow q^*$. It has a large branching ratio and will produce a peak in the two jet spectrum. The cross section for gluonic excitation of quarks is given by

$$\sigma = \frac{\alpha_s \pi^2}{3\Lambda^2} f_s^2 \tau \frac{d\mathcal{L}^q g}{d\tau} \tag{2.36}$$

where

$$\tau = \frac{m^*}{s}, \tag{2.37}$$

s is the center-of-mass energy squared and $\frac{d\mathcal{L}^q g}{d\tau}$ is the quark-gluon luminosity. For simplicity Λ is identified with m^* and $f_s = f = f' = 1$. If gauge interactions are dominating, the signals for solely produced excited quarks are large transverse momentum of jj, $j\gamma$, jZ or jW pairs with an invariant mass peaking at m^*.

In this analysis the reaction of

$$q+g \rightarrow q^* \rightarrow q+g \rightarrow jet+jet \tag{2.38}$$

is considered and studied.

Decay Channel	B.R.
$u^* \to ug$	0.85
$u^* \to u\gamma$	0.02
$u^* \to uZ$	0.03
$u^* \to dW$	0.10
$d^* \to dg$	0.85
$d^* \to d\gamma$	0.005
$d^* \to dZ$	0.05
$d^* \to uW$	0.10

Table 2.5. Branching ratios for u^* and d^* (Baur, 1990).

2.5.2 Axigluon and Coloron

Axigluon

The chiral color group is $SU(3)_L \times SU(3)_R$, which is spontaneously broken to diagonal subgroup interpreted as the color $SU(3)$ of QCD. There are many different implementations of chiral color and all predict new particles. The most important model independent prediction of chiral color is a massive color octet of gauge bosons, the axigluon. The axigluon has a strong gauge coupling to all quark flavours according to the following interaction Lagrangian (Katsilieris, 1992);

$$\mathcal{L}_A = -ig_s t^a_{ij} \hat{q}^i \gamma_5 \gamma_\mu A^{\mu a} q^j, \tag{2.39}$$

where the t^a_{ij} are the usual $SU(3)$ color matrices. The axigluon cannot decay to gg because of parity conservation. The axigluon is prominently produced by sea (valence) - valence quark collisions. The width of the axigluon is given by

$$\Gamma_A = \frac{N\alpha_s M_A}{6}, \tag{2.40}$$

where M_A is mass of the axigluon, α_s is QCD coupling constant and N is the number of open decay channels. The N ranges from 6 for known quarks up to 18 for all particles.

For the axigluon production the matrix element squared averaged over initial and summed over final spins and color is given by

$$< |M(q\hat{q} \rightarrow A)|^2 >= \frac{16}{9}\pi\alpha_s(Q^2)m_A^2. \tag{2.41}$$

The branching ratio of the axigluon into two-jets includes a correction due to the top quark. When $M_A < 2M_t$, the branching ratio to light quarks (u,d,s,c,b) is 1, and when $M_A > 2M_t$ the branching ratio is given by

$$BR(A \rightarrow q\hat{q}) = \frac{1}{5+[1-(2M_t/M_A)^2]^{3/2}}. \tag{2.42}$$

Coloron

In the flavor-universal coloron model, the strong gauge group is extended to $SU(3)_1 \times SU(3)_2$. The gauge couplings are, respectively, ξ_1 and ξ_2 with $\xi_1 \ll \xi_2$ (Chivikula, 1996). The gluons interact with quarks through a general QCD coupling with strength g_3, as well as an octet of massive colorons ($C^{\mu a}$) interacting with quarks through a new QCD-like coupling (Simmons, 1997)

$$\mathcal{L} = -g_3 \cot\theta J_\mu^a C^{\mu a}, \tag{2.43}$$

where J_μ^a is the color current

$$\sum_f \hat{q}_f \gamma_\mu \frac{\lambda^a}{2} q_f, \tag{2.44}$$

and $\cot\theta = \xi_2/\xi_1$.

The colorons decay to all sufficient light quarks. If there are n flavors lighter than $M_C/2$ where M_C is the coloron mass, the decay with is given by

$$\Gamma_C \approx \frac{n}{6}\alpha_s \cot^2\theta M_c \tag{2.45}$$

where $\alpha_s = g_3^2/4\pi$. In this analysis, $\cot\theta = 1$ and coloron has the same properties with axigluon.

Axigluon and coloron production requires an antiquark in the initial state ($q\bar{q} \rightarrow A$ or C), slightly reducing the cross section compared to excited quarks.

2.5.3 E_6 Diquark

Diquarks are predicted in the framework of superstring-inspired E_6 models (Hewett, 1989). Diquarks can be produced with electromagnetic coupling from the valence quarks of the proton ($ud \rightarrow D$). The Lagrangian of E_6 diquark model is given by (Katsilieris, 1992)

$$\mathcal{L}_D = \lambda\varepsilon_{ijk}\hat{u}^{ci}\frac{1}{2}(1-\gamma_5)d^jD^k + \frac{1}{2}\lambda_c\varepsilon_{ijk}\hat{u}^i\frac{1}{2}(1-\gamma_5)d^{cj}D^{ck} + h.c \tag{2.46}$$

where λ and λ_c are Yukawa-type couplings which are expected to be reasonably small in order to keep the higher order correction under control. The Lagrangian includes the up and down quark flavours of each family. The matrix element for E_6 diquark production is given by

$$< |M(ud \rightarrow D)|^2 >= \frac{1}{6}\pi\alpha_\lambda m_D^2 \tag{2.47}$$

where $\alpha_\lambda = \lambda^2/4\pi$. The cross section for E_6 diquarks at high mass is greater than excited quark and axigluon/coloron models, because at high parton momentum the probability of finding a quark in the proton is significantly larger than the probability of finding a gluon or antiquark.

2.5.4 String Resonances

The mass scale M_s of fundamental string can be order of few TeV provided that spacetime extends into large extra dimensions. This mass determines the center of energy threshold $\sqrt{s} \geq M_s$ for production of Regge resonances. It is considered that extensions of the standard model is based on open string ending on D-branes (Anchordoqui, 2010). The most spectacular such modification would be the appearance of dijet resonances corresponding to excited string states for the LHC experiments.

The physical process behind dijet production at the LHC is 2 → 2 scattering of partons. The corresponding 2 → 2 scattering amplitudes are completely model independent. All string effects are encapsulated in these amplitudes in one form factor function of Mandelstam variables s, t, u (Anchordoqui, 2010);

$$V(s,t,u) = \frac{\Gamma(1-s/M_s^2)\Gamma(1-s/M_s^2)}{\Gamma(1+t/M_s^2)} \tag{2.48}$$

where Mandelstam variables are constrained by $s+t+u=0$. The physical content of the form factor can be written clear after using the expansion in terms of s-channel resonances with Regge excitations of $\sqrt{n}M_s$ by

$$V(s,t,u) \approx \frac{1}{s-nM_s^2} \times \frac{M_s^{2-2n}}{(n-1)!} \prod_{J=0}^{n-1} (u+M_s^2 J). \tag{2.49}$$

The first Regge excitations at level $n=1$ include excited gluons of spins $J=1,2$ and excited quarks of $J=1/2,3/2$. For s-channel scattering at a hadron collider, all these excitations contribute to produce a dijet resonance at the string scale. The contribution of each subprocess for $M_s = 2$ TeV as function of dijet invariant mass are shown in Fig.2.7.

Using the optical theorem the widths of the $n=1$ Regge excitations in a given channel may be obtained from the residue of the leading order (ignoring the finite width) total cross sections near the $n=1$ s-channel pole after dividing by the wave function factor for the external states obtained from the residue of the forward scattering amplitude

$$\frac{1}{m_s}\Gamma(\text{Initial}\to R^{(1)}\to \text{All}) = m_s^2\,\frac{\text{Res}_2[\sigma(\text{Initial}\to R^{(1)}\to \text{All})]}{\text{Res}_1[\mathcal{M}(\text{Initial}\to \text{Initial})]} \tag{2.50}$$

where $\text{Res}_k[f(s)] = f(s)(s-m_s^2)^k$ extracts s-channel the pole(s).

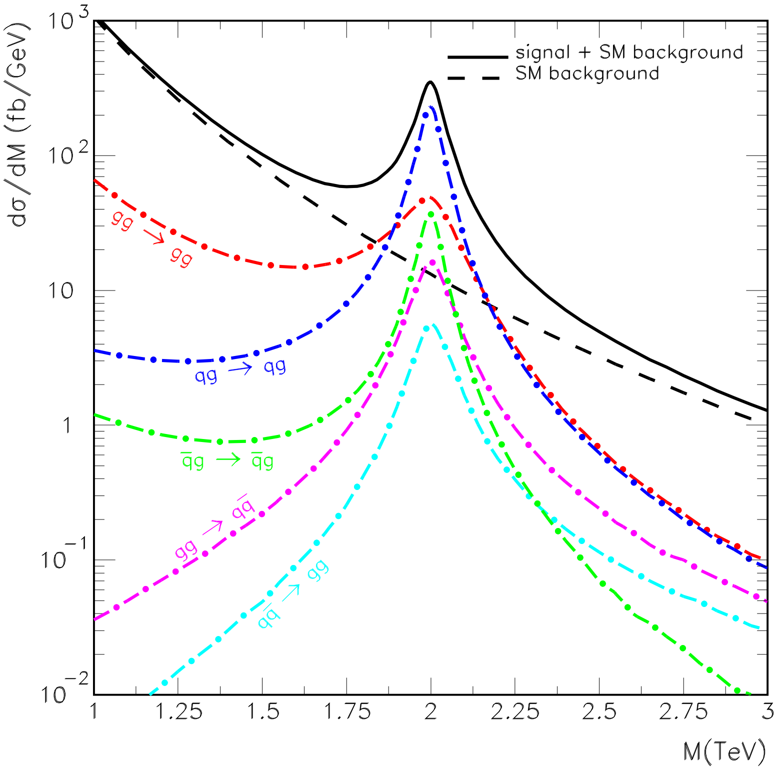

Figure 2.7. The string resonance signals are compared to SM QCD background (Anchordoqui, 2010).

The string resonance model has the largest cross section among all considered models. The cross section is about 25 times larger than q^* at 1 TeV since it is there for all the processes: $q\bar{q}$, qg, $\bar{q}g$, and gg. The string resonance decays to qg (74%), gg (13%) and $q\bar{q}$ (13%).

3. EXPERIMENTAL APPARATUS

3.1 Large Hadron Collider (LHC)

The prediction of the Standard Model of particle physics are consistent with the many precision measurements performed in the past decades. Most of these precision measurements were done by Large Electron-Positron (LEP) until 2010 and $W^{\pm}$ and Z bosons were observed in LEP. The maximum energy of circular particles is limited by the amount of energy loss due to synchrotron radiation given by

$$-\Delta E = \frac{4\pi\alpha}{3r}\beta^3\gamma^4 \tag{3.1}$$

where r is the radius of accelerator, $\beta = v/c \approx 1$ since the particles velocity is near the speed of light and $\gamma = E/mc^2$ where m is mass of the accelerated particles. According to Eq.3.1, the most efficient way to increase the center-of-mass energy is to increase the mass of the accelerated particles. Since rest mass of protons is about 2000 times greater than rest mass of electrons, the energy loss due to synchrotron radiation for protons is decreased by a factor of $(2000)^4 \approx 10^{13}$ compared to electrons.

Large Hadron Collider (LHC) is the world's largest and the most powerful proton-proton (p-p) and lead ion (Pb-Pb) collider, which was built at the European Organization for Nuclear Research (CERN) across the Swiss-French border. The LHC is located in the existing LEP tunnel between 50 and 175 m underground with 26.7 km circumference long. Two proton beams collided at a center of mass energy of 7 TeV in March 2010 and two lead ion beams collided at a center of mass energy of 2.76 TeV in November 2010 for the first time.

Before two proton beams collide in the LHC at the desired center-of-mass energy, the beams have to be accelerated by several steps. The beams start accelerating to an energy of 50 MeV by the LINAC 2. The protons with an energy of 50 MeV are transferred to the BOOSTER synchrotron and accelerated to 1.4 GeV. Then the proton beams are accelerated up to 25 GeV in the PS (Proton Synchrotron) and up to 450 GeV in the SPS (Super Proton Synchrotron). Finally, proton beams are injected into the LHC and accelerated to the energy of 3.5 TeV resulting in a center-of-mass energy of 7 TeV. The whole accelerator complex of the LHC is illustrated in Fig.3.1.

The magnetic field of 8.33 Tesla is needed to keep the proton beams on track in the LHC. To obtain this high magnetic field, super conducting magnets are operated at a temperature of 1.9 K which achieves the superfluidity of the 37 million kg of Helium cooling the NbTi windings of the magnets to reach superconductivity. The LHC has 1232 dipol magnets each of which is about 30 tonnes and 15 m long. The most important LHC parameters are listed in Table 3.1 (Bruening, 2004).

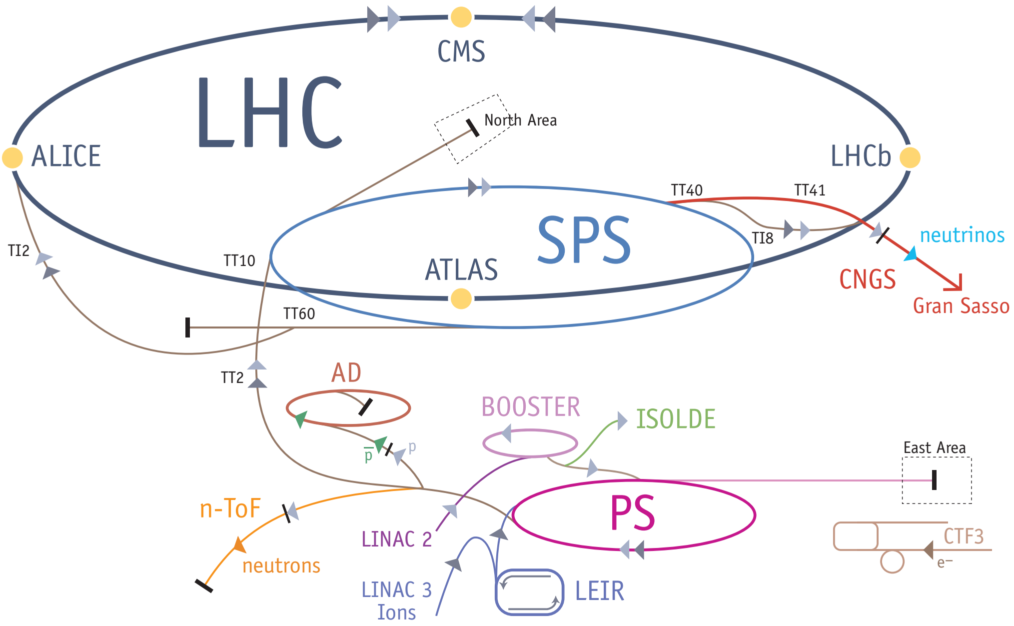

Figure 3.1. A schematic view of the CERN accelerator complex.

Since protons are not elementary particles and have a sub-structure, proton-proton collisions phenomenology are very different from lepton collisions. A proton is composed out of partons (quarks and gluons). The constituent partons that carry a fraction of total proton energy interact with each other in a collision and a fraction of total proton energy is exchanged. The effective center-of-mass energy of the hard scattering, $\sqrt{\hat{s}}$, is proportional to the fraction of momentum carried by partons, x_1 and x_2, and given by $\sqrt{\hat{s}} = \sqrt{x_1 x_2 s}$ where $\sqrt{s}$ is center-of-mass energy of the proton beams. Each collision will lead to a different type of event determined by the cross section of possible interactions because the fraction of momentum carried by interacting partons will be different. The total cross section for a hard interaction was given by Eq.2.22 in Chapter 2. The cross section for different process in pp collisions as a function of center-of-mass energy is illustrated in Fig.3.2.

Parameter	Value
Energy per proton beam	3.5 TeV
Number of bunches	2808
Number of particles per bunch	1.15×10^{11}
Bunch spacing	25 ns
RMS of bunch legth	7.55 cm
Bunch crossing rate	40 MHz
Peak luminosity	10^{34} cm^{-2}s^{-1}
Luminosity lifetime	14.9 h
Energy loss per turn	420 eV

Table 3.1. LHC parameters for pp collisions, mostly design values (except energy per proton beam and energy loss per turn).

The production rate per second for a physical process is given by

$$R = L\sigma, \tag{3.2}$$

where σ is the cross section of the physical process and L is the luminosity of the collider. The luminosity of a collider is given by

$$L = \frac{f n_1 n_2}{2\pi\sqrt{\sigma_{x,1}^2 + \sigma_{x,2}^2}\sqrt{\sigma_{y,1}^2 + \sigma_{y,2}^2}}. \tag{3.3}$$

Here, f is the collision frequency, n_i is the number of protons in bunch i, and $\sigma_{x/y,i}$ are the root mean square of the beam i in the transverse directions. The total amount of data accumulated in a time period corresponds to an integrated luminosity, $\mathcal{L}$, is defined as

$$\mathcal{L} = \int L dt \tag{3.4}$$

From Equation 3.2, the expected number of events of a physical process in a stored total amount of data is given by $N_{event} = \mathcal{L}\sigma$. It is obvious that high luminosity is needed to observe the events of the interesting physics production with small cross section like Higgs boson production.

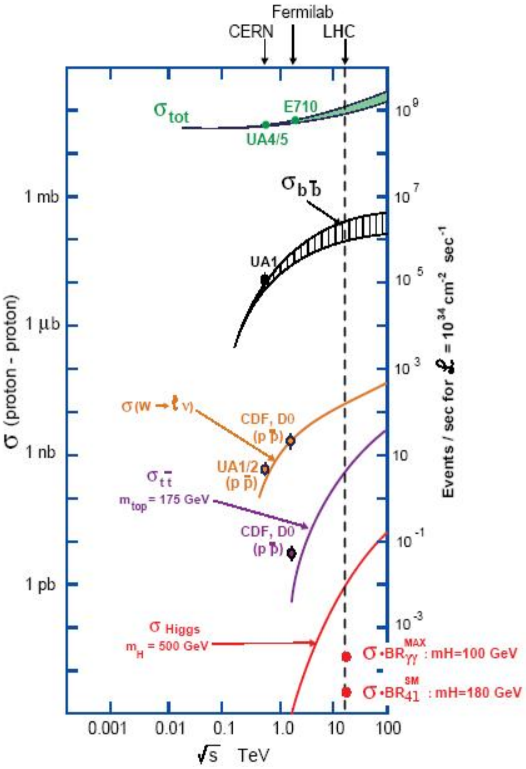

Figure 3.2. The cross section and event rate in pp collisions as a function of center-of-mass energy (Flugge, 1994).

The LHC hosts four different main detectors. A Torodial LHC Apparatus (ATLAS) and Compact Muon Solenoid (CMS) are general purpose detectors and their main goal is to search for Higgs boson which is predicted to be responsible for the electroweak symmetry breaking mechanism. Searching for new physics, such as supersymmetric particles, new massive vector bosons, extra dimensions, quark compositeness etc., at the TeV scale is an important part of CMS and ATLAS. Apart from the new phenomena search, the ATLAS and CMS physics programs aim to understand deeply already discovered Standard Model particles. The LHCb experiment studies b-quark physics and CP violation.

The LHC also includes a heavy ion physics program. The A Large Ion Collider Experiment (ALICE) is designed to study lead-lead collisions in order to observe quark-gluon plasma which is the state of hot nuclear matter. ATLAS and CMS are also planing to study both heavy ion physics and CP violation.

3.2 Compact Muon Solenoid

The Compact Muon Solenoid (CMS) is a multi purpose detector at the LHC. All three parts of the name have a certain function. The first part of the name, Compact, is used due to dimensions of the detector. The tracker and calorimeters are inside the magnet and dimensions of the CMS detector are smaller compared to ATLAS, a diameter of 15m and a length of 28.7m compared to 25m and 44m, respectively. However, weight of the CMS with 14000 tonnes is about two times heavier than ATLAS. The second part of the name is used due to excellent muon system of the detector. Muons provide very clean signatures and a part of several interesting Standard Model and beyond Standard Model physics signatures, for example, signature for the discovery of the Higgs is its golden decay to four muons, $Higgs \rightarrow ZZ \rightarrow 4\mu$. The third part of the name is used due to geometrical shape. A perspective view of the CMS detector is illustrated in Fig.3.3. The detector requirements for CMS to satisfy the aims of the LHC physics program can be summarized as following (Bayatian, 2006):

- Good muon identification and momentum resolution,
- Good charged particle momentum resolution and reconstruction efficiency in the inner tracker,
- Good electromagnetic energy resolution, good diphoton and dielectron mass resolution,
- Good E^T_{miss} and dijet mass resolution.

The CMS detector design is similar to the structure of an onion. It consists of several layers of each one which is specialized to measure and identify different classes of particles. These detector layers are shown in Fig.3.4. In the following sections each sub-detector corresponding to these layers are briefly discussed.

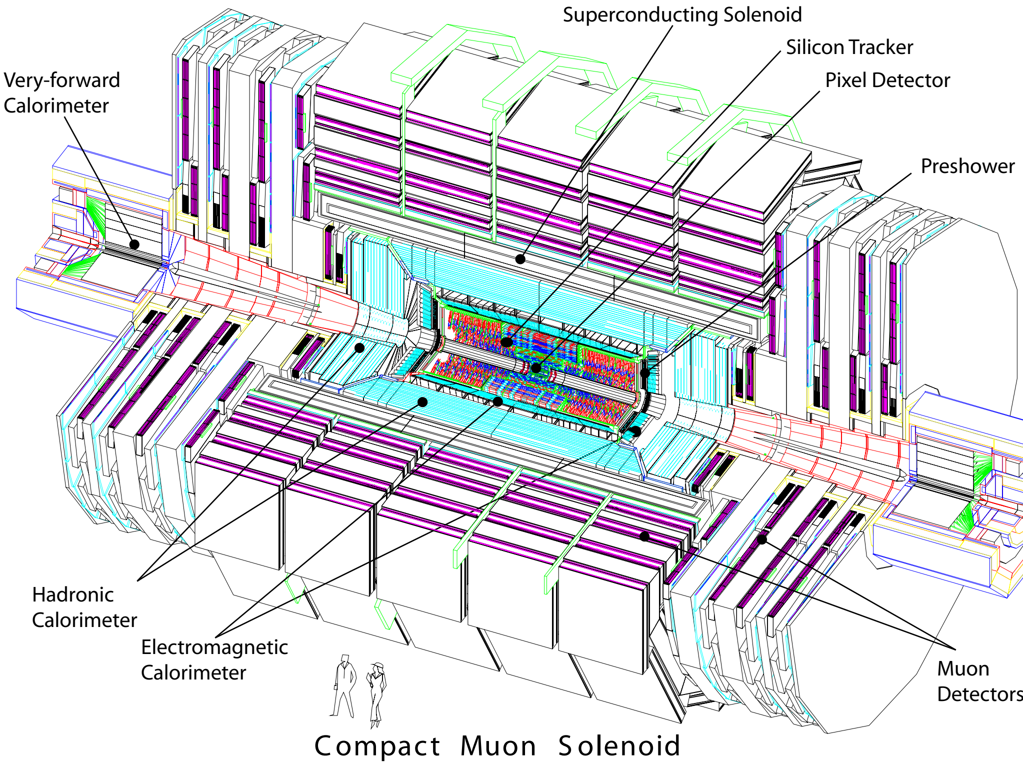

Figure 3.3. A full view of the CMS detector.

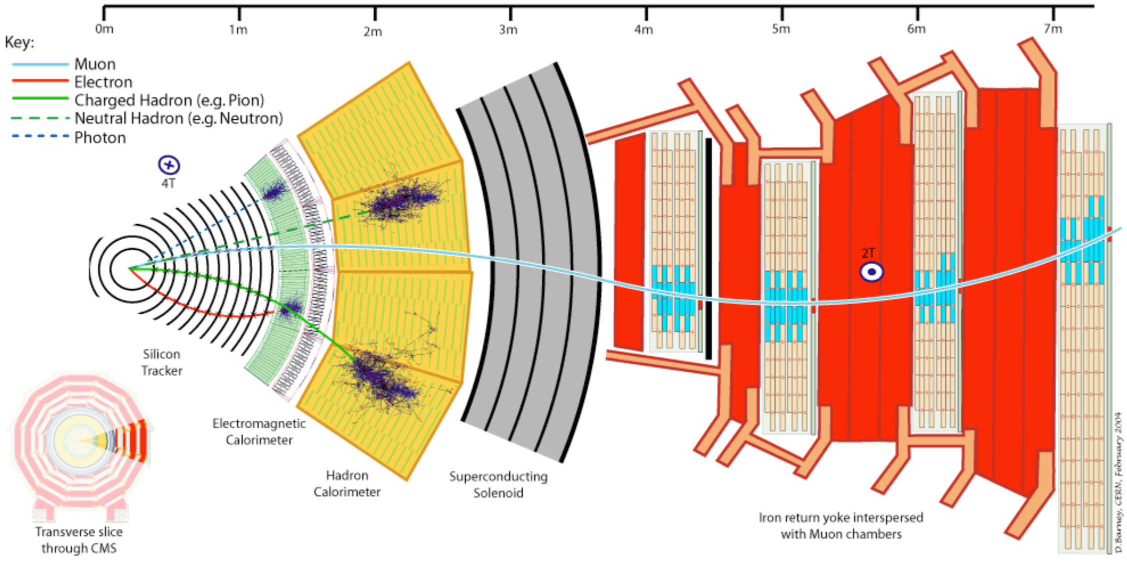

Figure 3.4. Slice through CMS showing particles incident on the different sub-detectors.

3.2.1 The Tracker

The inner tracking system of CMS is designed to provide a precise measurement of the trajectories of charged particles from the interaction point, and also precise reconstruction of secondary vertices. The tracker is used to reconstruct the paths of high-energy muons, electrons and charged hadrons, as well as to see tracks coming from the decay of very short-lived particles such as b-quark, with high momentum resolution and efficiency.

It surrounds the interaction point and has a length of 5.8 m and a diameter of 2.5 m. The CMS solenoid provides a homogeneous magnetic field of 4 T over the full volume of the tracker. A schematic drawing of the CMS tracker is shown in Fig.3.5. It comprises a silicon pixel detector with 3 barrel layers at radius between 4.4 cm and 10.2 cm and a silicon strip tracker with 10 barrel detection layers extending outwards to a radius of 1.1 m. Each system is completed by endcaps which consist of 2 disks in the pixel detector and 3 plus 9 disks in the strip tracker on each side of the barrel, extending the acceptance of the tracker up to a pseudorapidity of $|\eta| < 2.5$ (Mangano, 2009).

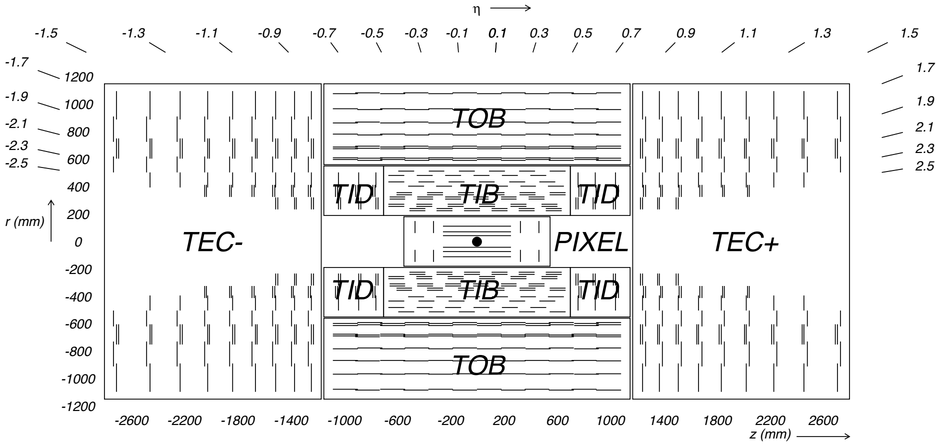

Figure 3.5. Schematic cross section through the CMS tracker. Each line represents a detector module. Double lines indicate back-to-back modules.

The Tracker Inner Barrel and Disks (TIB/TID) extend in radius up to 55 cm and and are composed of 4 barrel layers, supplemented by 3 disks at each end. The Tracker EndCaps (TEC) covers the region $22.5 < |r| < 113.5$ cm and are composed of 9 disks. The Tracker Outer Barrel (TOB) has an outer radius of 116 cm and consists of 6 barrel layers. For high momentum muon tracks (100 GeV) the transverse momentum resolution is about $1-2\%$ in the central region $|\eta| = 1.6$, beyond which it degrades due to the reduced lever arm.

The CMS tracker consists of pixel detectors at the very core of the detector dealing with the highest intensity of particles, and the silicon microstrip detectors that surround it.

3.2.1.1 The Pixel Detectors

The pixel system is the closest part of the tracking system to interaction region and contains 65 million pixels, allowing it to track the paths of particles emerging from the collision with extreme accuracy. It provides pricise tracking points in the three dimensional space with a spatial resolution in the range of 15-20 μm. The size of a pixel cell is 100×150 $\mu\mathrm{m}^2$ and the pixel detector covers a pseudorapidity range $|\eta| < 2.5$ as seen in Fig.3.6. The pixel detector is necessary for secondary vertices reconstruction from *b*-quark and tau decays and forming seed tracks for the reconstruction of outer track.

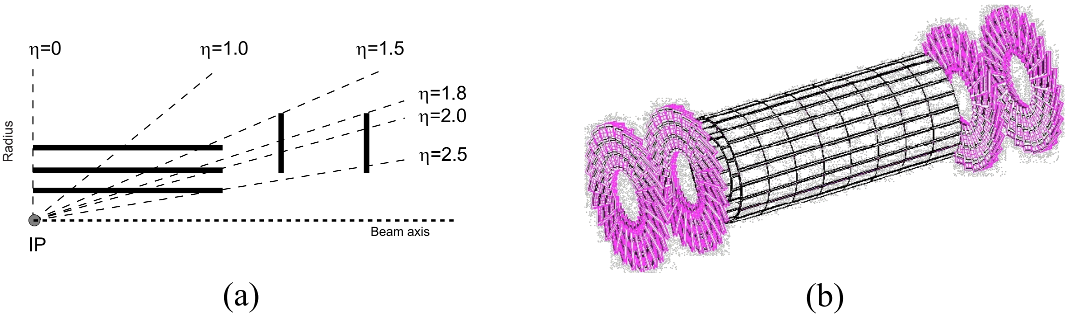

(a) (b)

Figure 3.6. Geometrical layout of the pixel detector.

The vicinity to interaction region causes a very high track rate and particle fluences which require a radiation tolerant design. A $n+$ pixel on n-substrate detector design allows operation even at very high particle fluences. The forward detectors are tilted at 20^o in a turbine-like geometry to induce charge-sharing. Due to high rate radiation environment in the CMS, the pixel detectors will have to be replaced during the time period of the experiment.

3.2.1.2 The Silicon Strip Detectors

The silicon strip tracker is composed of 15148 detector modules distributed among the four different subsystems (TIB, TID, TOB, TEC). Each module carries either one thin (320 μm) or two thick (500 μm) silicon sensors. The sensor elements in the strip tracker are single sided $p-on-n$ type silicon micro-strip sensors. After the pixels and on their way out of the tracker, particles pass through ten layers of silicon strip detectors, reaching out to a radius of 130 centimeters. The silicon detectors work in much the same way as the pixels: as a charged particle crosses the material it knocks electrons from atoms and within the applied electric field these move giving a very small pulse of current lasting a few nanoseconds.

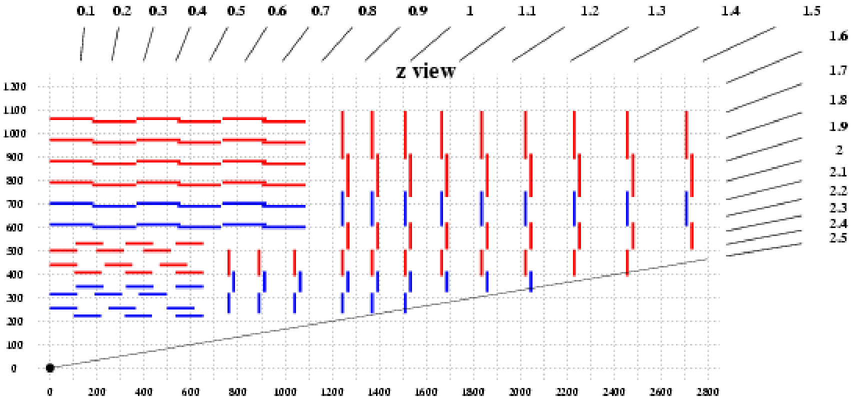

Figure 3.7. Schematic layout of the silicon microstrip detector.

3.2.2 The Calorimeters

A calorimeter is an experimental apparatus to measure the energy of particles. Most particles interact with a material and deposit their energy through creation and destruction processes. The CMS calorimeters are designed to measure the energy of photons, electrons and hadrons (jets) precisely. Basically, the CMS calorimeter system consists of two layers. The first layer, electromagnetic calorimeter, is used to measure the energy of particles which interact electromagnetically such as photons and electrons.

The second layer, hadronic calorimeter, is designed to measure the energy of strongly interacting particles, hadrons (e.g. $\pi^{\pm}$, π^{0}, K etc.). Neutrinos don't interact with matter and escape from the calorimeters. Neutrinos can be observed indirectly as an imbalanced event energy in the transverse plane. This imbalanced event energy in the transverse plane is called missing transverse energy, E_T^{miss}, and measurement of missing transverse energy plays a critical role for new physics searches, such as supersymmetry.

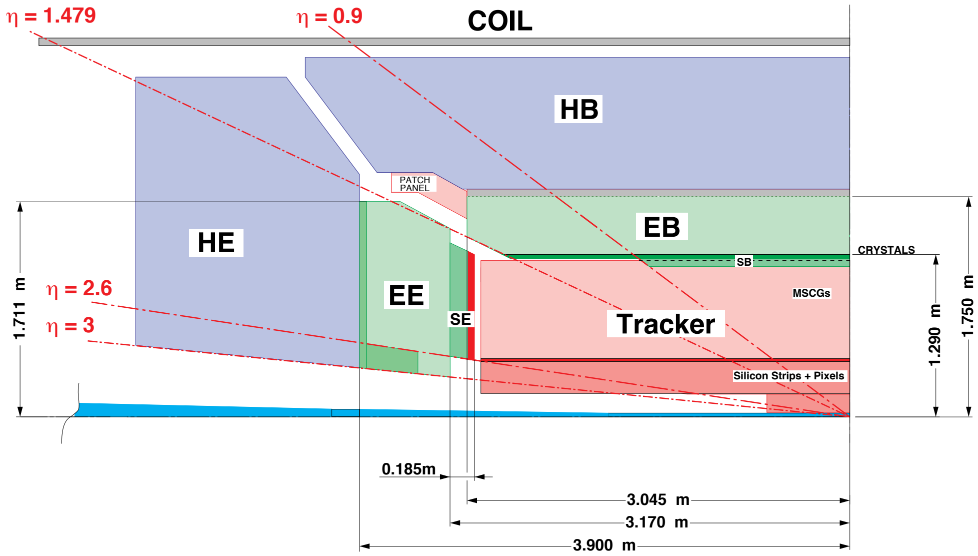

Figure 3.8. Schematic view of one quadrant of the calorimetry and tracking system.

3.2.2.1 The Electromagnetic Calorimeter

The electromagnetic calorimeter of CMS (Bayatian, 1997a) (ECAL) is a hermetic homogeneous calorimeter. It is made of 61200 lead tungstate ($PbWO_4$) crystals in the barrel part and 7324 crystals in each of the two endcaps. $PbWO_4$ crystals have high density (8.28 g/cm^3), short radiation length (0.89 cm) and small Moliere radius (2.2 cm) which allow designing a fine granularity and a compact calorimeter.

The ECAL play an essential role in the study of electroweak symmetry breaking. The search for the Higgs boson strongly rely on ECAL information by measuring the decay mode of Higgs from $H \to \gamma\gamma$ for $m_H < 150$ GeV and $H \to ZZ^*$ and $H \to WW$ for $140 < m_H < 170$ GeV.

The pseudorapidity coverage extends to $|\eta| < 3$. The transverse granularity of $\Delta\eta \times \Delta\phi = 0.0175 \times 0.0175$, corresponding to a $PbWO_4$ crystal face of 2.2×2.2 cm, is equal to Moliere radius of $PbWO_4$. In the endcaps ($1.48 < |\eta| < 3.0$), the granularity increases to a maximum value of $\Delta\eta \times \Delta\phi = 0.05 \times 0.05$. The length of a $PbWO_4$ crystal is 23 cm in the barrel region and 22 cm in the endcaps.

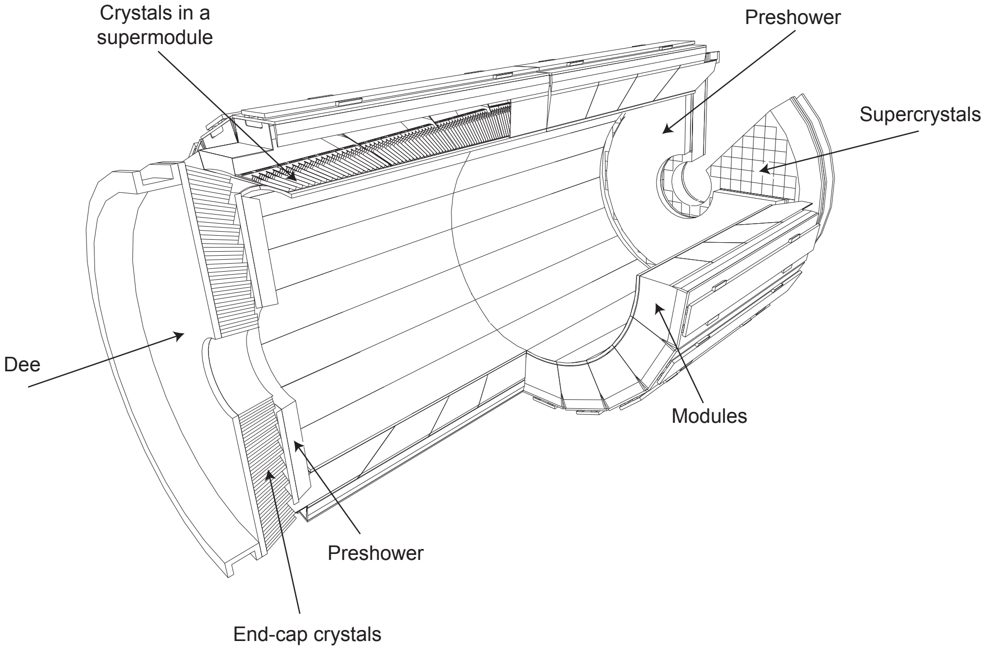

Figure 3.9. Layout of the CMS electromagnetic calorimeter.

For the energies between 25 GeV and 500 GeV, the energy resolution can be parametrized as (Chatrchyan, 2008)

$$(\frac{\sigma}{E})^2 = (\frac{S}{\sqrt{E}})^2 + (\frac{N}{E}) + C^2 \qquad (3.5)$$

where S is the stochastic term, N is the noise term and C is the constant term. The contribution to stochastic term comes from fluctuations in the shower containment. The different contributions for energy resolution are shown in Fig.3.10.

The endcap preshower covers pseudorapidity range of $1.65 < |\eta| < 2.61$. The main function of preshower detectors is to provide $\pi^0 - \gamma$ separation. The preshower detectors are placed in front of the ECAL crystals.

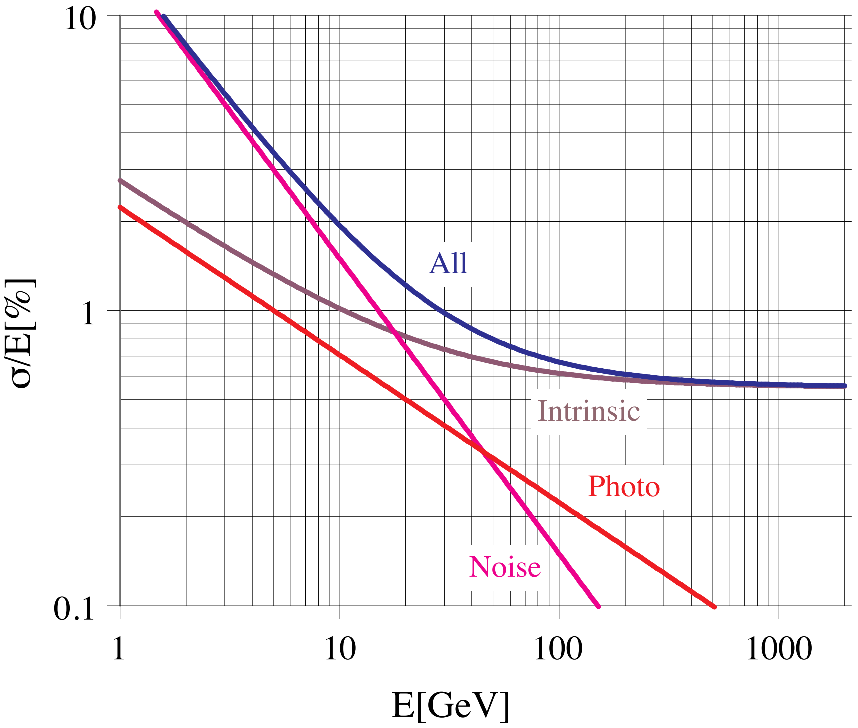

Figure 3.10. Different contributions to the energy resolution of the CMS ECAL calorimeter (Chatrchyan, 2008).

3.2.2.2 The Hadronic Calorimeter

The Hadronic calorimeter (HCAL) (Bayatian, 1997b) surrounds ECAL and measure quark, gluon and neutrino directions and energies by measuring jets and missing transverse energy together with ECAL. The determination of missing energy and jets are crucial for new particles and phenomena, such as supersymmetric partners of quarks and gluons. The HCAL consists of four sub-detectors which are shown in Fig.3.11. The hadron barrel (HB) and hadron endcaps (HE) are sampling calorimeters with scintillator as the active matter and brass as absorber. HB covers the pseudorapidity range $|\eta| < 1.3$ and is placed inside the magnetic coil. The HB is divided into two half-barrel sections (HB+ and HB-) and each section consists of 18 identical azimuthal wedges, resulting in a segmentation $\Delta\eta \times \Delta\phi = 0.087 \times 0.087$.

The hadron endcaps (HE) cover the pseudorapidity range $1.3 < |\eta| < 3.0$. Since the calorimeter is inserted into the ends of a solenoid magnet, non-magnetic absorber

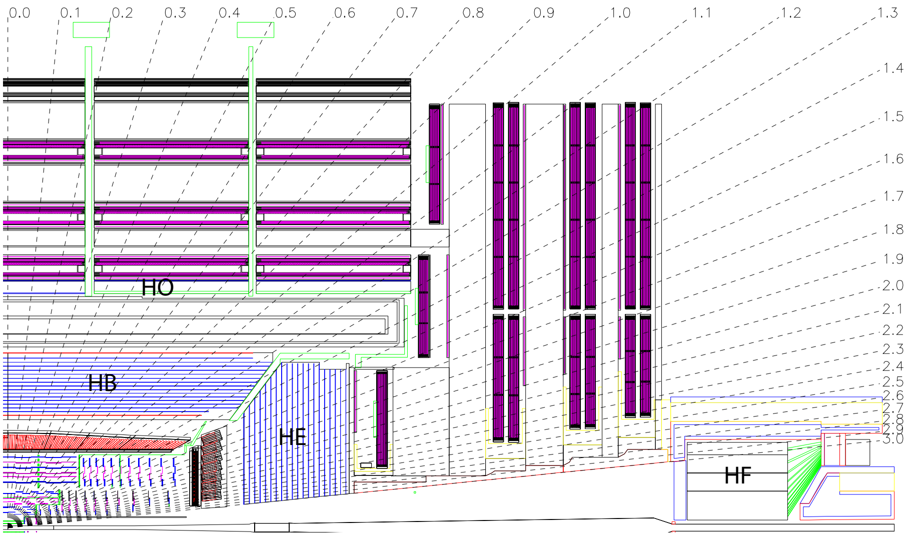

Figure 3.11. Longitudial view of the parts of CMS HCAL, hadron barrel (HB), hadron endcap (HE), hadron outher (HO) and hadron forward (HF) (Chatrchyan, 2008).

material which has a maximum number of interaction lengths to contain hadronic shower was used. The granularity of HE is $\Delta\eta \times \Delta\phi = 0.087 \times 0.087$ for $|\eta| < 1.6$ and $\Delta\eta \times \Delta\phi = 0.17 \times 0.17$ for $|\eta| \geq 1.6$.

The combination of electromagnetic barrel (EB) and hadronic barrel (HB) doesn't provide sufficient stopping power for hadron showers in the central pseudorapidity region. Thus, the hadron calorimeter is extended outside the solenoid coil with a tail catcher for $|\eta| < 1.3$. This part of the HCAL is called hadron outher calorimeter (HO). The HO is used to identify and to measure the late starting shower energy after HB.

The HF calorimeters are located 11 m away from the interaction point to cover the pseudorapidity range $3 < |\eta| < 5$. The HF is designed to improve measurement of missing transverse energy and to enable identification and reconstruction of very forward jets which are distinguishing characteristic of several important physics processes. The signal in HF is generated when a charged particle transverses a quartz fiber with a velocity greater than the speed of light, resulting in Cherenkov radiation. The particles entering the absorber of a calorimeter produce showers of particles. The embedded quartz fibers have two different lengths to differentiate between shower processes. Longer fibers (1.65 m) provide light from EM and hadronic showers in the absorber. Shorter fibers (1.43 m) contain the hadronic showers (Chatrchyan, 2008). The iron absorber with 10 nuclear interaction lengths is used. Each HF module is divided into 18 wedges. Fig.3.11 shows a cross sectional view of the HF.

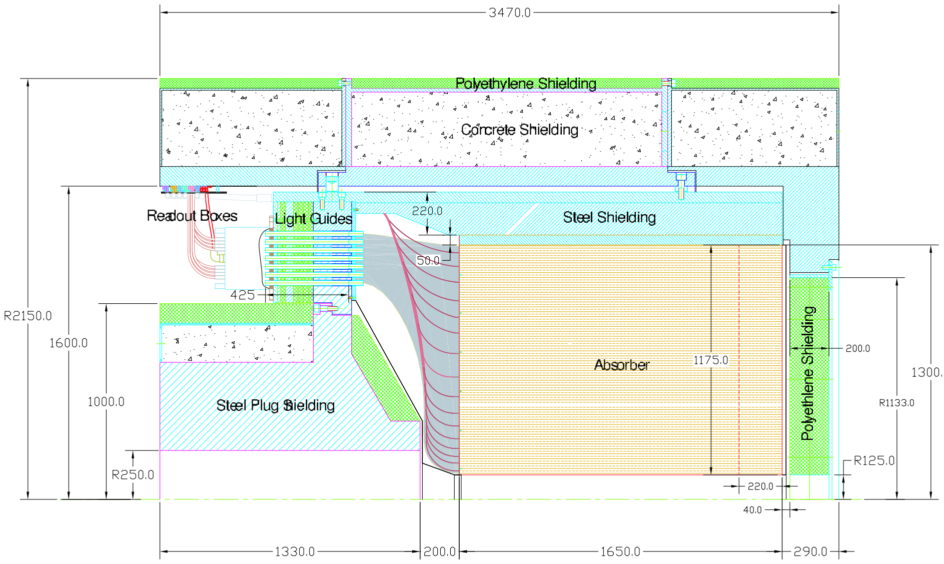

Figure 3.12. The cross sectional view of the HF calorimeter (Chatrchyan, 2008).

3.2.3 The Magnet

The magnet of the CMS detector (Bayatian, 1997c) is a superconducting solenoid with 6 m diameter and 12.5 m length, and designed to reach a 4 Tesla uniform magnetic field. The magnetic flux generated by the superconducting coil is returned via a 1.5 m thick saturated iron yoke. The yoke is divided into two main components: the barrel yoke and the endcap yoke. The barrel yoke is a 12-sided cylindrical structure. The End Cap Yoke is design to provide access to the forward muon stations.

The requirement for a good energy measurement leads naturally to the choice of a high magnetic field. A field of 4 T brings substantial benefits for the muon tracking, inner tracking and electromagnetic calorimetry. The energy of electrons measured in the calorimeter can be compared with their momenta measured in the tracker.

The transverse momentum of a charged particle, P_T, in a magnetic field is given by

$$P_T = 0.3 \times B \times R \tag{3.6}$$

where B is the magnetic field and R is the radius of curvature of the charged particle. The distance between interaction point and ECAL surface is about 1.3 m. The minimum P_T of the charged particle to reach ECAL surface is $P_T = (0.3 \times 4 \times 1.3)/2 \approx 0.8$ GeV in CMS detector.

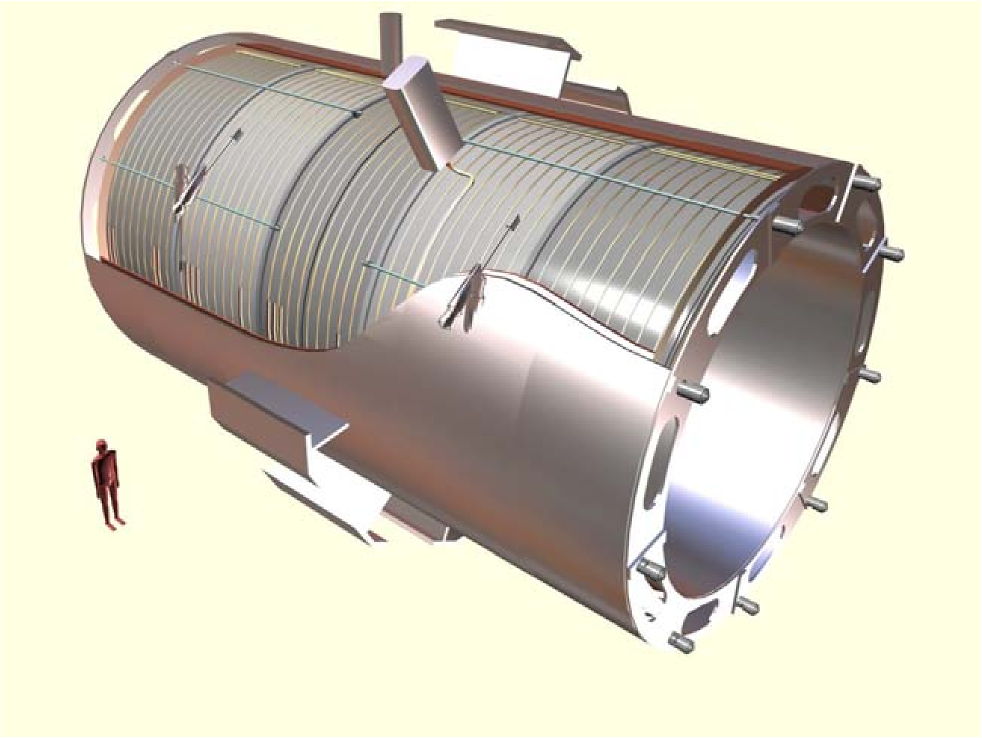

Figure 3.13. The CMS superconducting magnet.

3.2.4 The Muon System

Muon detection is the most powerful tool to detect interesting events, such as the signature for the discovery of the Higgs decaying into ZZ or ZZ^* which in turn decays into four charged leptons. If the leptons are muons, the best mass resolution can be achieved since muons are less affected than electrons by radiative losses in the tracker material. Possible extensions of the Standard Model predict the other gauge bosons, such as heavy

W and heavy Z. The discovery search relies mostly on the measurements of high energy muons ($p_T > 1$ TeV) in the $Z' \to \mu^+\mu^-$ decay channel.

The muon system has three purposes: muon identification, muon trigger and muon momentum measurement. The CMS muon system is designed to have the capability of reconstructing the momentum and charge of muons over the the entire kinematic range of the LHC (Chatrchyan, 2008). The muon system is driven to have a cylindrical shape due to the shape of the solenoid magnet and consists of a barrel section and two endcap regions. In the barrel region, the muon rate is low and the 4-T magnetic field is uniform. The barrel drift tube (DT) chambers cover the pseudorapidity region $|\eta| < 1.2$ and are organized into 4 stations. The first 3 stations measure the muon coordinate in the $r-\phi$ bending plane and z direction, along the beam line. The fourth station is used to achieve the best angular resolution. In the 2 endcap regions, the muon rate is high and the magnetic field is large and non-uniform. The muon system in the endcap regions uses cathode strip chambers (CSC) and cover the pseudorapidity region $0.9 < |\eta| < 2.4$. Each endcap has 4 stations of CSCs.

The muon identification is provided over the range corresponding to $10^o < \theta < 170^o$ since the muon detectors cover the full pseudorapidity interval $|\eta| < 2.4$ without acceptance gaps. The offline reconstruction efficiency of single-muon varies between 95% and 99%. The offline muon momentum resolution of the standalone muon is about 9% for small values of $|\eta|$ and for transverse momenta up to 200 GeV. The standalone momentum resolution at 1 TeV varies between 15% and 40%, depending on $|\eta|$. A global muon momentum using also the inner tracker improves the momentum resolution at low momenta. At 1 TeV, the momentum resolution of a global muon is about 5% (Chatrchyan, 2008).

3.2.5 The DAQ and Trigger

The Trigger and Data Acquisition (DAQ) system of a hadron collider experiment is necessary because the collision data rate is much higher than the rate of writing data to mass storage. At the LHC, the proton beams will cross each other at a frequency of 40 MHz and the CMS Trigger and DAQ system is designed to collect and analyze the events from the detector information at that frequency. At the design luminosity of the LHC

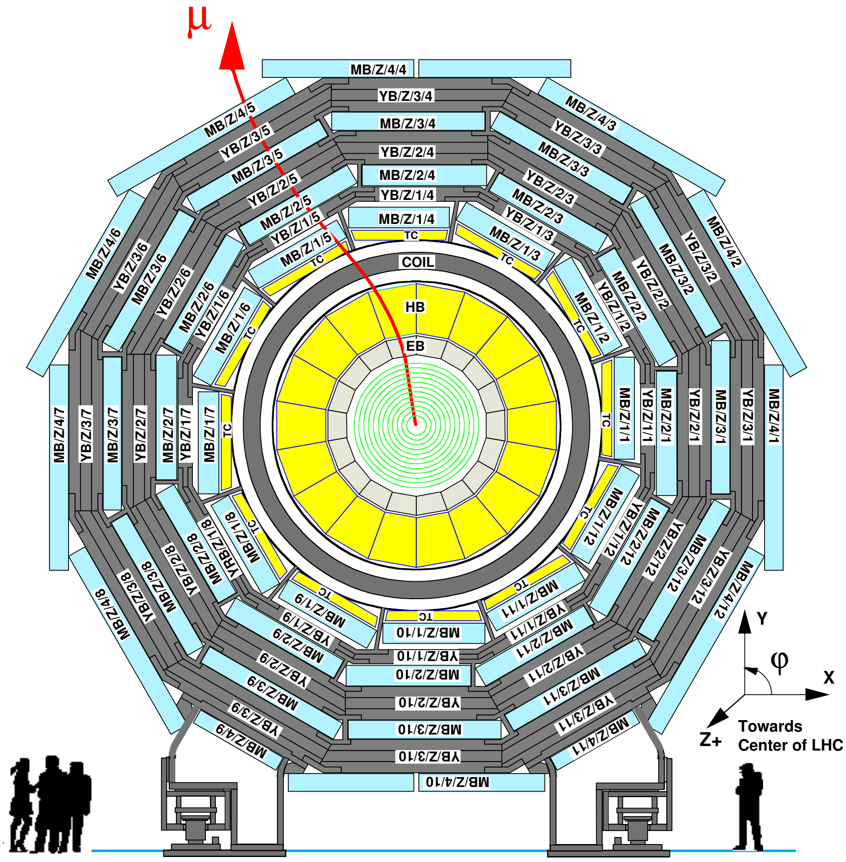

Figure 3.14. A transverse view of the CMS barrel muon DT chambers in one of the 5 wheels.

(10^{34} cm^{-2}s^{-1}) leads an average of about 20 inelastic *pp* event producing approximately 1 MB of zero-suppressed data (Bayatian, 2000a). The rate of events to be recorded for offline processing and analysis is on the order of a few 10^2 kHz. The full selection task is split into two steps. The first level trigger is designed to reduce the incoming average data rate to a maximum of 100 kHz, by information coming from the calorimeter and the muon chambers. The second step, High Level Trigger (HLT), reduces the rate of stored events by a factor of 1000. The architecture of the DAQ system is shown schematically in Fig.3.15.

The Level-1 Trigger has to process information from the CMS detector at the full beam crossing rate of 40 MHz. The time between two beam crossings (25 ns) makes impossible using fully programmable processing elements. The time available for processing in the Level-1 Trigger system is limited by front-end electronics availability and the maximum time interval for a Level-1 decision to be received by the front-end elec-

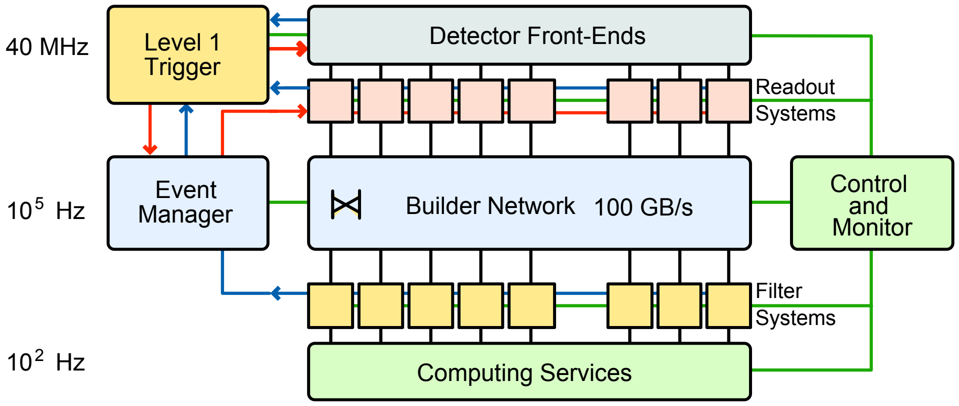

Figure 3.15. Architecture of the CMS DAQ system.

tronics is 3 μs. Therefore the Level-1 Trigger can only process data from a subset of CMS subdetectors, the calorimeters and muon chambers. The Level-1 Trigger system achieves a crossing reduction factor of 400, for a maximum mean event rate of 100 kHz.

The next selection step, the High-Level Trigger will receive, on average, one event every 10 μs. This time is sufficiently long, therefore the algorithms can be used in the offline reconstruction of the events. The average processing time is roughly 40 ms, with some events requiring up to 1 second.

3.2.6 The Computing

The CMS offline computing system has to support the storage, transfer and manipulation of the recorded collision data. The system also must access to conditions and calibration information and other non-event data. The CMS application software performs a variety of event processing, selection and analysis tasks. The main concept of the CMS data model is the Event. The Event provides access to the recorded data. The Events are physically stored as ROOT files.

The Event is used by a variety of physics modules which performs a well-defined function of reconstruction or analysis of the Event. The modules execute independently from one another. The CMS Application Framework is illustrated in Fig.3.16.

The CMS computing system has several event formats with differing levels of detail and precision in order to achieve the required level of data reduction.

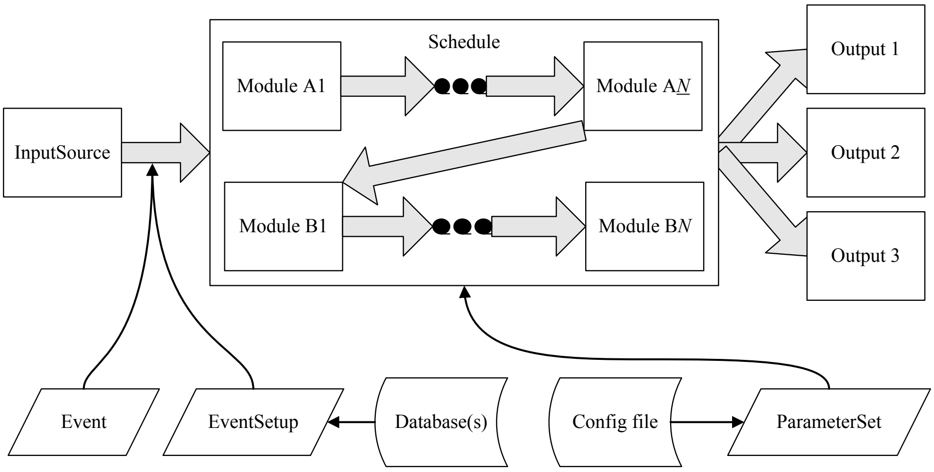

Figure 3.16. The CMS Application Framework with modules.

The RAW format contains the full recorded information from the detector and also a record of the trigger decision. The RAW data is permanently archived in safe storage with size of 1.5 MB/event. For simulated data, the size RAW format is about 2 $MB/event$ due to additional Monte Carlo truth information. The largest contribution is expected from the silicon strip detector.

Reconstructed (RECO) data is derived from RAW data and should provide access to reconstructed physics objects for physics analysis in a convenient format. Event reconstruction is structured in several algorithms which include detector-specific filtering and correction of the the digitized data; cluster- and track-finding; primary and secondary vertex reconstruction; and particle ID (Chatrchyan, 2008). The resulting RECO events contain high-level physics objects such as jets, muons, electrons, b-jets, etc. The RECO format is about 250 kB/event.

The Analysis Object Data (AOD) is the compact analysis format and is produced by filtering of RECO data. The AOD data format is about 50 kB/event.

The computing system with such a scale could not be hosted entirely at one site. Thus, the CMS offline computing system is arranged in four tiers. A single Tier-0 centre at CERN accepts data from the CMS Online DAQ System and performs prompt first pass reconstruction. The Tier-0 distributes raw and processed data to a set of large Tier-1 centers in CMS collaborating countries. These centers provide services for data archiving, reconstruction, calibration, skimming and other data-intensive analysis tasks. A more numerous set of Tier-2 centers provide capacity for analysis, calibration activities and Monte Carlo simulation. Tier-3 centers provide interactive resources for local groups and additional best effort computing capacity for the collaboration. The majority of CMS users rely upon Tier-2 or Tier-3 resources as their base for analysis (Bayatian, 2005). The data flow between CMS Computing Centers is illustrated in Fig.3.17.

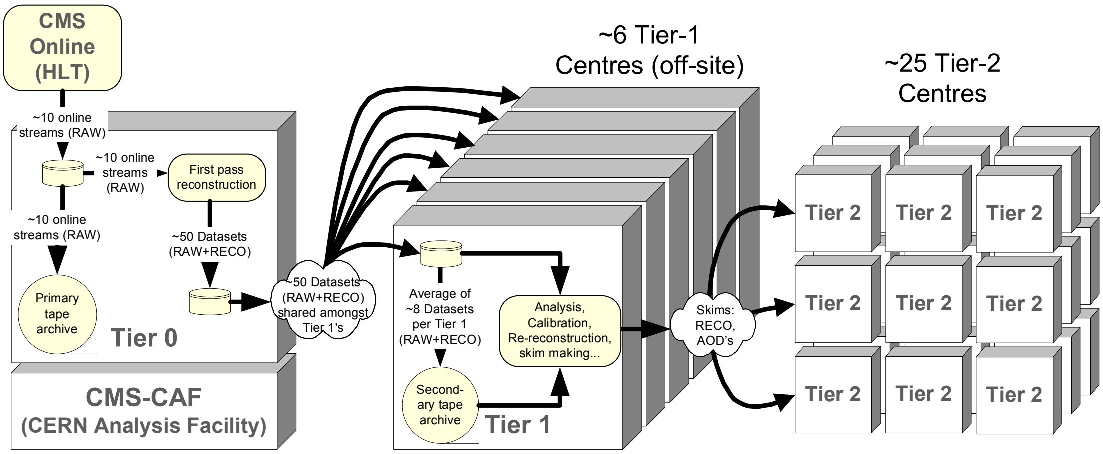

Figure 3.17. The data flow between CMS Computing Centers.

4. JET RECONSTRUCTION AT CMS

In this chapter, properties of jets and jet reconstruction methods at CMS detector will be discussed.

4.1 Kinematics and Definition of Jets

Quarks and gluons cannot be in free form because of their color charge, therefore they hadronize. A jet is the experimental signature of a parton, materialized as a spray of energetic hadrons. Fig.4.1 shows the evolution of a jet.

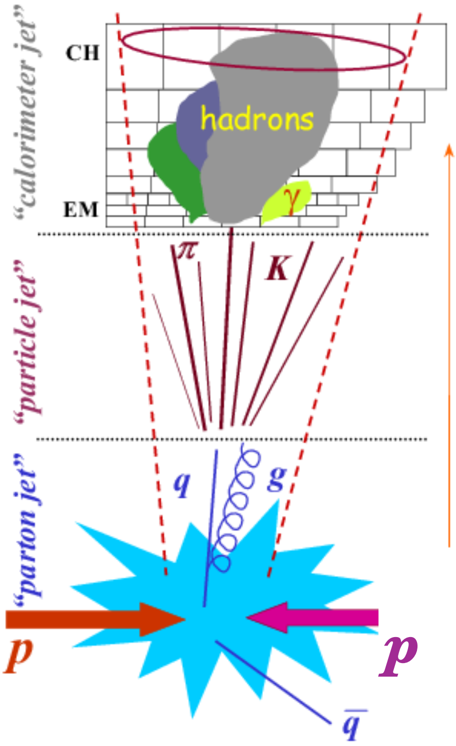

Figure 4.1. Evolution of a Jet.

Events in which jets are created are used to understand the strong interaction (QCD) and also to search for new physics strongly interacting. A jet can be described using the variables p_T (transverse momentum), ϕ (azimuth angle), y (rapidity) and m (mass). The four components of momenta can be written as (Ellis, 1996)

$$p^{\mu} = (\sqrt{p_t^2 + m^2}\cosh(y), p_t \sin\phi, p_t \cos\phi, \sqrt{p_t^2 + m^2}\sinh(y)). \tag{4.1}$$

The rapidty is given by

$$y = \frac{1}{2}\ln(\frac{E + p_z}{E - p_z}) \tag{4.2}$$

where z is the beam direction. For $m \rightarrow 0$, rapidity is replaced by the pseudorapidity, η.

$$\eta = -\ln\tan(\frac{\theta}{2}) \tag{4.3}$$

It is a more useful variable experimentally, because the angle θ from the beam direction is measured directly in the detector. A jet is defined as a cluster of transverse energy E_T in a cone size ΔR which is given by

$$\Delta R = \sqrt{(\Delta\eta)^2 + (\Delta\phi)^2} \tag{4.4}$$

The transverse energy, E_T, pseudorapidity, η, and azimuth, ϕ, of a jet are defined below (Ellis, 2007).

$$E_{T_{jet}} = \sum_{i \in jet} E_{T_i} \tag{4.5}$$

$$\eta_{jet} = \frac{1}{E_{T_{jet}}} \sum_{i \in jet} E_{T_i}\eta_i \tag{4.6}$$

$$\phi_{jet} = \frac{1}{E_{T_{jet}}} \sum_{i \in jet} E_{T_i}\phi_i \tag{4.7}$$

4.2 Jet Types at CMS

There are four types of reconstructed jets at CMS, which differently combine individual contributions from sub-detectors to form the inputs to the jet clustering algorithm. These jet types are:

Calorimeter Jets: Energy deposition in the calorimeters cells (HCAL and ECAL) which is combined into calorimeter towers are used for reconstruction. The calorimeter towers are the input into jet reconstruction algorithms. A calorimeter tower consists of HCAL cells and the geometrically corresponding ECAL crystals. The thresholds are applied on energies of the individual cells to suppress the contribution from calorimeter readout electronics noise when building calorimeter towers. These threshold values can be seen in Table 4.1 (Zielinski, 2010). In addition, to suppress contribution from event pile-up, calorimeter towers with transverse energy of $E_T^{towers} < 0.3$ GeV are not used in jet reconstruction. Fig.4.2 shows an event display of a dijet event. The calorimeter segmentation in η and ϕ is shown with energy deposition in calorimeter towers. The blue part shows energy deposition in HCAL and red part shows energy deposition in ECAL.

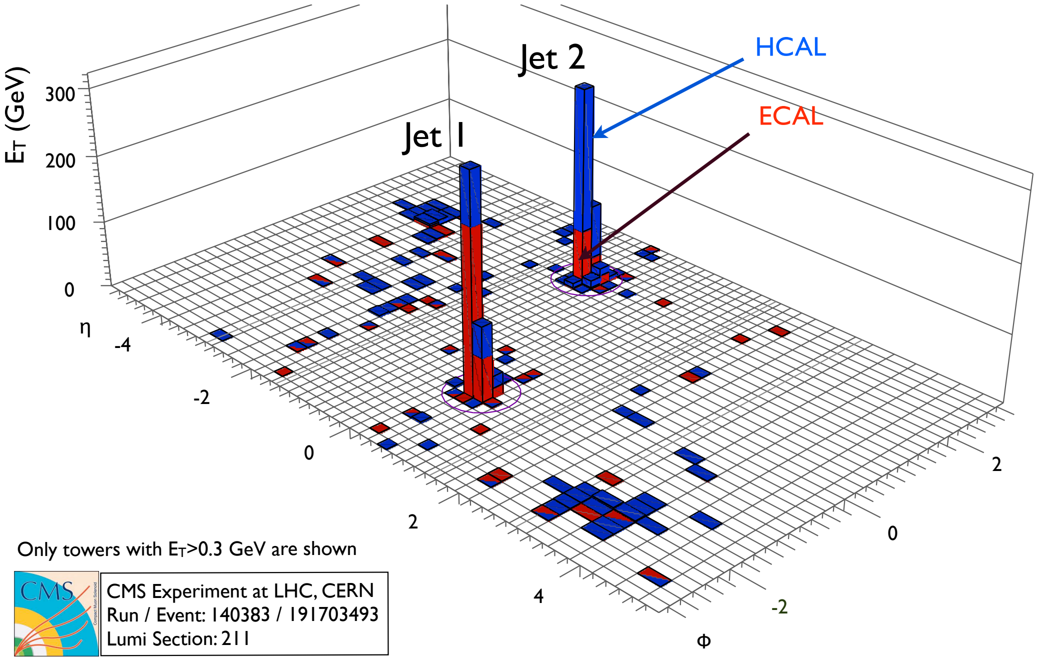

Figure 4.2. An observed dijet event in the CMS calorimeters. Energy deposition in HCAL is shown by blue and energy deposition in ECAL is shown by red.

Jet-Plus-Tracks: In addition to calorimeter towers, charged particle tracks associated with jets are used for reconstruction. The associated tracks are projected onto the surface of the calorimeter. The Jet Plus Tracks algorithm (JPT) corrects the energy of a jet reconstructed from calorimetric energy depositions, using the momentum of charged particles measured in the tracker (Nikitenko, 2009).

Section	Threshold (GeV)
HB	0.7
HE	0.8
HO	1.1 / 3.5 (Ring 0 / Ring 1,2)
HF (Long)	0.5
HF (Short)	0.85
EB	0.07 (per crystal, double sided)
EE	0.3 (per crystal, double sided)
EB Sum	0.2
EE Sum	0.45

Table 4.1. Threshold of Calorimeter cell used in calorimeter and JPT jet reconstruction (Zielinski, 2010).

Particle Flow (PF) Jets: PF jets are reconstructed by all CMS sub-detectors to identify all stable particles in the events, such as muons, electrons, photons, charged hadrons and neutral hadrons (Bernet, 2009). Photons are reconstructed from energy clusters in ECAL. Electrons are reconstructed by a combination of a track and energy deposition in the ECAL. Muons are reconstructed from a combination of the tracker and muon chamber. Charged and neutral hadrons deposit their energy in HCAL. Charged hadrons are reconstructed with tracker in addition to HCAL. These elements are then linked topologically into blocks and PF jets are reconstructed from resulting of these blocks. The jet energy measurement and resolution are improved with respect to the calorimeter jets due to the using of tracker and ECAL which allows to measure charged particles and photons inside jets precisely.

Track Jets: Track Jets are reconstructed only from track of charged particles measured in the CMS central trackers and completely independent from the calorimetric jet measurement (Azzurri, 2010). Track jets are extremely efficient to find jets of any energy, down to very low p_T.

4.3 Jet Reconstruction Algorithms at CMS

A jet is reconstructed from energy deposition in calorimeter towers and from track momentum of charged particles. Jet reconstruction algoritms which provide a set of rules for clustering particles or calorimeter towers based on proximity into jets are used for jet reconstruction. Basically, a good jet reconstruction algorithm should satisfy some issues as listed below (Salam, 2009).

- It should be fully specified, including defining in detail any pre-clustering, merging and splitting,
- It should be simple to implement in an experimental analysis and should be independent of detector structure,
- It should be simple to implement in a theoretical calculation,
- It should yield a finite cross section at any order in perturbation theory,
- It should yield a cross section that is relatively insensitive to hadronization effects,
- It should be Infrared and collinear (IRC) safe.

Infrared and collinear (IRC) safety is a fundamental requirement for jet algorithms. Infrared safety is that adding a soft gluon should not change the results of the jet clustering. Collinear safety is that splitting one parton into two partons should not change the results of the jet clustering (Salam, 2009). The configurations of infrared and collinear safety are shown separately in Fig.4.3.

Mainly, there are three types of jet reconstruction algorithm which are used by the CMS experiment. These jet reconstruction algorithms are discussed below.

4.3.1 Iterative Cone Algorithm

Iterative cone is a simple cone-based algorithm. Since it has short execution time, it is used by CMS in the High Level Trigger (HLT) (Schieferdecker, 2007). In this algorithm, a seed particle (or calorimeter tower) with energy greater than 1 GeV labeled with

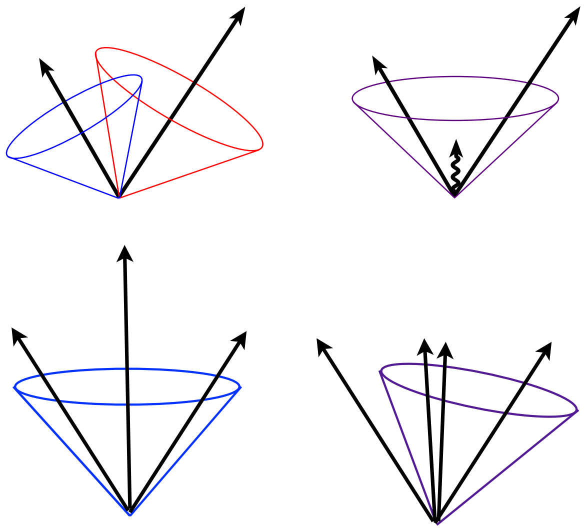

Figure 4.3. Infrared safety (top): adding a soft gluon should not change the jet clustering results. Collinear safety (bottom): splitting one parton into two collinear partons should not change the jet clustering results.

p_T ordered, i sets some initial direction and one sums the momentum of all particles j within a cone of radius R around i in azimuthal angle ϕ and rapidity y taking all j as

$$\Delta R_{ij} = \sqrt{(y_i - y_j)^2 + (\phi_i - \phi_j)^2} < R \tag{4.8}$$

where y_i and ϕ_i are respectively the rapidity and azimuth of particle i (Salam, 2010). This calculation is iterated until a stable cone is found. The dimensionless parameter R is the radius of jet. Once a stable cone is found, it is declared a jet and its constituents are removed from the remaining inputs. The algorithm is neither collinear- nor infrared-safe (Schieferdecker, 2007). CMS supports iterative cone algorithm with cone $R = 0.5$.

4.3.2 Seedless Infrared Stable Cone (SISCone) Algorithm

Current cone jet algorithms, such as iterative cone algorithm, take all particles in the event as a seed and search for stable cones. A soft particle is added between the two hard particles, it behaves as a seed and then a third stable cone may be found. This problem is know as infrared unsafety as discussed before.

In order to solve this problem in the cone algorithms, a seedless search for all

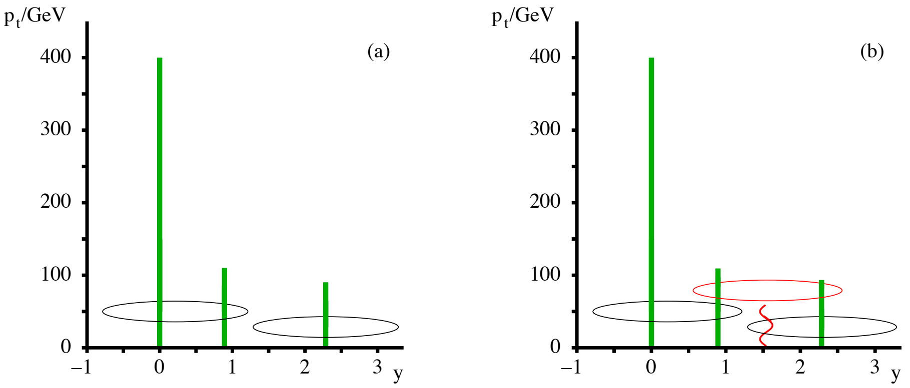

Figure 4.4. A configuration (left) gives different jets adding a soft particle with 1 GeV of p_T (right) (Salam, 2007).

stable cones was proposed and was named as Midpoint Cone Algorithm (Blazey, 2000). According to this proposal, after finding stable cones with true seed particles, counterfeit midpoint seeds are added between pairs of stable cones and search for new stable cones. But it took time $\sim N\times 2^N$ to find jets among N particles (10^{17} years for 100 particles), it was useless and unthinkable (Salam, 2007). This problem is solved by generalization of the above procedure into 2-dimensions. In one dimension example, there was a single degree of freedom (y or η) to determine the position of the segment. In 2-dimensions, there are two degrees of freedom (y,ϕ) to determine the position of a circle which has a pair of particles in its circumference (Salam, 2007). This approach is illustrated in Fig.4.5.

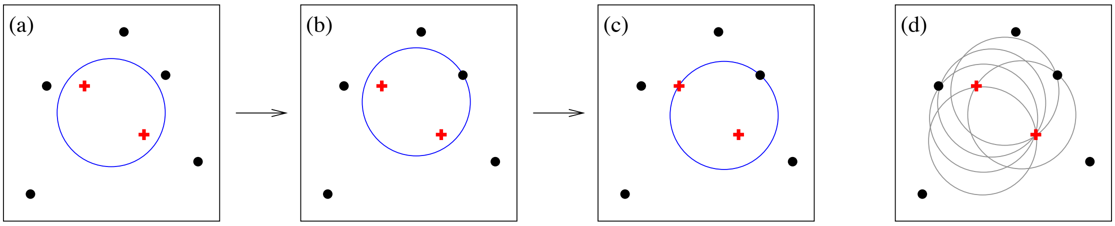

Figure 4.5. Some initial circular enclosure (a); moving the circle in a random direction until some enclosed or external point touches the edge of the circle (b); pivoting the circle around the edge point until a second point touches the edge (c); all circles defined by pairs of edge points leading to the same circular enclosure (d) (Salam, 2007).

It takes $\sim N^2 \cdot \ln(N)$ time and provides an acceptable IR safe cone algorithm. The final version of the seedless algorithm is named as SISCone and practical at parton, hadron and detector levels. However SISCone is not recommended as default jet finding algorithm in CMS experiment since it doesn't work for the events with high pile-up activity and it is not CPU efficient. CMS supports SisCone algorithm with cone sizes $R = 0.5$ and $R = 0.7$.

4.3.3 Anti-k_T Algorithm

The anti-k_T algorithm is an infrared and collinear safe algorithm and it is used by CMS as default jet reconstruction algorithm. The anti-k_T is a special form of k_T algorithm. The k_T algorithm is based on a pair-wise recombination and combines two particles (or calorimeter towers) if their relative transverse momentum is less than a given measure. The distance d_{ij} between particle (or calorimeter tower) i and j and d_{iB} between i and beam (B) are defined as

$$d_{ij} = min(p_{Ti}^2, p_{Tj}^2)\frac{\Delta R_{ij}^2}{R^2} \tag{4.9}$$

$$d_{iB} = p_{Ti}^2 \tag{4.10}$$

$$\Delta R_{ij}^2 = (y_i - y_j)^2 + (\phi_i - \phi_j)^2 \tag{4.11}$$

where R has a similar role as in the cone algorithm (Salam, 2010). The k_T works in following steps:

1. Make list of particles.
2. Calculate d_{ij} and d_{iB}.
3. If d_{ij} is smallest, combine i and j into a single new particle and return to step 1.
4. Otherwise, it d_{iB} is smallest, remove i from the list and return to step 1.
5. Repeat until no particles left.

The distance measurement can be generalized as

$$d_{ij} = min(p_{Ti}^{2p}, p_{Tj}^{2p})\frac{\Delta R_{ij}^2}{R^2} \tag{4.12}$$

$$d_{iB} = p_{Ti}^{2p} \tag{4.13}$$

where p is a parameter that is 1 for k_T algorithm. It means that soft particles are clustered firstly. If $p = -1$, anti-k_T algorithm is obtained and hard particles are clustered firstly rather than soft particles (Salam, 2010). If $p = 0$, an energy dependent clustering algorithm which is called as Cambridge/Aachen (CA) algorithm is obtained. The behaviors of different jet algorithms are illustrated in Fig.4.6. The anti-k_T jet algorithm gives the best shape of jets. CMS supports k_T algorithm with cone sizes $R = 0.4$ and $R = 0.6$ and supports anti-k_T algorithm with cone sizes $R = 0.5$ and $R = 0.7$.

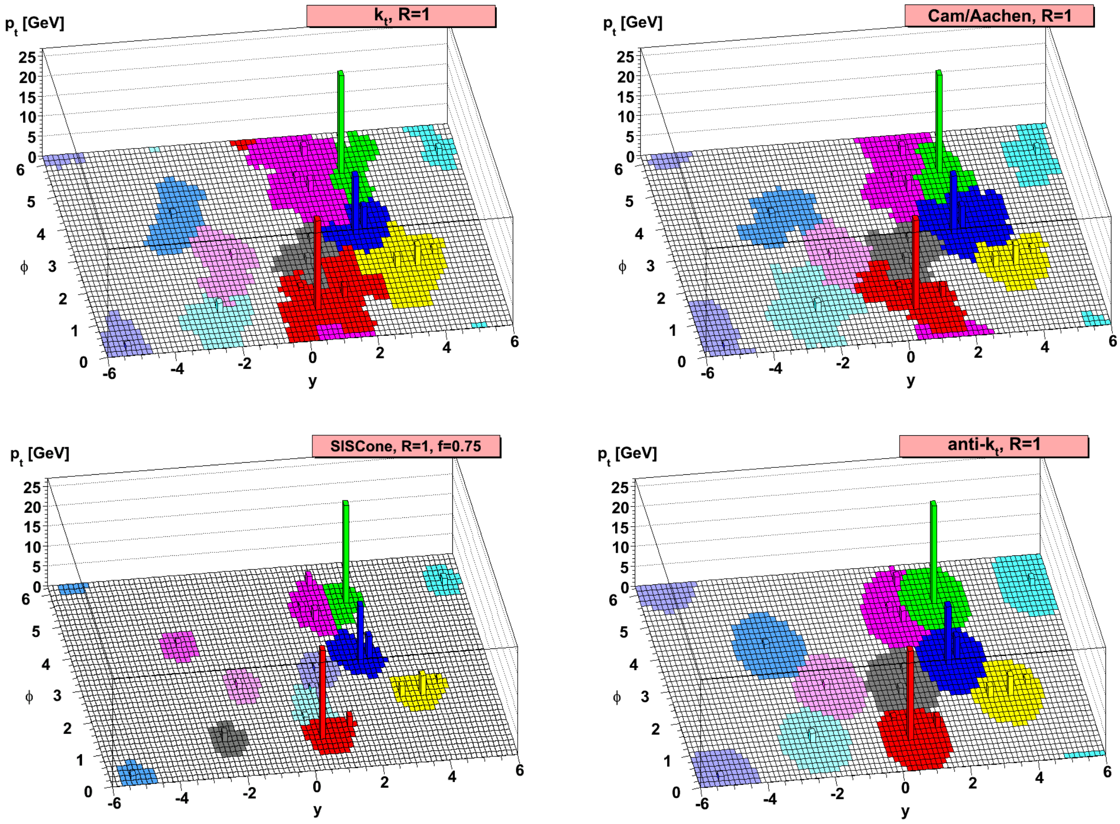

Figure 4.6. The behaviors of different jet algorithms in parton level (Salam, 2010).

4.4 Jet Energy Calibration

Jet energy measurement is typically different from the corresponding particle jet energy. The main reason for this energy inconsistency is the non-uniform and non-linear response of the CMS calorimeters. In addition, electronic noise and event pile-up can cause extra unwanted energy. The aim of jet energy correction is to relate, on average, the jet energy measurement in the detector to the energy of corresponding particle jet. CMS has a factorized multi-level jet energy calibration, in which the correction must be applied in the following fixed sequence (Harris, 2007):

1. **Offset:** Required correction for pile-up and electronic noise.
2. **Relative (η):** Required correction for jet response versus pseudorapidity relative to a control region.
3. **Absolute (p_T):** Required correction for jet response versus p_T in the control region.
4. **EMF:** Optional correction for jet response with electromagnetic energy fraction.
5. **Flavor:** Optional correction to particle level for different types of jets (light quarks, c, b, gluon).
6. **Underlying Event (UE):** Optional correction for underlying event energy.
7. **Parton:** Optional correction for parton level.

The equation relating the corrected CaloJet energy to uncorrected CaloJet energy is given by

$$E_{Corrected} = (E_{Uncorrected} - E_{Offset}) \times C(rel:\eta) \times C(abs:p_T) \tag{4.14}$$

which includes the offset, relative and absolute corrections. These first three steps are the required corrections. It can be extended further by multiplying the right hand side with optional correction factors.

Figure 4.7. Schematic picture of a factorized multi-level jet correction. Solid boxes show required correction levels and dashed boxes show optional correction levels (Harris, 2007).

Offset Correction

Pile-up of multiple interactions within the same bunch crossing and electronic noise in the detector produce an energy offset. For the data taking period of March-July, the average number of pile-up ranges from $< N_{PU} >\simeq 0.001$ for early runs up to $< N_{PU} >\simeq 0.5$ (Zielinski, 2010).The electronic noise contribution is estimated from Zero Bias trigger with Minimum Bias trigger veto. It gives a pure noise sample. Fig.4.8 shows $E_{Offset}(\eta)$ and $P_{T_{Offset}}(\eta)$ for noise and noise+one pile-up. Noise contribution is less than 250 MeV and noise+one pile-up contribution is less than 400 GeV in p_T. The offset contribution increases up to 7 GeV in energy in the forward region.

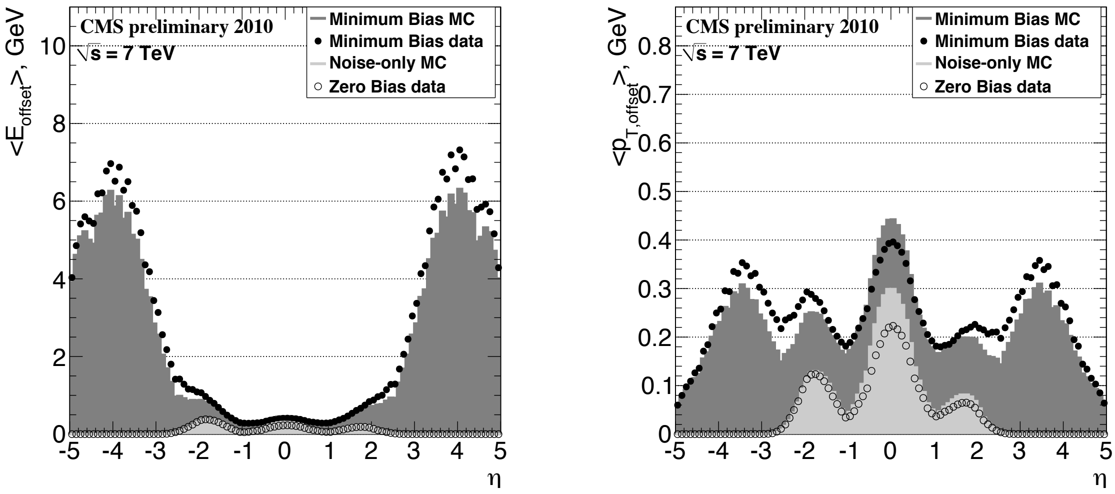

Figure 4.8. Offset contribution from noise only and from noise+one pile-up as function of η in energy (left) and transverse momentum (right) (Zielinski, 2010).

Relative Correction: η Dependence

The jet response of CMS varies as a function of jet η for a fixed jet p_T. The goal of the relative correction is to remove these variations and obtain a flat response as a function of η. This correction should be done after the offset correction. The dijet balance method is used to derive relative jet energy correction (Harris, 2008). In the dijet balance method, p_T balances in back-to-back dijet events with one jet (barrel jet) in the central control region of the calorimeter ($|\eta| < 1.3$) and the other jet (probe jet) with arbitrary η. The two leading jets must be separated by $\Delta\phi > 2.7$ and no additional third jet in the event is allowed with $p_T^{3^{rd}Jet}/p_T^{dijet}$ to enrich the sample in $2 \to 2$ process, where $p_T^{dijet} = (p_T^{probe} + p_T^{barrel})/2$ is an average uncorrected p_T of two leading jets. The balance quality is given by

$$B = \frac{p_T^{probe} - p_T^{barrel}}{p_T^{dijet}} \tag{4.15}$$

in the bins of η^{probe} and p_T^{dijet}. The relative response from the average value of B distribution, $< B >$, in a given η^{probe} and p_T^{dijet} bin is defined as below (Harris, 2008).

$$R(\eta^{probe}, p_T^{dijet}) = \frac{2+ < B >}{2- < B >} \tag{4.16}$$

The relative jet response as a function of η obtained from data and MC prediction are shown in Fig.4.9 for different p_T^{dijet} ranges.

Absolute Correction: p_T Dependence

CMS calorimeter energy response varies as a function of jet p_T. The goal of the absolute jet energy correction is to make the response equal to unity at all p_T for the control region $|\eta| < 1.3$. Absolute jet energy correction from collider data is determined using $\gamma + jet$ events with applying two different procedures which are called p_T balancing method and MPF (missing E_T projection fraction) method (Zielinski, 2010). In p_T balancing method, the balance in the transverse plane between the photon and the recoiling

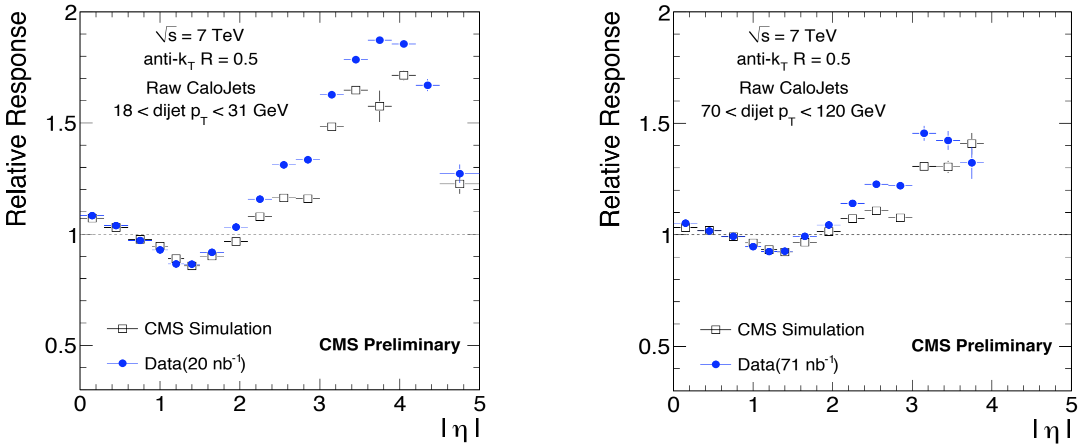

Figure 4.9. Relative jet response for calorimeter jets as a function of η for various p_T^{dijet} bins. (Zielinski, 2010).

jet is considered and photon p_T which is accurately measured in the ECAL calorimeter is used as a reference object. MPF method is the main method for absolute jet energy correction of CMS. In MPF method, it is assumed that $\gamma + jet$ events have no real missing E_T and there is a perfect balance between photon and hadronic recoil in the transverse plane.

$$\overrightarrow{p}_T^{\gamma} + \overrightarrow{p}_T^{recoil} = 0 \tag{4.17}$$

This equation can be rewritten for the reconstructed event as

$$R_\gamma \overrightarrow{p}_T^{\gamma} + R_{recoil}\, \overrightarrow{p}_T^{recoil} = -\overrightarrow{E}_T^{miss} \tag{4.18}$$

where R_γ and R_{recoil} are response of detector to the photon and the hadronic recoil. Since photons are well calibrated, $R_\gamma = 1$, R_{recoil} after solving the two equation is given

$$R_{MPF} \equiv \frac{R_{recoil}}{R_\gamma} = 1 + \frac{\overrightarrow{E}_T^{miss} \cdot \overrightarrow{p}_T^{\gamma}}{(p_T^{\gamma})^2} = R_{recoil} \tag{4.19}$$

Fig.4.10 shows response of $< p_T/p_\gamma >$ and MPF response as a function of photon p_T.

True response is the mean value of the p_T ratio of reconstructed jet and particle level jet after matching, $< p_T^{CaloJet}/p_T^{GenJet} >$.

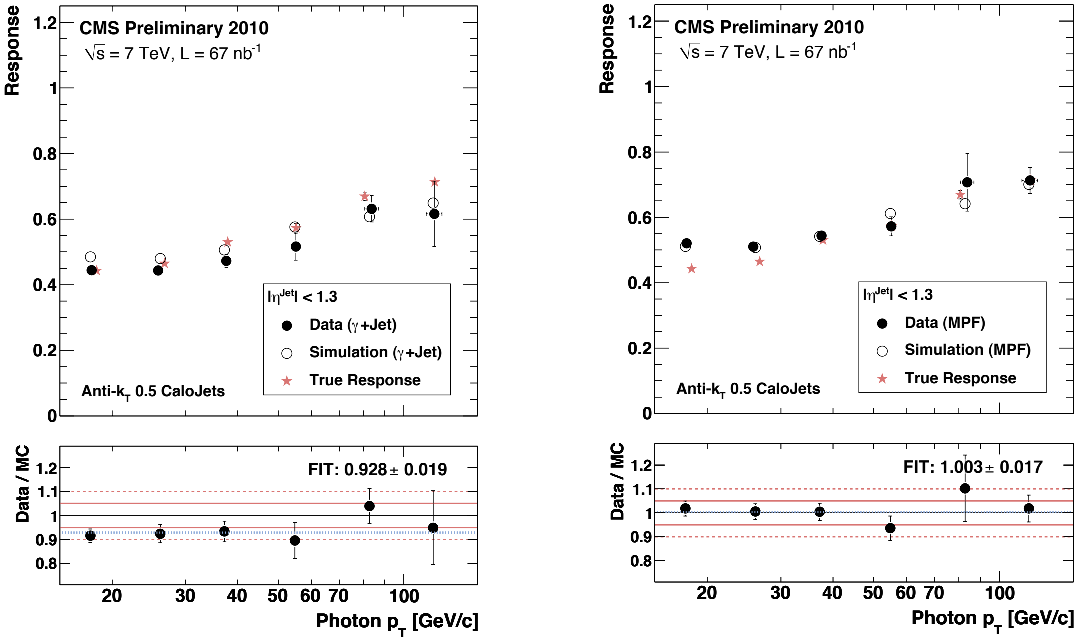

Figure 4.10. Response of $< p_T/p_\gamma >$ (left) and MPF response (right) as a function of photon p_T from data and simulation (Zielinski, 2010).

4.5 Jet Quality Criteria

Unphysical energy deposition in the calorimeter originating from,e.g. calorimeter noise, beam halo, cosmic background might lead to fake jets in the data. Some jet quality criteria are derived to reject the unphysical fake jets, called as ”Jet Identification” or ”Jet ID” criteria. A set of variables are considered which give idea about a jet originating from a *pp* collision. These variables are listed below (Harel, 2009).

1. **fHPD**: fraction of the jet’s energy measured by the most energetic HPD.
2. **fRBX**: fraction of the jet’s energy measured by the most energetic RBX.
3. σ_η: the RMS of the E_T-weighted η distribution of the calorimeter towers clustered into a jet.

$$\sigma_\eta = \sqrt{\left[\sum_{\text{tow}} \frac{E_T^{\text{tow}}}{E_T} \eta_{\text{tow}}^2\right] - \left[\sum_{\text{tow}} \frac{E_T^{\text{tow}}}{E_T} \eta_{\text{tow}}\right]^2}, \tag{4.20}$$

where E_T is the transverse energy of the jet, while E_T^{tow} and η_{tow} denote respectively the transverse energy deposited in the calorimeter towers belonging to the jet and the pseudorapidity of those calorimeter towers.

4. σ_ϕ: the RMS of the E_T-weighted ϕ distribution of the calorimeter towers clustered into a jet.

$$\sigma_\phi = \sqrt{\left[\sum_{\text{tow}} \frac{E_T^{\text{tow}}}{E_T} \phi_{\text{tow}}^2\right] - \left[\sum_{\text{tow}} \frac{E_T^{\text{tow}}}{E_T} \phi_{\text{tow}}\right]^2}, \tag{4.21}$$

where ϕ_{tow} denotes the azimuthal angle of calorimeter towers belonging to the jet.

5. **n90**: minimum number of energy ordered calorimeter towers carrying 90% of the jet energy.
6. **n90hits**: minimum number of energy ordered calorimeter rechits carrying 90% of the jet energy.
7. **EMF**: electromagnetic energy fraction of the jet.
8. **nTrkCalo**: number of tracks associated to a jet at the calorimeter face.

Most of the quantities are based on the jet energy as measured in the calorimeters. If a jet is originated from HPD or RBX noise, fHPD or fRBX should be close to 1, respectively. In case a jet is generated by HCAL noise, the all jet energy deposits in HCAL and EMF of the jet is close to 0. If a jet is originated from the noise in a single cell like an ECAL spike, all jet energy deposition might come from one channel and n90hits is close to 1. Fig.4.11 shows an event display of HPD noise which leads to three reconstructed jets in CMS.

Two sets of standard jet quality selection criteria have been defined, loose and tight, which remove fake jets efficiently. The loose and tight JetID criteria for calorimeter jets are summarized in Table 4.2.

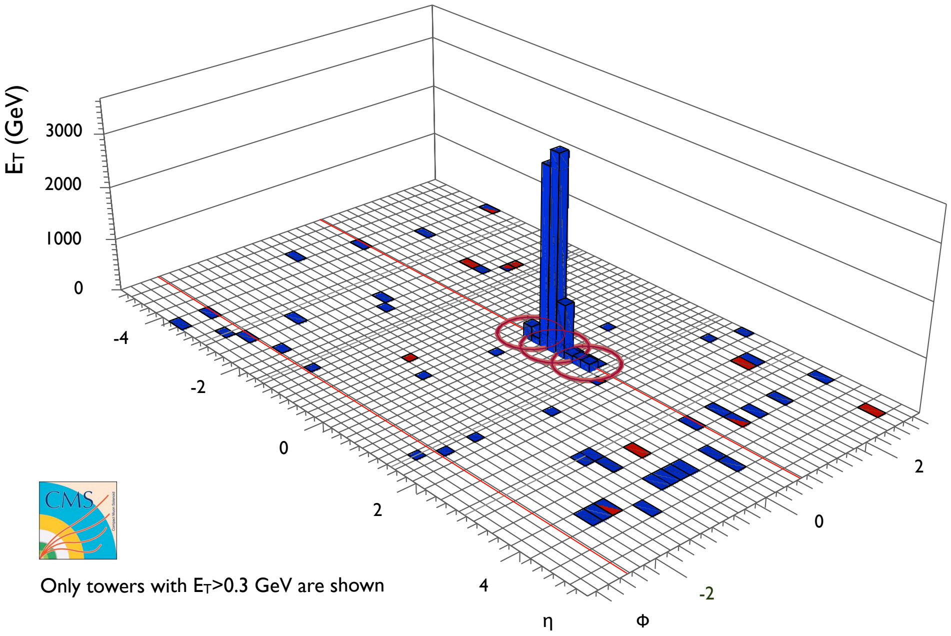

Figure 4.11. An example event display of HPD noise in CMS.

Variable	$\|\eta\|$	loose	tight
EMF	< 2.6	> 0.01	> 0.01
$n90hits$	-	> 1	> 4
$fHPD$	-	< 0.98	< 0.98
$fRBX$	-	-	< 0.98
σ_η	-	-	> 0.01
σ_ϕ	-	-	> 0.01

Table 4.2. Loose and tight calorimeter jet quality criteria.

4.6 Jet Trigger

The jet trigger uses the transverse energy sums of HCAL and ECAL in 4×4 trigger towers for the $|\eta| < 3$ region. In the forward hadron calorimeter the region is the trigger tower itself. The jet candidates are characterized by transverse energy in 3×3 calorimeter region (corresponding to 12×12 trigger towers) which is illustrated in Fig.4.12. This square region nearly surrenders a jet cone radius of 0.7. This global jet finding is performed using iterative cone algorithm with cone size of 0.5 since it has significantly better resolution at low E_T. The HLT trigger paths with seed threshold for low E_T are listed in Table 4.3.

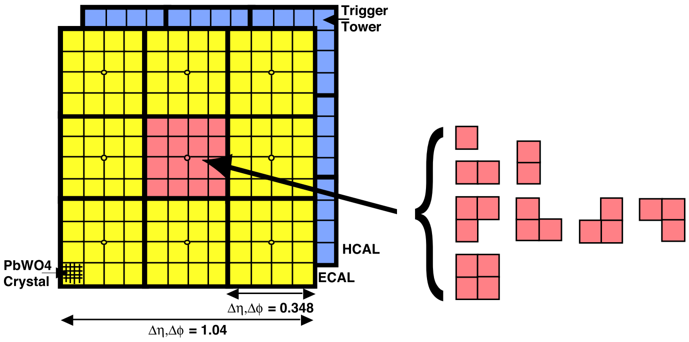

Figure 4.12. Jet trigger algorithm (Dasu, 2002).

Trigger Path	L1 seeds	Description
L1_SingleJet6U	none	1 Jet with $E_T > 6$ GeV
HLT_L1Jet6U	L1_SingleJet6U	No selections beyond L1
HLT_Jet15U	L1_SingleJet6U	A single jet trigger, requiring $\geq$ 1 jet at HLT with $E_T > 15$ GeV. The jet energy threshold is chosen based on uncorrected jets.
HLT_Jet30U	L1_SingleJet15U	A single jet trigger, requiring $\geq$ 1 jet at HLT with $E_T > 30$ GeV. The jet energy threshold is chosen based on uncorrected jets.
HLT_Jet50U	L1_SingleJet30U	A single jet trigger, requiring $\geq$ 1 jet at HLT with $E_T > 50$ GeV. The jet energy threshold is chosen based on uncorrected jets.

Table 4.3. L1 and High Level Trigger jet descriptions.

5. MEASUREMENT OF DIJET MASS SPECTRUM

In this chapter, measurement of dijet mass spectrum will be discussed. Then, the observed dijet mass spectrum will be compared with the Monte Carlo prediction for QCD and with a smooth fit to test the smoothness of the data.

5.1 Data Sample and Event Selection

This analysis is based on data collected during April-August, 2010. The dataset were;

```
(135059-135735) /MinimumBias/Commissioning10-SD_JetMETTau-Jun14thSkim_v1/RECO
(136066-137028) /JetMETTau/Run2010A-Jun14thReReco_v2/RECO
(137437-139558) /JetMETTau/Run2010A-PromptReco-v4/RECO
(139779-140159) /JetMETTau/Run2010A-Jul16thReReco-v1/RECO
(140160-141899) /JetMETTau/Run2010A-PromptReco-v4/RECO
(141900-142664) /JetMET/Run2010A-PromptReco-v4/RECO
```

The data was reconstructed using $CMSSW\_3\_6\_1\_patch4$. The good runs and luminosity sections were selected based on official CMS JSON files. The integrated luminosity of the selected data sample is 2.875 ± 0.316 pb^{-1}. The integrated luminosity is measured using signals from HF calorimeters. The uncertainty luminosity measurement is about 11%.

The events which have at least two jets were selected. Jets were reconstructed using the anti-kt algorithm with cone size $R = \sqrt{(\Delta\eta)^2 + (\Delta\phi)^2} = 0.7$. The corrections applied for this analysis were the CMS standard relative ($L2$) and absolute ($L3$) corrections for η and p_T variation of the jets using tag ”$Spring10$”. A residual data-driven relative ($L2$) correction was also applied to the data to correct for differences between data and Monte Carlo. The technical trigger bit TT0 selection was made to select events consistent with the LHC bunch crossing. Then, HLT_Jet50U unprescaled trigger selection was required. A dijet mass preselection of corrected $M_{jj} > 100$ GeV was performed because jet energy correction where dijet mass was less than 100 GeV was not reliable. The other event selection criteria are as the following:

Vertex Quality Cuts:

The vertex selection is based on following cuts:

- at least a good primary collision vertex; $nPV \geq 1$,
- primary vertex within 24 cm of center of the detector; $|PVz| < 24$ cm,
- number of degrees of freedom is greater than three; $PVndof > 3$.

The first cut is quite clear, because a vertex is needed to reconstruct jet P_T and η. The second cut makes safe that jets are reasonable near center of the calorimeter so that incidence angles for central and forward calorimeters are absolute. The third cut is to select accurately the reconstructed vertices.

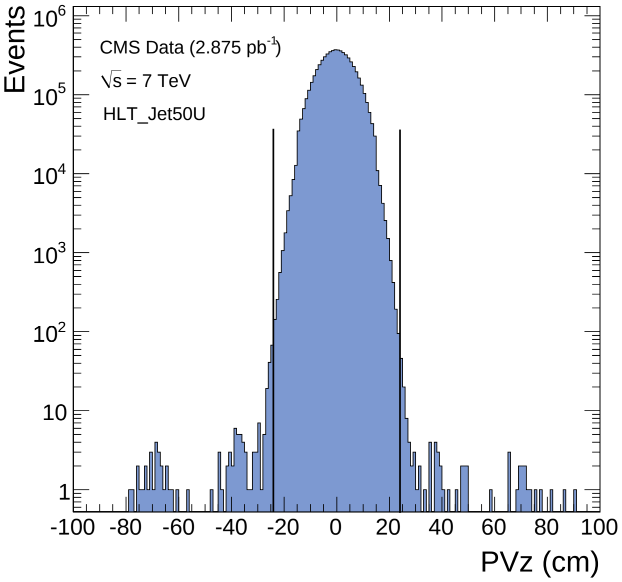

Figure 5.1. Distribution of z values of primary vertices. The events between solid lines were selected.

Jet Identification Cuts:

The jet identification cuts were applied to reject unphysical jets which are caused by mainly HCAL noise or ECAL noise. The cuts also remove the fake jets from cosmic ray background. The loose JetID selection criteria were required for two leading jets which is defined below:

- jet electromagnetic fraction (EMF) > 0.01,
- number of energy ordered rechits carrying 90% of the jet energy (n90hits) > 1,
- fraction of energy contributed by the hottest HPD (fHPD) < 0.98.

The first cut is designed to remove the jets due to noise in the HCAL. The second cut is selected against the jets from the hot cells in ECAL. The third cut rejects the jets generated by HPD noise in HCAL.

Kinematic Cuts:

Both leading jets were required to satisfy the η cuts which are $|\eta_1, \eta_2| < 2.5$ and $|\Delta\eta| < 1.3$. This selection was made because:

- It suppresses QCD processes significantly more than the dijet resonances.
- It defines a fiducial region for our measurement predominantly in the Barrel.
- It provides a faster trigger turn on curve for the jet trigger which uses E_T, allowing us to start the analysis at lower mass.

The eta cut optimization will be discussed in Chapter 6.2.

5.1.1 Trigger Efficiency

The HLT_Jet50U trigger efficiency was measured as a function of dijet mass and corrected transverse momentum of leading jets. In order to measure the efficiency of HTL_Jet50U trigger as a function dijet mass, HLT_Jet30U trigger sample was used. The events from the good runs with unprescaled HLT_Jet30U trigger were considered and dijet mass spectra were measured. The ratio of the dijet mass spectrum between the dijet mass spectrum with HLT_Jet50U requirement and the dijet mass spectrum with HLT_Jet30U requirement gives the trigger efficiency of HTL_Jet50U trigger as a function of the dijet mass.

The HTL_Jet50U trigger becomes fully efficient when the dijet mass is equal to 220 GeV and it is shown on left in Fig.5.2. Thus, dijet mass spectrum was started from 220 GeV and the full efficient mass region was considered. In addition, The HLT_Jet50U trigger efficiency as a function of corrected transverse momentum of leading jet was investigated and it is illustrated on right in Fig.5.2. The HTL_Jet50U trigger becomes fully efficient when corrected p_T of leading jet is equal to 110 GeV.

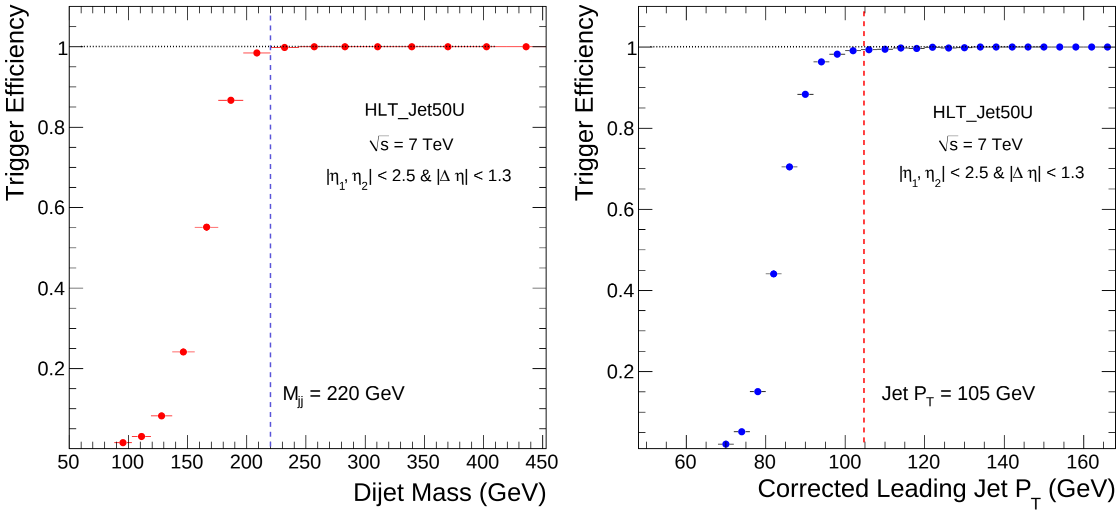

Figure 5.2. HLT_Jet50U trigger efficiency as a function of dijet mass (left) and as a function of corrected p_T of leading jet (right) is measured in data.

5.1.2 Data Quality

The number of events in the analysis after the basic cuts are shown for each cut in Table 5.1.

Cuts	Events	Fraction (%)
Events after pre-selection cut	6126910	100
Events after vertex cuts	6125930	99.98
Events after eta cuts	2088922	34.09
Events after dijet mass cut	414645	6.78
Events after jet id cut	414131	6.76

Table 5.1. Number of events and fraction of events after applying the selection cuts.

Only 514 events which were mostly HPD noise were rejected by the loose JetID cut and the fraction of events removed by JetID cut is very small. The requirement of kinematic cuts ($|\eta| < 2.5$ and $|\Delta\eta| < 1.3$) and dijet mass cut ($M_{jj} > 220$ GeV) give higher jet purity.

The distributions of the loose JetID variable are shown in Fig.5.3. Electromagnetic fraction of jet energy, Jet EMF, doesn't have a peak near zero or one which would indicate a problem from ECAL and HCAL, such as a hot channel in the calorimeter. The fraction of jet energy in the hottest HCAL HPD, Jet fHPD, doesn't show a peak near one which would indicate a problem from HCAL HPD noise. The number of energy ordered rechit containing at least 90% of the jet energy, Jet n90Hits, doesn't have any peak near one which would indicate a hot cell in the ECAL. These JetID variables distributions show that the jets don't originate from unphysical background.

Fig.5.4 shows number of good tracks associated with either of two leading jets. The track multiplicity distribution don't have a peak at zero which would indicate calorimeter background. The track multiplicity distributions show that the calorimeter jets are generated by pp collisions.

Some event balance distributions are illustrated in Fig.5.5. The dijet events have low $MET/SumE_T$ which indicates that the event energy is well balanced in the transverse plane. Backgrounds from cosmic rays, beam halo and detector noise are expected to occasionally produce events with large or unbalanced energy deposition, which is not observed in this data. The events with $MET/SumE_T > 0.5$ look like monojet events with low second jet energy produced by QCD radiation. These events probably are from $W(\mu\nu) + jet$ or $Z(\nu\nu) + jet$. Two leading jets are mostly back-to-back in ϕ space as expected for dijet events. The tails to small and large values of $\Delta\phi$ are produced by QCD radiation and multijet events. These distributions show that observed events are with dijet topology.

Fig.5.6 shows some basic jet kinematic variables distributions. Transverse momenta of leading and second jets for data and MC are in good agreement. The η and ϕ distribution of two leading jets are in reasonable agreement. The $\eta - \phi$ distribution of two leading jets is uniform and doesn't show any hot or dead regions of the calorimeters. The $\cos(\theta^*)$ distribution is in good agreement with PYTHIA (Sjostrand, 2006) QCD and is symmetrical around zero and peaks at forwards, corresponding to 2 → 2 Rutherford scattering.

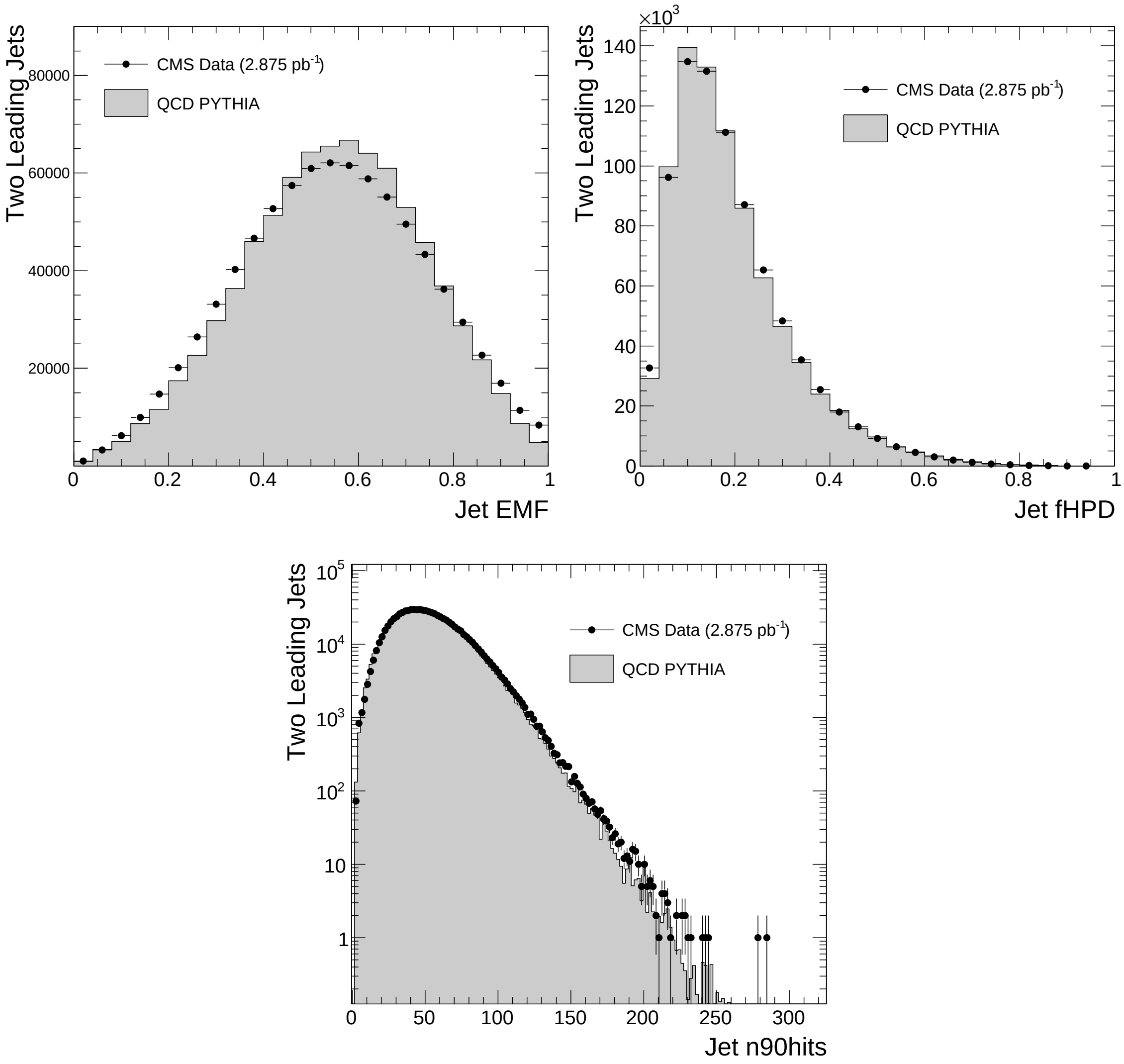

Figure 5.3. Jet ID Distributions. The EM energy fraction of the two leading jets (upper left), the fHPD for the two leading jets (upper right), the n90hits for the two leading jets (lower).

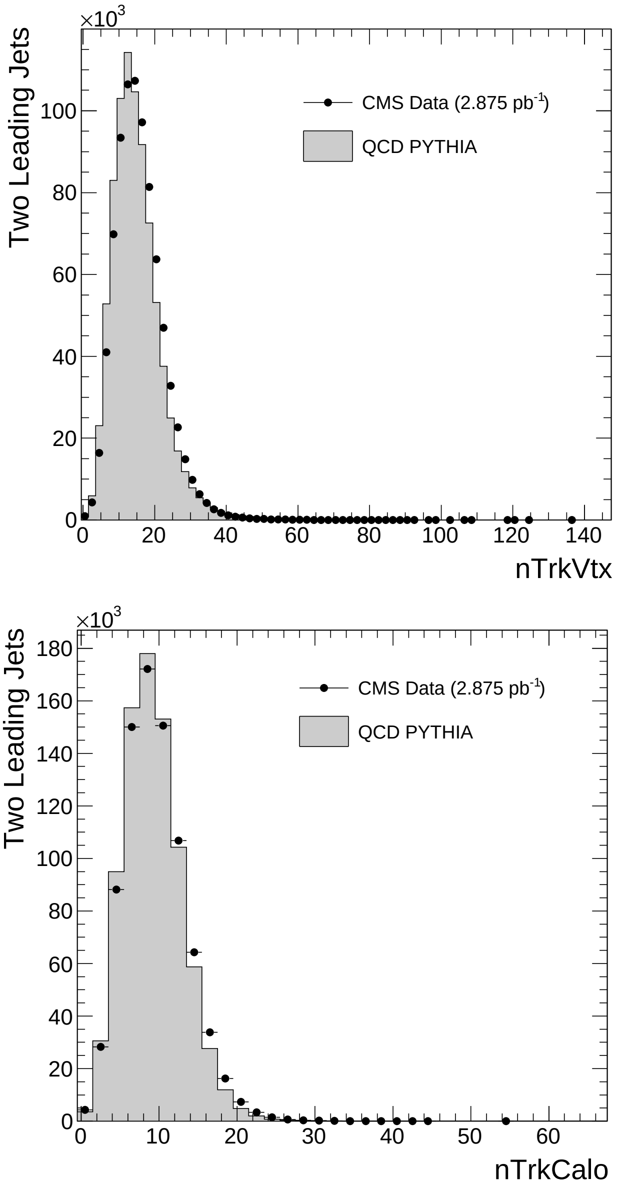

Figure 5.4. The multiplicity of tracks associated to two leading jets at the vertex (top) and at the calo face (bottom).

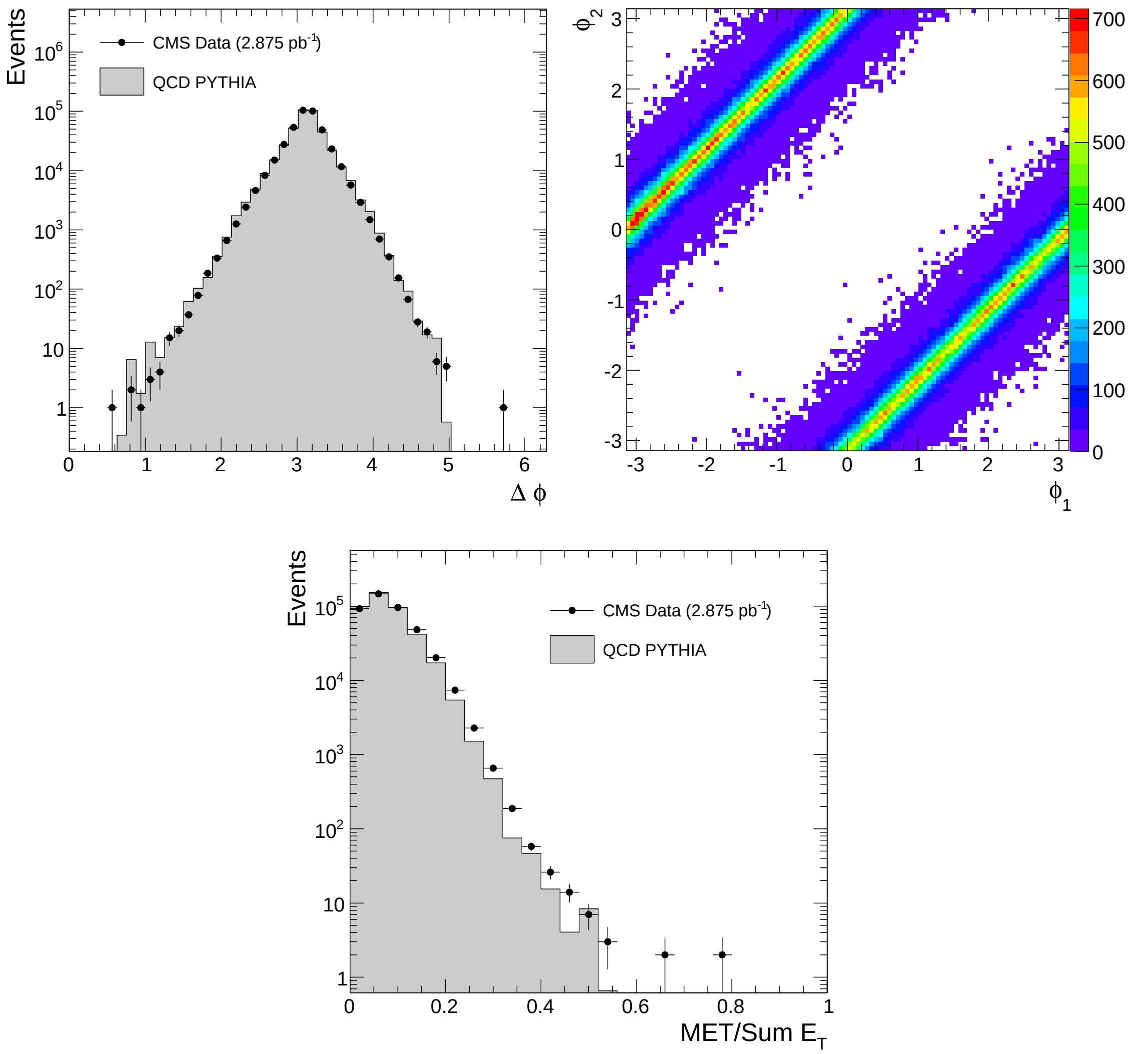

Figure 5.5. Event balance distributions. The ϕ difference between two leading jets (upper left) and ϕ_1 vs ϕ_2 distribution (upper right). The missing transverse energy in the calorimeters divided by total calorimeter transverse energy (lower).

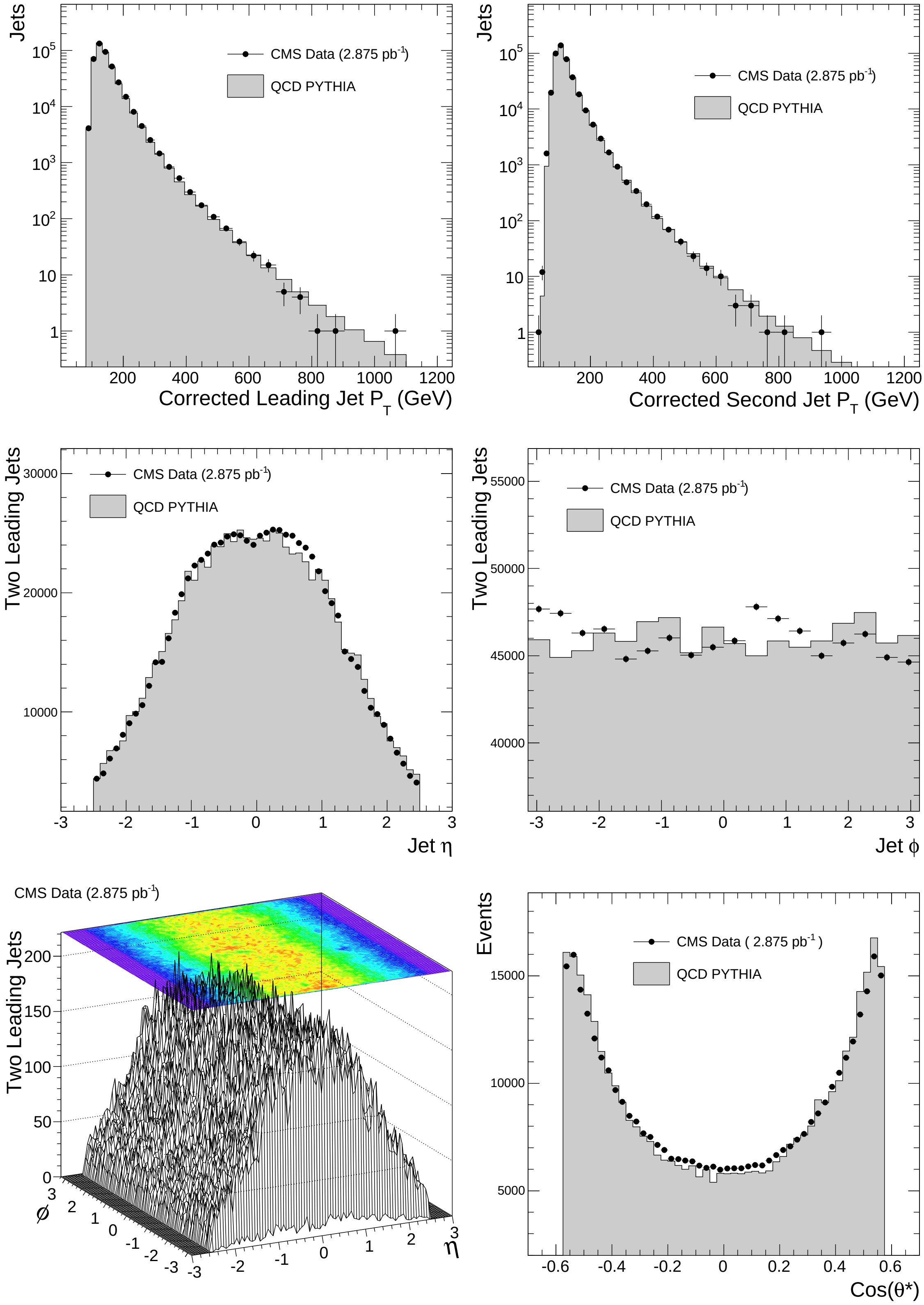

Figure 5.6. Jet kinematics distributions. The corrected P_T of leading jet (upper left) and second jet (upper right). The η (middle left) and ϕ (middle right) distributions of two leading jets. η vs ϕ distribution of two leading jets (lower left). The cos (θ*) distribution (lower right).

5.1.3 Data Stability

The data quality shows good stability as a function of run numbers. The observed cross section which is defined as the number of dijet events divided by the corresponding integrated luminosity of each run is illustrated in Fig.5.7. The observed cross section is stable around 142 nb with RMS of 2%. The observed cross section stability is an indication of a stable calorimeter energy scale and luminosity evaluation. In Fig.5.8, average dijet mass for each run is shown. The runs with integrated luminosity greater than 1 nb^{-1} are considered. Average dijet mass distribution has a good stability around 280 GeV. Missing calorimeter energy divided by total calorimeter energy for each run are shown in Fig.5.9. There is a good stability for energy balance in transverse space. The stability plots for some jet properties are illustrated in Fig.5.10. Overall, the data shows a good stability.

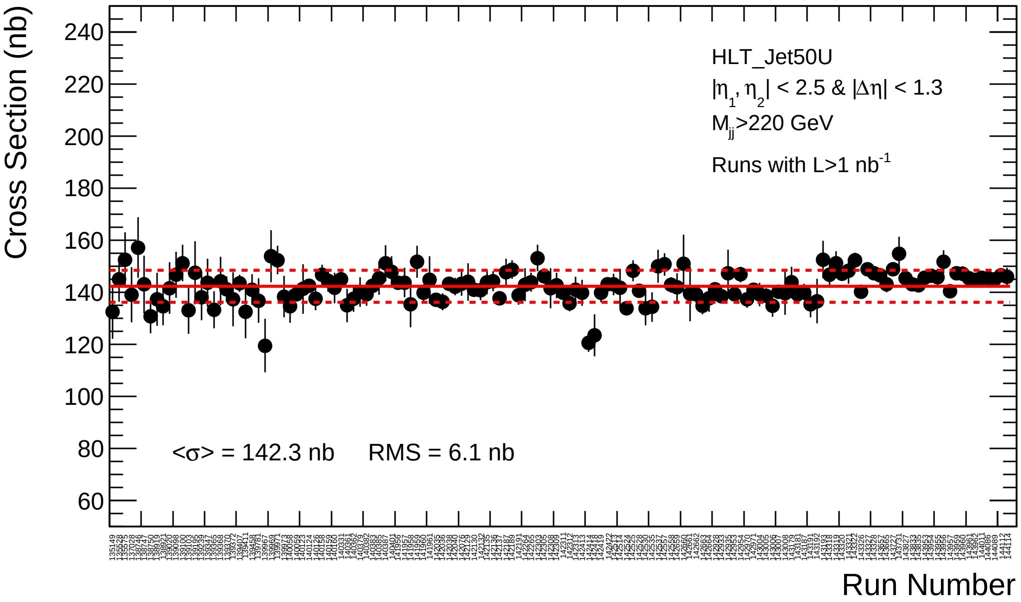

Figure 5.7. Number of dijet events passing the full selections, divided by the integrated luminosity of each run, vs. run. Only runs with integrated luminosity greater than 1 nb^{-1} passing the analysis selection are shown.

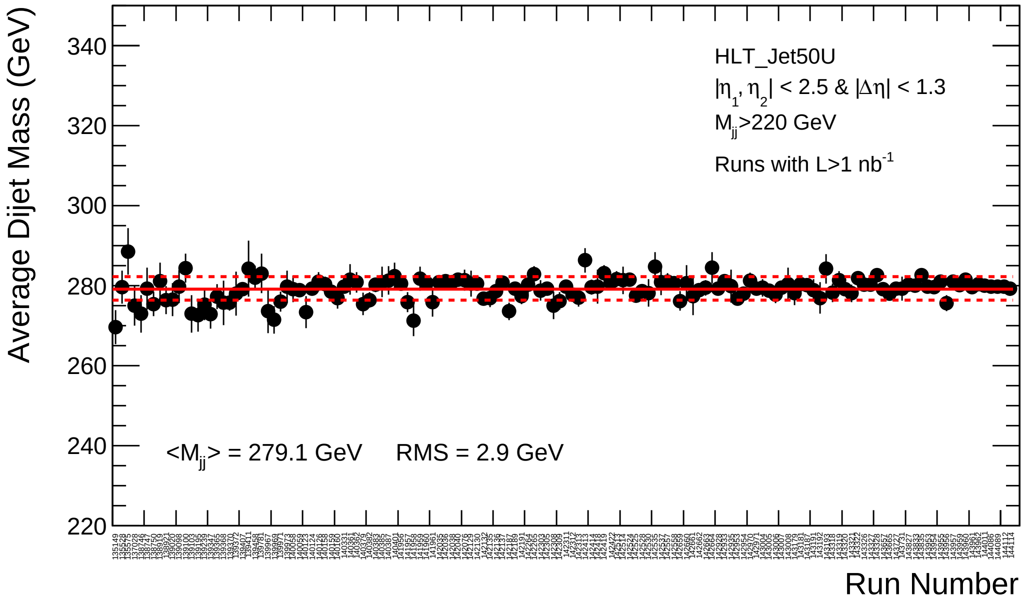

Figure 5.8. Mean dijet mass vs run with integrated luminosity greater than 1 nb^{-1}.

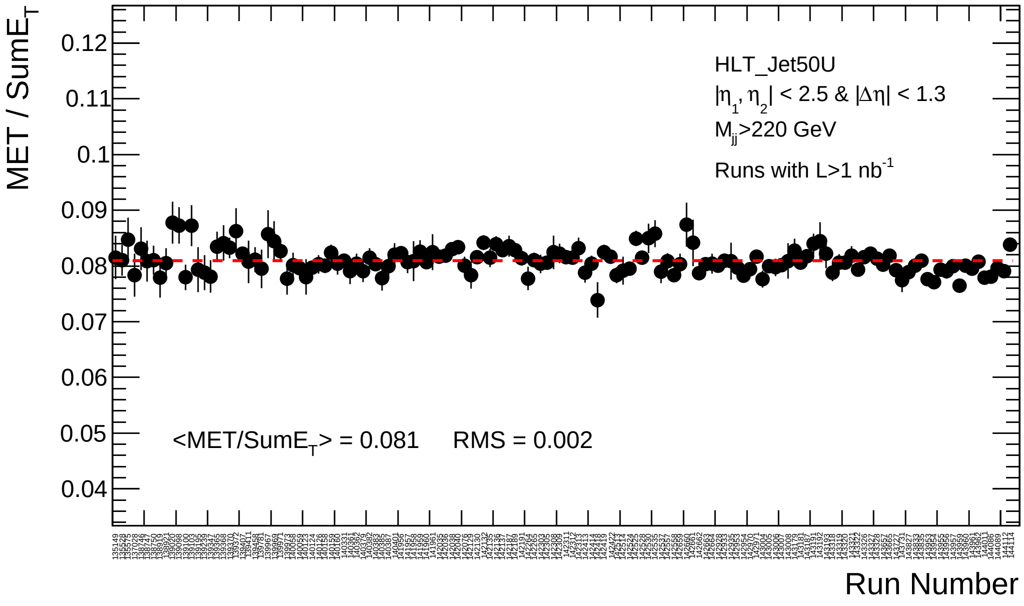

Figure 5.9. Missing calorimeter energy divided by total calorimeter energy vs. run with integrated luminosity greater than 1 nb^{-1}.

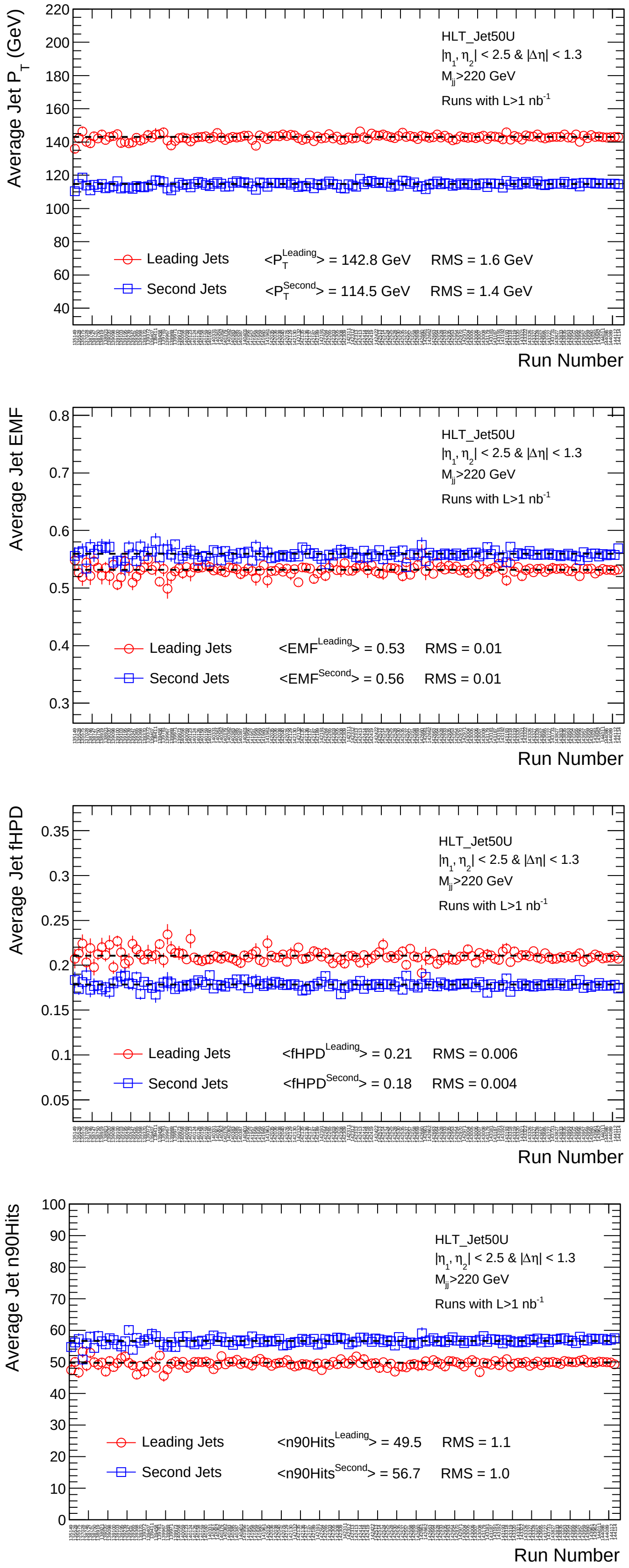

Figure 5.10. Mean value of jet properties for the leading jet (open red circles) and the second jet (open blue squares) vs. run with integrated luminosity greater than 1 nb^{-1}.

5.2 Dijet Mass Spectrum and QCD

The measured dijet mass spectrum is shown in Fig.5.11. The dijet mass spectrum is formed by;

$$\frac{d\sigma}{dm} = \frac{1}{\int Ldt}\frac{N_i}{\Delta m_i} \tag{5.1}$$

where m is the dijet mass, N_i is the number of events in the i-th dijet mass bin, and Δm_i is the width of the i-th dijet mass bin, and the integrated luminosity is $\int Ldt$. Variable dijet mass bins roughly equal to dijet mass resolution are used. The data is compared to a QCD prediction from the PYTHIA MC and full CMS simulation. Spring10 QCD PYTHIA MC samples are used with the $\hat{p}_T$ boundaries (/QCDDiJet_PtXXtoYY/Spring10-START3X_V26_S09-v1/GEN-SIM-RECO) and CTEQ6L1 (Pumplin, 2002) parton distribution function is considered. Both data and QCD MC are normalized assuming integrated luminosity of 2.875 pb^{-1}. Fig.5.11 also shows the sensitivity of the QCD+CMS simulation to a 10% systematic uncertainty on the jet energy scale.

The horizontal error bars on data are the bin width, the vertical error bars are Gaussian and Poisson uncertainties. Poisson uncertainties are used where N_i is less than 25, and Gaussian uncertainties are used where N_i is equal or greater than 25. The bins with zero events are indicated by a Poisson vertical error bar extending up to 1.8 events.

In Fig. 5.12, the ratio of the data to the QCD MC prediction is illustrated. The PYTHIA QCD MC prediction is in good agreement with the data. The data points and corresponding uncertainty are listed in Table 5.2.

5.3 Dijet Mass Spectrum and Fit

Dijet mass spectrum is compared to a fit in Fig.5.13. The parametrization of smooth fit function is

$$\frac{d\sigma}{dm} = p_0\frac{(1-X)^{p_1}}{X^{p_2+p_3\ln(X)}} \tag{5.2}$$

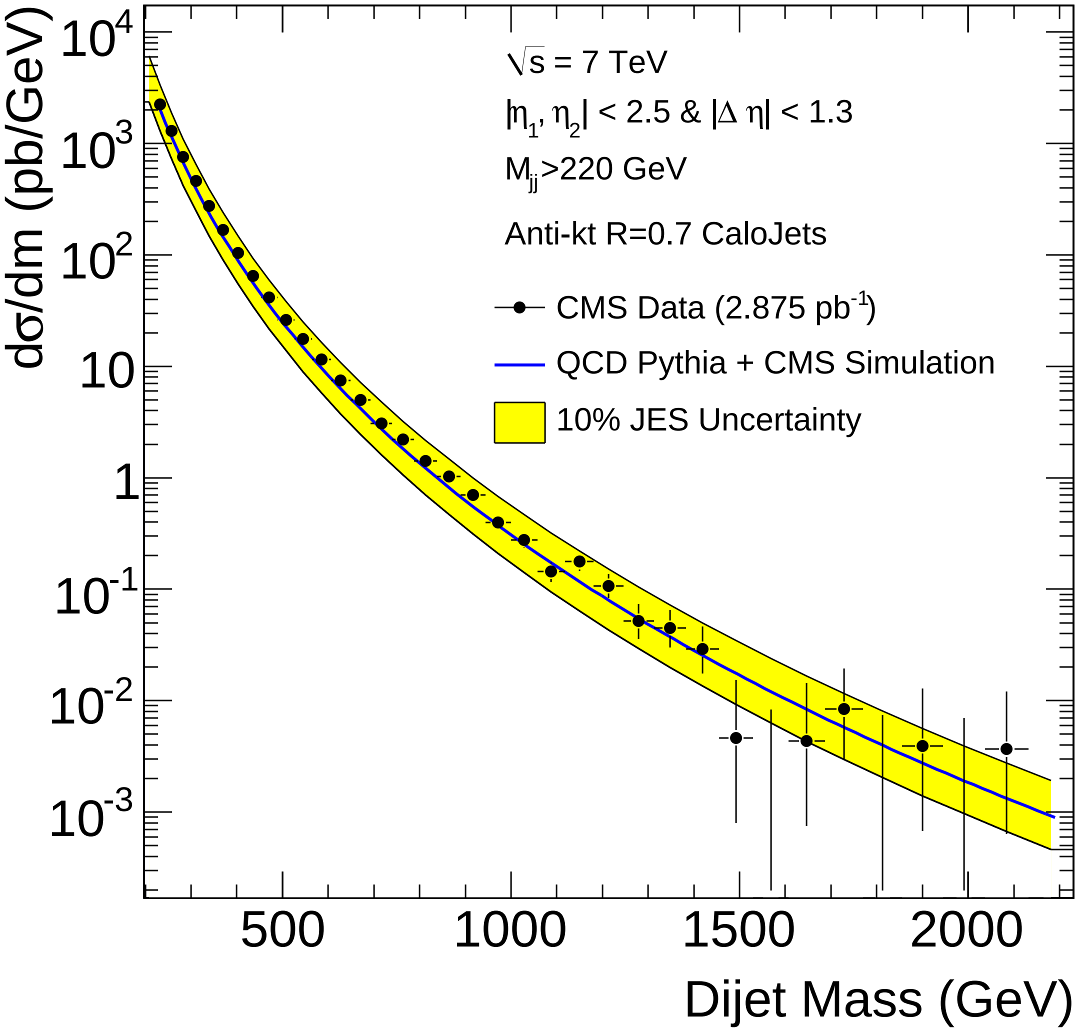

Figure 5.11. The dijet mass spectrum data (points) is compared to a QCD MC prediction (solid line). The band shows the sensitivity to a 10% systematic uncertainty on the jet energy scale.

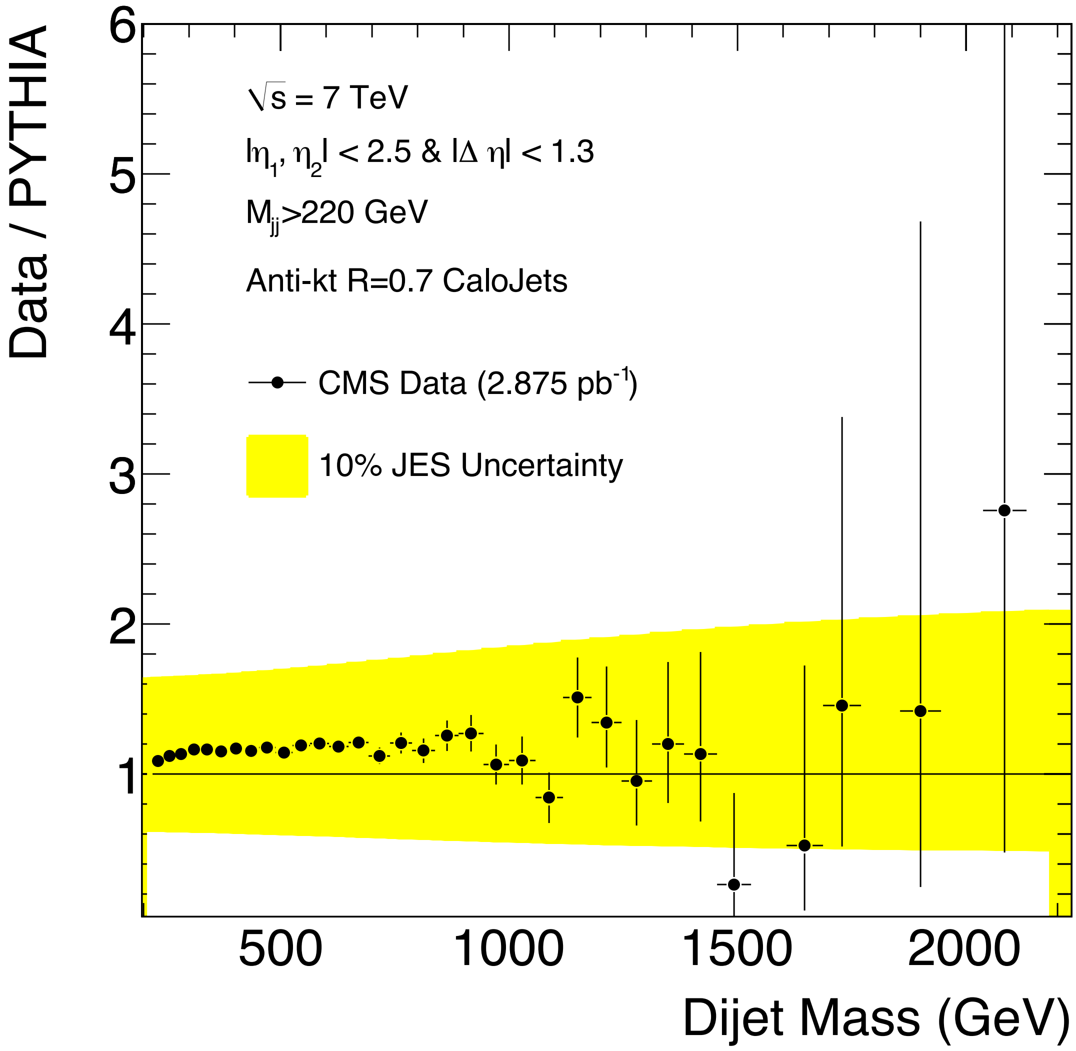

Figure 5.12. The dijet mass spectrum data (points) divided by the QCD PYTHIA prediction. The band shows the sensitivity to a 10% systematic uncertainty on the jet energy scale.

where $X = m/\sqrt{s}$ and $p_{0,1,2,3}$ are free parameters (Aaltonen, 2009). The $(1-X)$ term is motivated by the parton distribution fall off with fractional momentum. The $X^{-p_3 \ln(x)}$ factor describes the high dijet mass part of the QCD spectrum. The χ^2 for the fit over the dijet mass range $220 < m_{jj} < 2100$ GeV is 32.33 for 31 degrees of freedom.

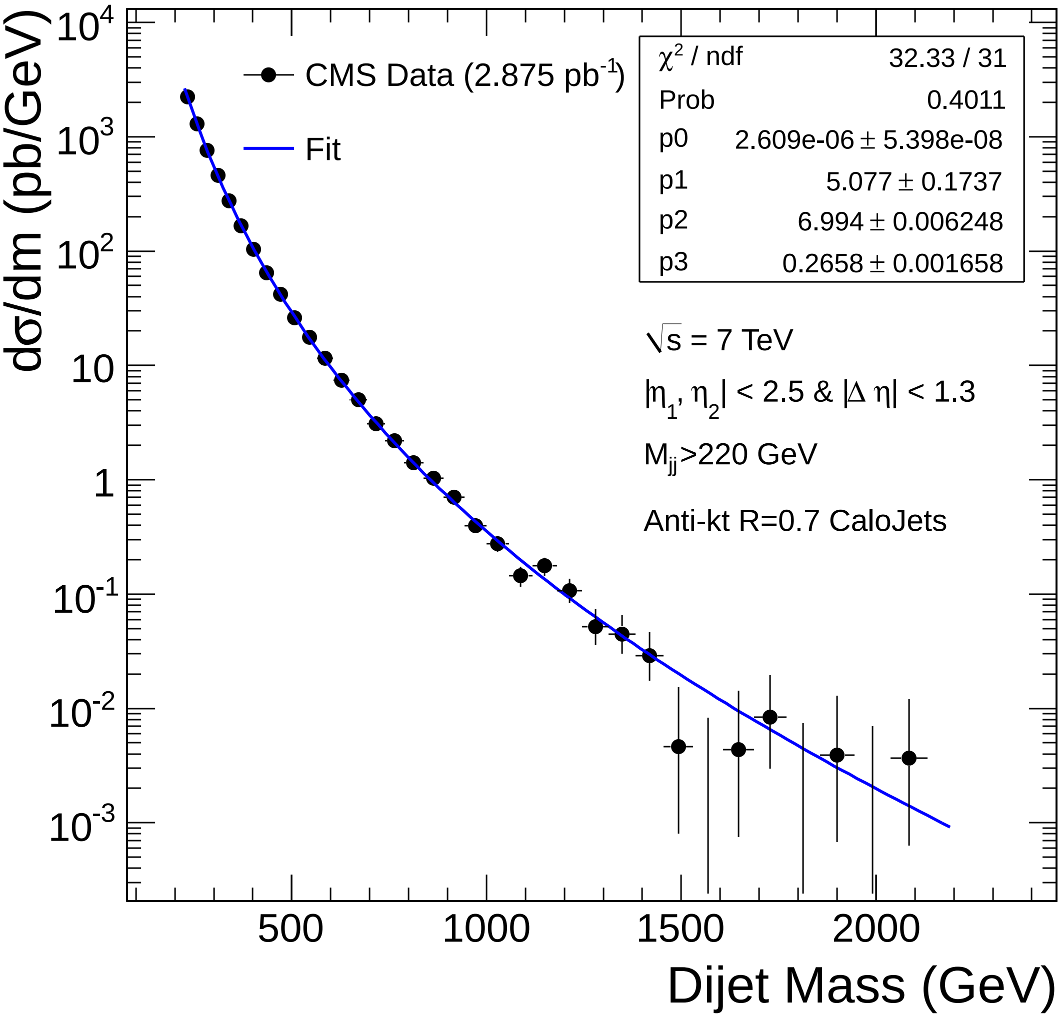

Figure 5.13. The dijet mass spectrum data (points) is compared to a smooth background fit (solid curve)

Fig.5.14 shows fractional differences between data and the fit function, (Data-Fit)/Fit, which indicate no significant evidence of peaks above the background fit. The largest upward fluctuation observed will be discussed in Chapter 6.3. The pulls, defined as (Data-Fit)/Error, also are shown in Fig.5.14. The residuals are consistent with statistical fluctuation and oscillating around zero. In the pulls plot, the error bars are set as exactly 1, because they are in units of the error in the bin.

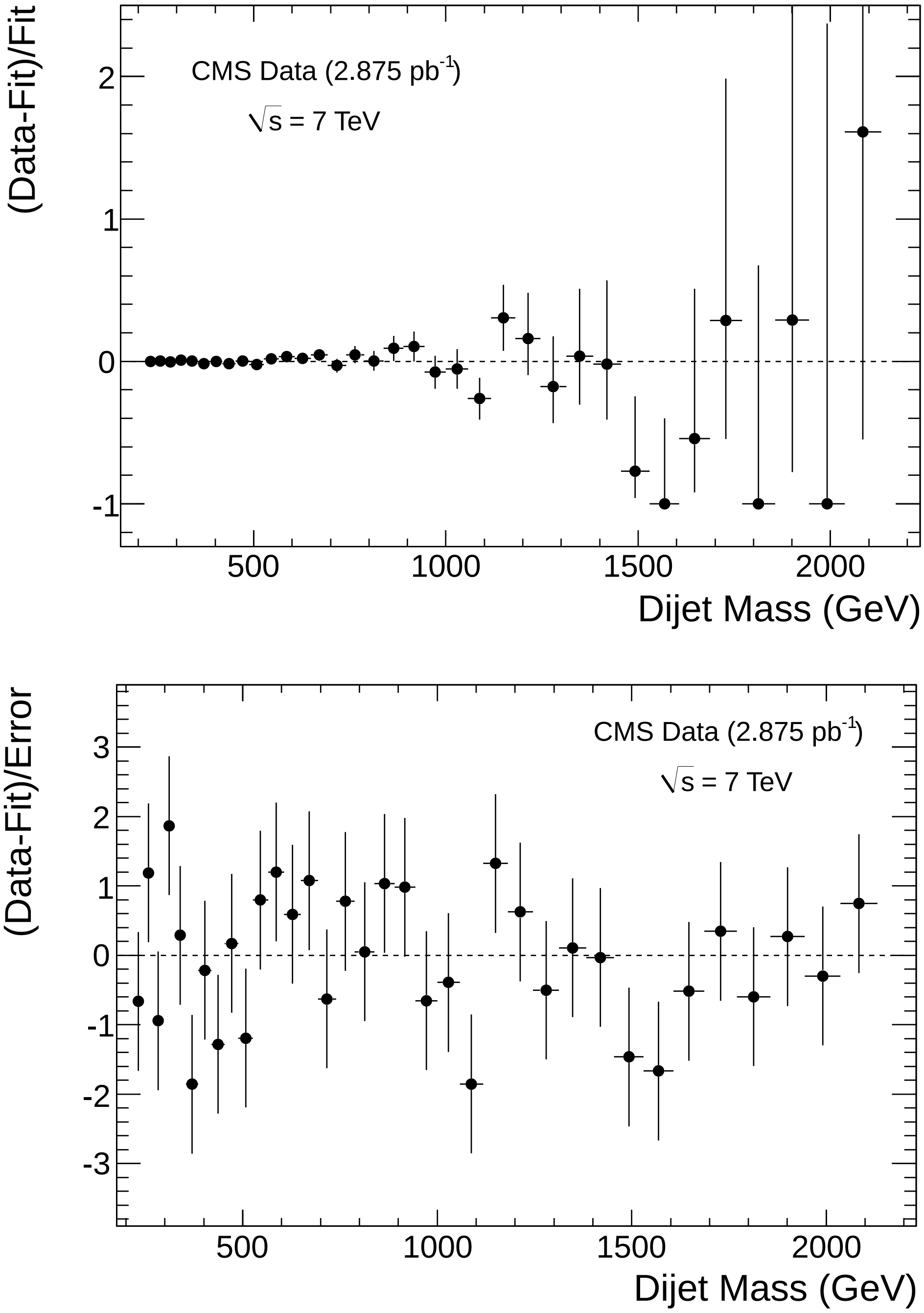

Figure 5.14. The fractional difference between the dijet mass distribution (points) and a smooth background fit as a function of dijet mass (top). The pulls distribution (Data-Fit)/Error as a function of dijet mass (bottom).

5.3.1 Fit to Dijet Mass Spectrum with Various Parameterizations

In addition to the default fit, two alternate functional forms are considered. Those alternate functional forms are listed in Equation 5.3.

$$
\begin{aligned}
\frac{d\sigma}{dm} &= \frac{P_0 \cdot (1-X)^{p_1}}{X^{p_2+p_3 ln(X)}} \text{ (Default Fit with 4-parameters).} \\
&= \frac{P_0 \cdot \left(1 - X + P_3 \cdot X^2\right)^{P_1}}{m^{P_2}} \text{ (Alternate Fit A with 4-parameters).} \\
&= \frac{P_0 \cdot (1-X)^{P_1}}{m^{P_2}}, \text{ (Alternate Fit B with 3-parameters)}
\end{aligned}
\tag{5.3}
$$

where $X = m/\sqrt{s}$. The dijet mass spectrum is shown fitted by three different forms. All alternate functions give a reasonable fit of the data. The default four parameter function was used by CDF in the Run II (Aaltonen, 2009) and is used by ATLAS (Aad, 2010). It gives a good fit with the best $\chi^2/NDF = 32.3/31$. Alternate fit A is a four parameter function that was used by CDF in Run IB (Abe, 1997). The goodness of fit, $\chi^2/NDF = 36.8/31$, is significantly worse than the default fit. Alternate fit B is a three parameter fit which was used by CDF in Run IA (Abe, 1995). The goodness of fit, $\chi^2/NDF = 39.3/32$, is the worst in all of the considered fit functions.

The dijet mass distribution is compared to all considered fits in Fig.5.15. Fig.5.16 shows a comparison between all three fits as fractional differences between data and fit function and the pulls.

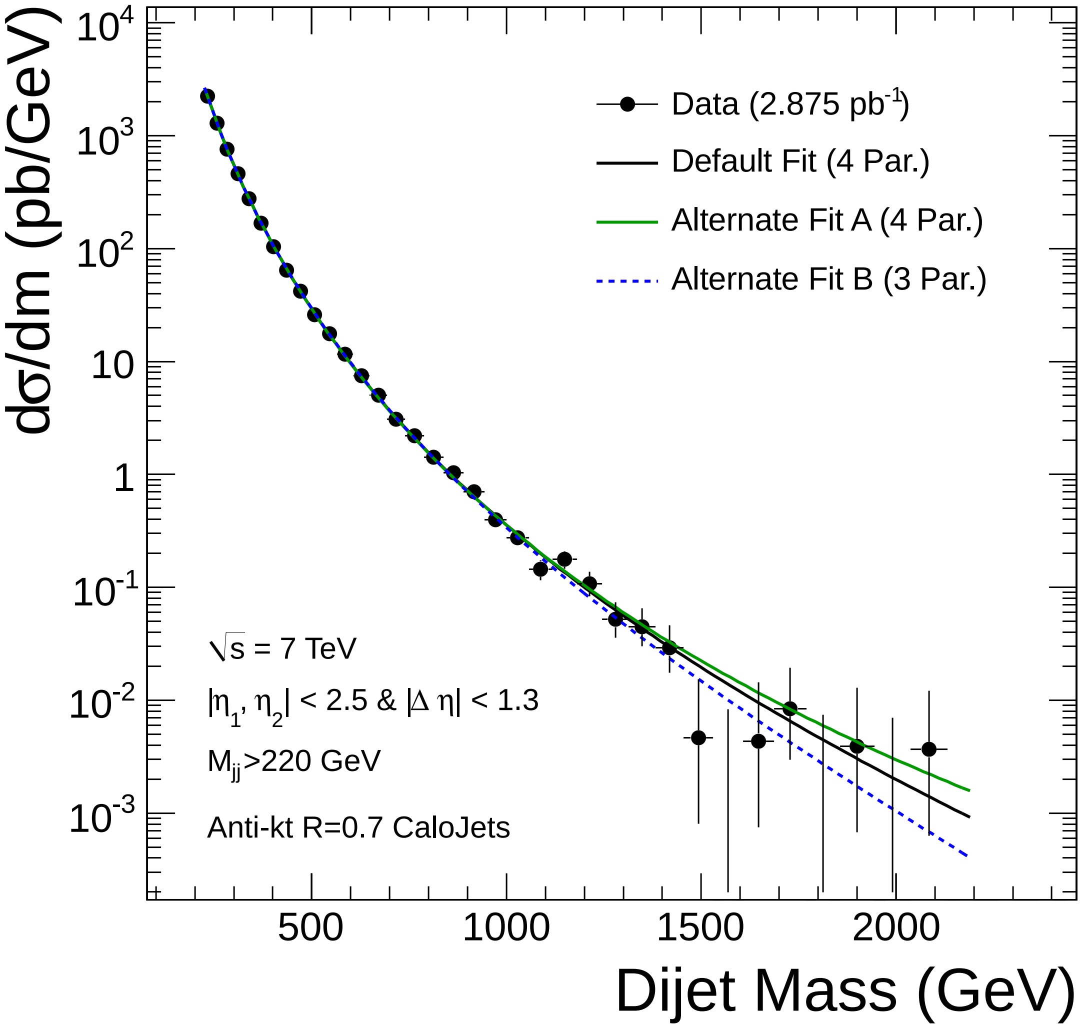

Figure 5.15. The dijet mass spectrum data (points) is compared to fits (solid curves) using default fit function and the other alternate fit functions.

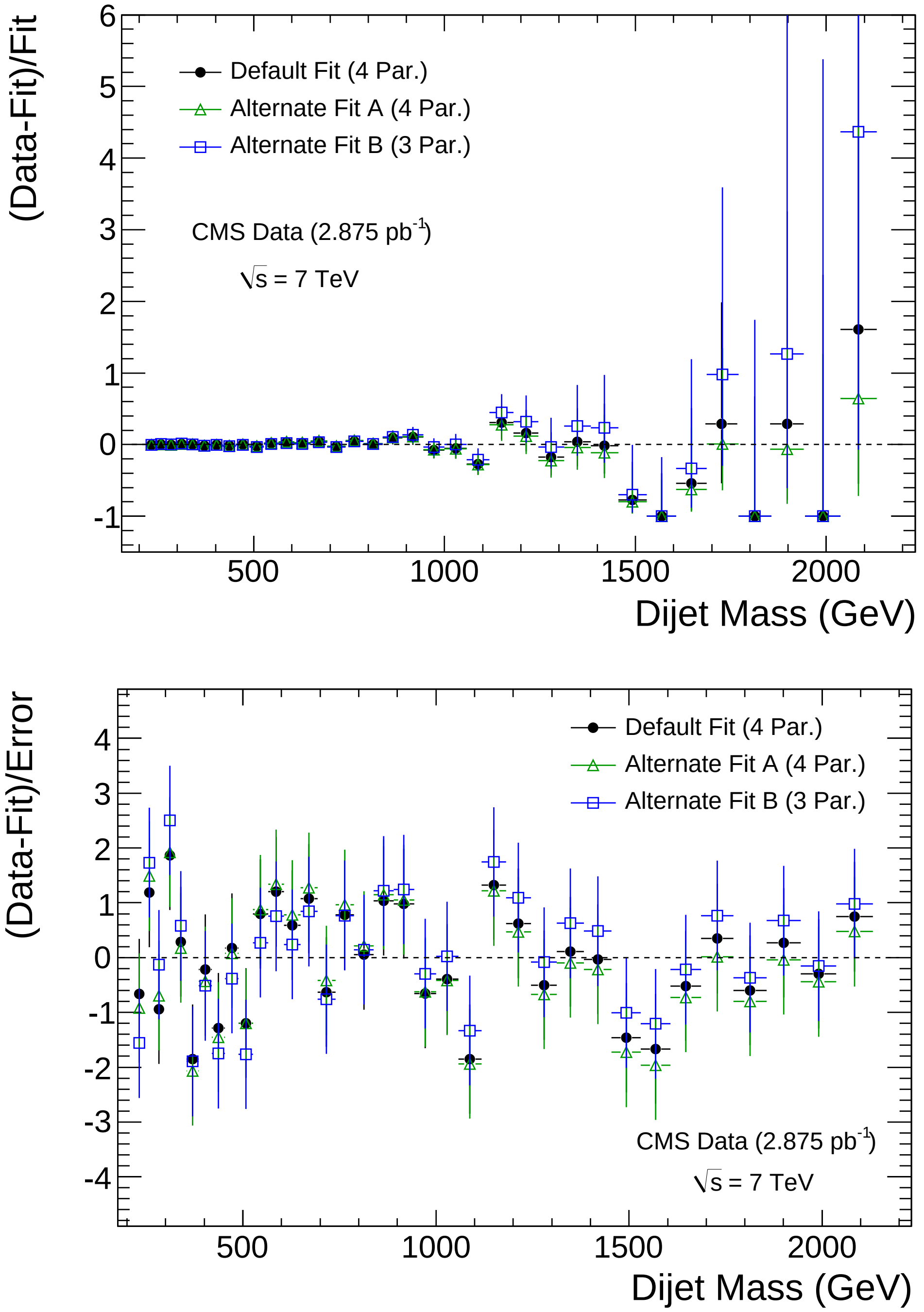

Figure 5.16. Fractional difference (points) between the dijet mass distribution data and three fits as a function of dijet mass (top). Pulls for the data (points) compared to three fits as a function of the dijet mass (bottom).

Low Edge (GeV)	Bin Width (GeV)	Events	$d\sigma/dm$ (pb/GeV)	Low Edge (GeV)	Bin Width (GeV)	Events	$d\sigma/dm$ (pb/GeV)
220	24	154283	2235.99 ± 5.693	890	54	109	0.7021 ± 0.0672
244	26	96774	1294.64 ± 4.162	944	56	64	0.3975 ± 0.0497
270	26	56703	758.57 ± 3.186	1000	58	46	0.2759 ± 0.0407
296	29	38360	460.09 ± 2.349	1058	60	25	0.1449 ± 0.0290
325	29	23071	276.71 ± 1.822	1118	63	32	0.1767 ± 0.0312
354	32	15359	166.95 ± 1.347	1181	65	20	$0.1070^{+0.0297}_{-0.0237}$
386	33	9886	104.20 ± 1.048	1246	67	10	$0.0519^{+0.0221}_{-0.0161}$
419	34	6308	64.532 ± 0.813	1313	70	9	$0.0447^{+0.0204}_{-0.0146}$
453	36	4318	41.720 ± 0.635	1383	72	6	$0.0290^{+0.0173}_{-0.0115}$
489	37	2774	26.078 ± 0.495	1455	75	1	$0.00464^{+0.0107}_{-0.0038}$
526	39	1970	17.570 ± 0.396	1530	77	0	$0^{+0.0083}_{-0.0}$
565	41	1365	11.580 ± 0.313	1607	80	1	$0.00435^{+0.0099}_{-0.0036}$
606	43	921	7.4499 ± 0.245	1687	83	2	$0.00838^{+0.0110}_{-0.0054}$
649	44	635	5.0198 ± 0.199	1770	86	0	$0^{+0.0074}_{-0.0}$
693	47	416	3.0786 ± 0.151	1856	89	1	$0.00391^{+0.0090}_{-0.0032}$
740	48	304	2.2029 ± 0.1263	1945	92	0	$0^{+0.0070}_{-0.0}$
788	50	203	1.4121 ± 0.0991	2037	95	1	$0.00366^{+0.0084}_{-0.0030}$
838	52	154	1.0301 ± 0.0830	2132	99	0	$0^{+0.0065}_{-0.0}$

Table 5.2. For each bin of dijet mass data listed the lower bin edge, the bin width, the number of events, the observed differential cross section, and an estimate of the statistical uncertainty from Gaussian and Poisson statistics.

6. SEARCH FOR DIJET RESONANCES

In this chapter, searching for dijet resonances will be discussed. The model-independent generic upper limit on cross section calculation will be covered.

6.1 The Signal Modeling

Three generic shapes are considered for each type of parton pair in the resonance decay (quark-quark (qq), quark-gluon (qg) and gluon-gluon (gg)). To obtain generic shapes for these three types parton pair, the process of $q* \rightarrow qg$, $G \rightarrow q\bar{q}$ and $G \rightarrow gg$ were produced using PYTHIA+CMS Spring10 simulation at five different masses of 0.5, 0.7, 1.2, 2 and 3.5 TeV. The Fig.6.1 shows the dijet mass distribution of excited quarks for GenJets, CaloJets and Corrected CaloJets at three different resonance masses. The peak of resonance shapes of GenJets and Corrected CaloJets are roughly at the expected resonance mass. The resonance shape of corrected calojet is wider than genjets due to detector smearing effect. The low mass tail in the resonance shape comes predominantly from final state radiation (FSR) and the high mass tail is enhanced by initial state radiation (ISR).

Fig.6.2 shows the resonance shapes at mass of 1.2 TeV resonance of type qq, qg and gg. These resonance shapes are approximately valid for any resonance model because the natural half-width ($\Gamma/2$) of models is small compared to the dijet mass resolution. Since gluons emit more radiation than quarks, the width of dijet resonances increases with the number of gluons in the final state. The peak value of dijet mass of the resonance decrease with the number of gluons in the final state because CMS detectors have lower response to gluon jets than quark jets. Thus, the shape of gluon-gluon resonance is the widest and shifted to lower dijet mass region. Fig.6.3 shows simulated excited quark (qg) signals at various resonance masses. An interpolation technique was used to obtain the resonance shape at intermediate masses. This technique is discussed in Appendix C. An estimated resolution of Gaussian core of the dijet mass response as a function of resonance mass is illustrated in Fig. 6.4. The resolution is well fit by the function of

$$\frac{\sigma}{Mean} = P_0 + \frac{P_1}{M_{Res}} \tag{6.1}$$

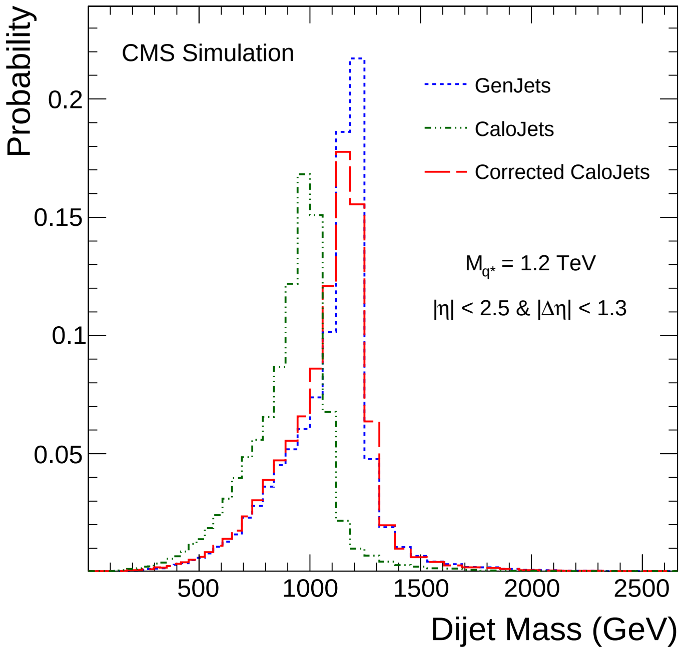

Figure 6.1. Dijet mass distribution for quark-gluon resonance at mass of 1.2 TeV of GenJets, CaloJets and Corrected CaloJets.

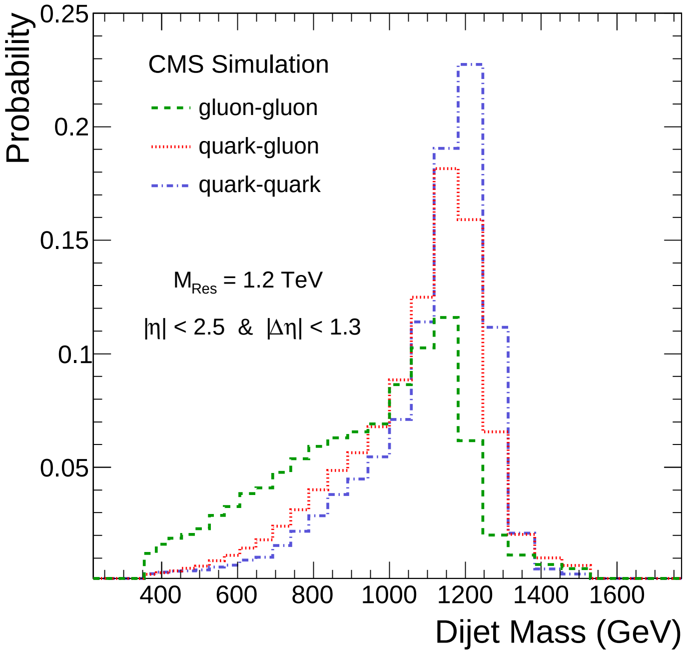

Figure 6.2. Dijet mass distribution for *qq*, *qg* and *gg* resonance at mass of 1.2 TeV.

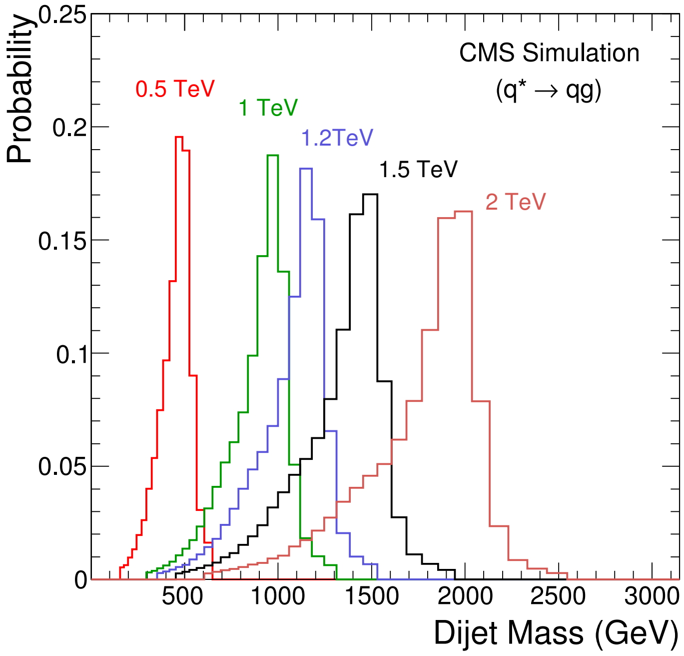

Figure 6.3. Simulated excited quark signals at resonance mass of 0.5, 1.0, 1.2, 1.5 and 2.0 TeV.

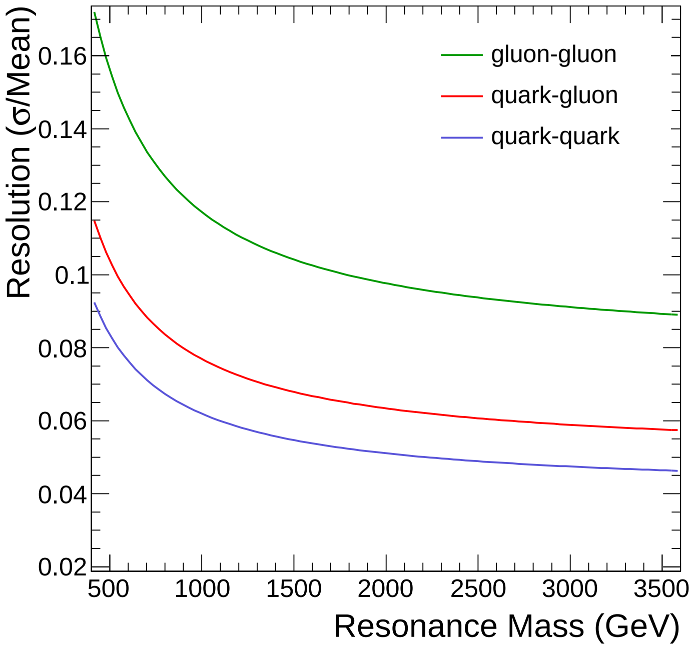

Figure 6.4. The dijet mass gaussian core resolution as a function of resonance mass from CMS simulation of qq, qg and gg resonances.

where M_{Res} is the resonance mass and P_0 and P_1 are free parameters. The free parameters of the fit are $P_0 = 4.02 \cdot 10^{-2}$ and $P_1 = 21.7$ for qq resonances, $P_0 = 4.99 \cdot 10^{-2}$ and $P_1 = 27.0$ for qg resonances, and $P_0 = 7.81 \cdot 10^{-2}$ and $P_1 = 39.0$ for gg resonances. The resolution varies from 11% at 0.5 TeV to 6% at 3.5 TeV for qg resonances.

Fig.6.5 shows the differential cross section of excited quark signals and string resonance signals as a function of dijet mass on data with QCD MC prediction and fit. The string resonance line shape is modeled using excited quark line shape since string resonance decays into a quark and a gluon predominantly (74%).

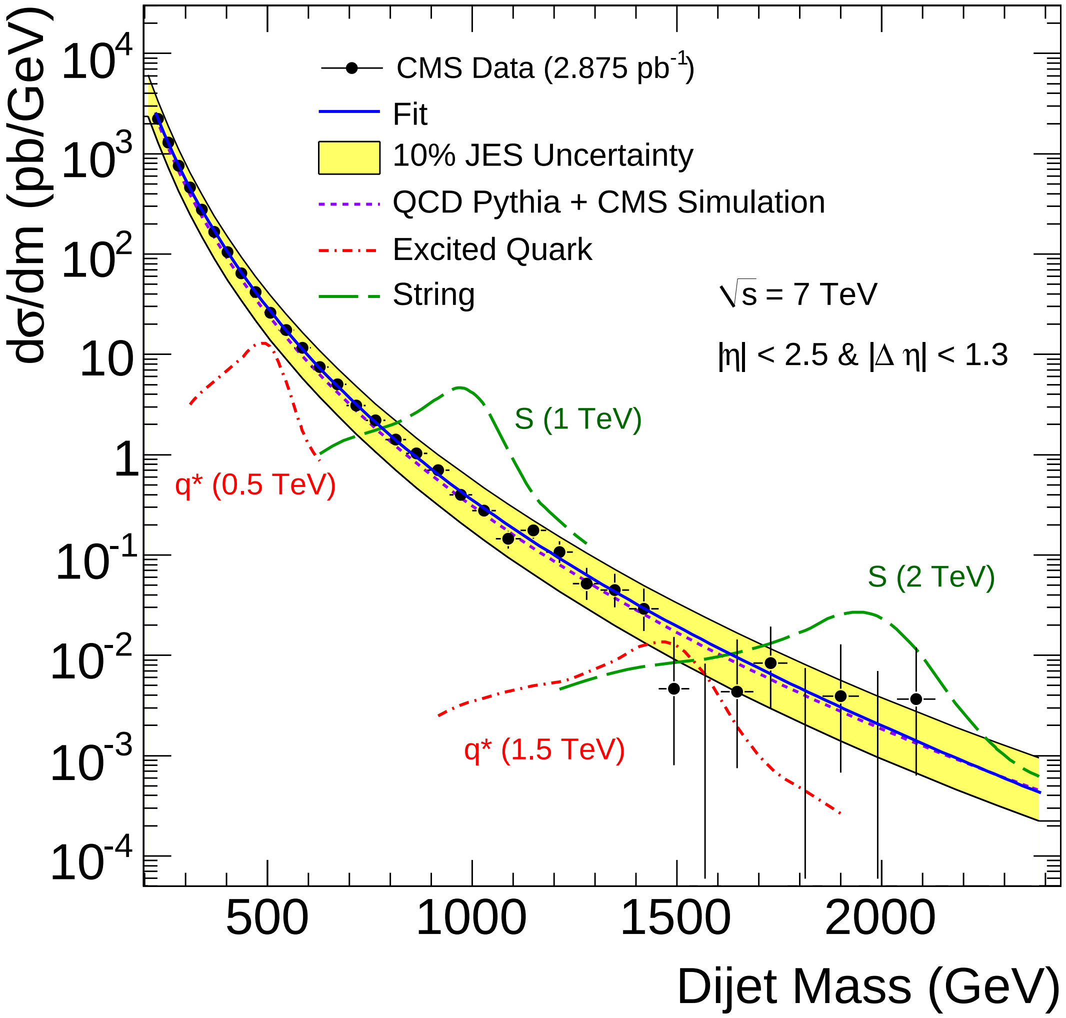

Figure 6.5. The dijet mass distribution (points) compared to a smooth background fit (blue solid line), to a QCD PYTHIA prediction (purple dashed line), to simulated excited quark signals (red dot-dashed curves) and to simulated string resonance signals (green long dashed curves).

The ratio between the data and fit compared to simulated excited quark and string resonance signals are shown in Fig.6.6. Excited quark signals with resonance mass less than roughly 1.5 TeV could be seen or excluded based on Fig.6.6.

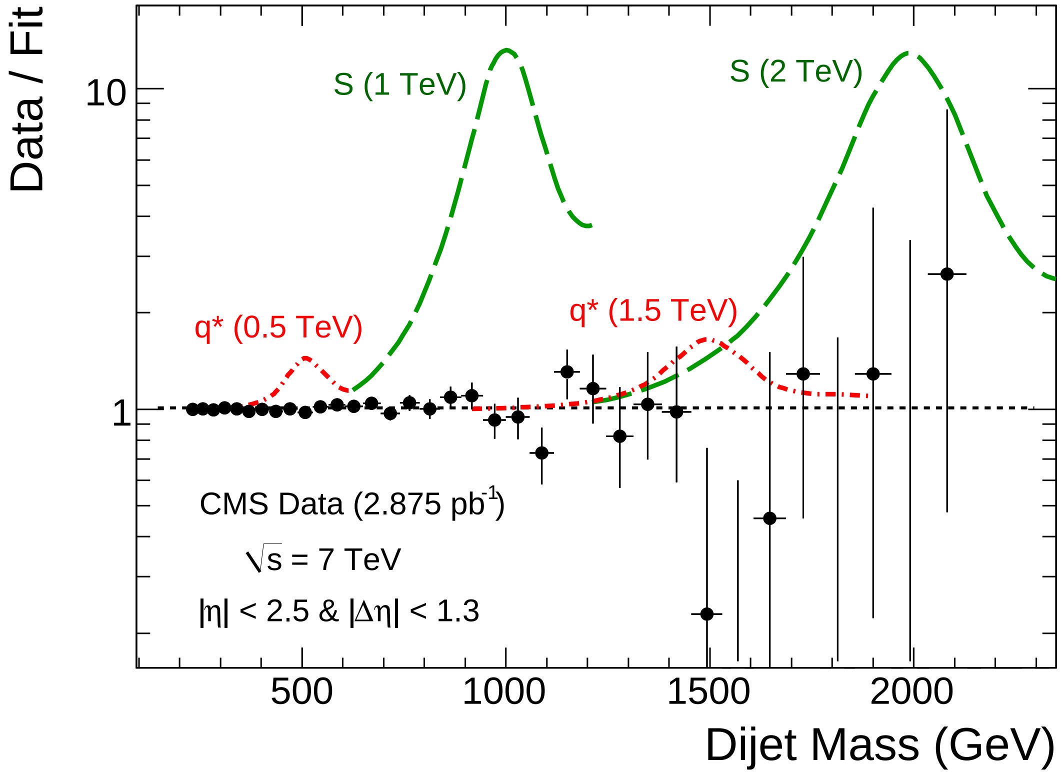

Figure 6.6. The ratio between the dijet mass distribution (points) and smooth background fit (dashed line) compared to simulated excited quark (red dashed curves) and string resonance (green long dashed curves) signals.

6.2 Eta Cut Optimization

A two parton system is shown in Fig.6.7. The kinematics of the two jets in the parton-parton center of mass are given in terms of the observed pseudo-rapidities by (Ellis, 1996):

$$\eta_{boost} = \frac{1}{2}(\eta_1 + \eta_2) \tag{6.2}$$

$$\eta^* = \frac{1}{2}(\eta_1 - \eta_2) \tag{6.3}$$

$$\eta_{LAB} = \eta^* + \eta_{boost} \tag{6.4}$$

The center of mass scattering angle θ^* for a parton is given by,

$$\cos\theta^* = \tanh(\eta^*) = \tanh(\frac{\Delta\eta}{2}) \tag{6.5}$$

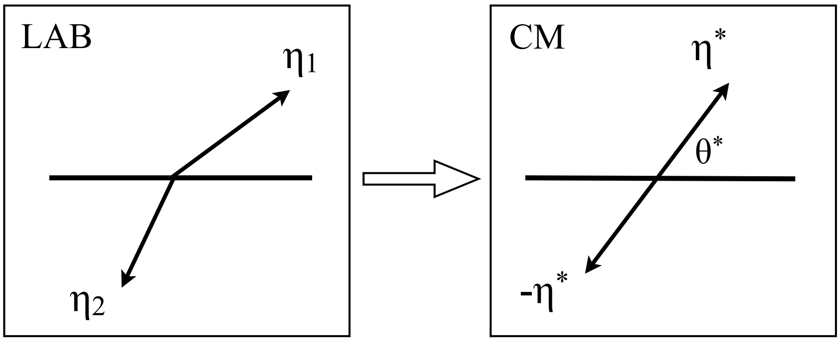

Figure 6.7. LAB and CM frame of a two parton system.

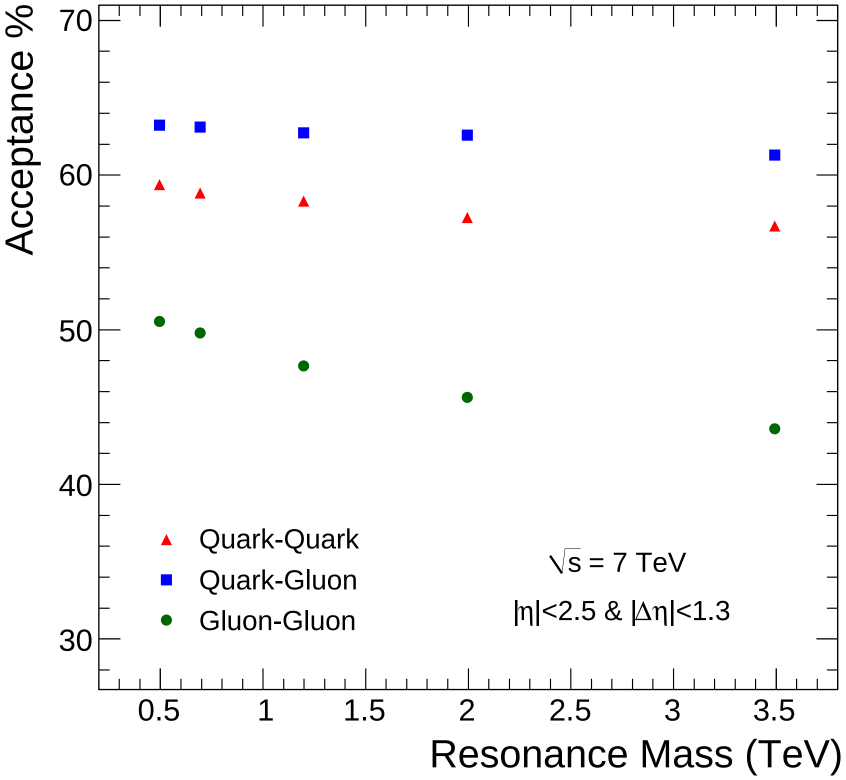

Figure 6.8. The acceptance for *qq* (blue square), *qg* (red triangle) and *gg* (green circle) resonances.

The θ^* distribution have the similar Rutherford scattering at small angle with exchanging a gluon in the t-channel.

$$\frac{d\hat{\sigma}}{d\cos\theta^*} \approx \frac{1}{(1-\cos\theta^*)^2} \tag{6.6}$$

For QCD t-channel scattering, $\cos\theta^*$ is close to one ($\cos\theta^* \approx 1$). To remove QCD t-channel pole in center-of-mass, a kinematic cut as $|\Delta\eta| < 1.3$ (or $\cos\theta^* < 0.57$) is required. It suppresses QCD processes significantly more than dijet resonances.

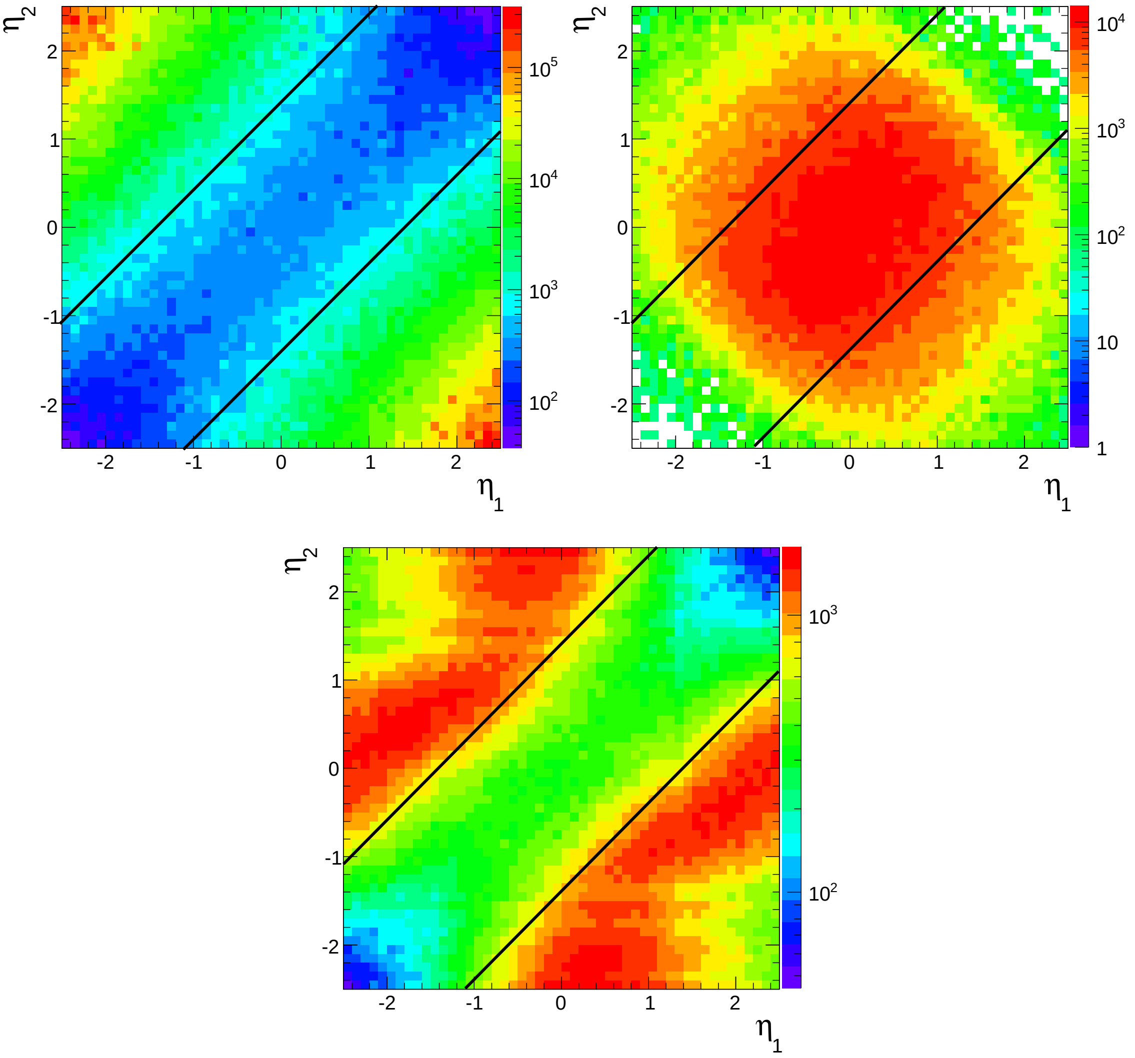

Figure 6.9. $\eta_1 - \eta_2$ distribution of two leading jets for PTYHIA QCD (upper left), for excited quark at mass of 1.2 TeV (upper right) and for observed data (lower middle). The region between two solid lines shows $|\Delta\eta| < 1.3$ kinematic cut.

The signal acceptance for *qq*, *qg* and *gg* resonances are shown in Fig.6.8. The signal acceptances of *qq* and *qg* resonances are around 60%,which is reasonable. Fig. 6.9 shows $\eta_1 - \eta_2$ distribution of two leading jets for PTYHIA QCD MC sample (upper left), excited quark MC (upper right) sample at mass of 1.2 TeV and the data (lower middle) assuming 2.875 pb^{-1} integrated luminosity. The region between black solid lines is the selected kinematic region requiring $|\Delta\eta| < 1.3$ cut. Fig.6.10 shows $Signal/\sqrt{Background}$ ratio for each $|\eta|$ and $|\Delta\eta|$ cuts of excited quark at a mass of 1 TeV, 2 TeV and 3 TeV. Signal defined as the excited quark cross section at resonance mass, M_{Res}. The background defined as the LO QCD cross section for $0.9 \cdot M_{Res} < M_{jj} < 1.1 \cdot M_{Res}$. The $|\Delta\eta| < 1.3$ is optimal for isotropic decay like excited quark.

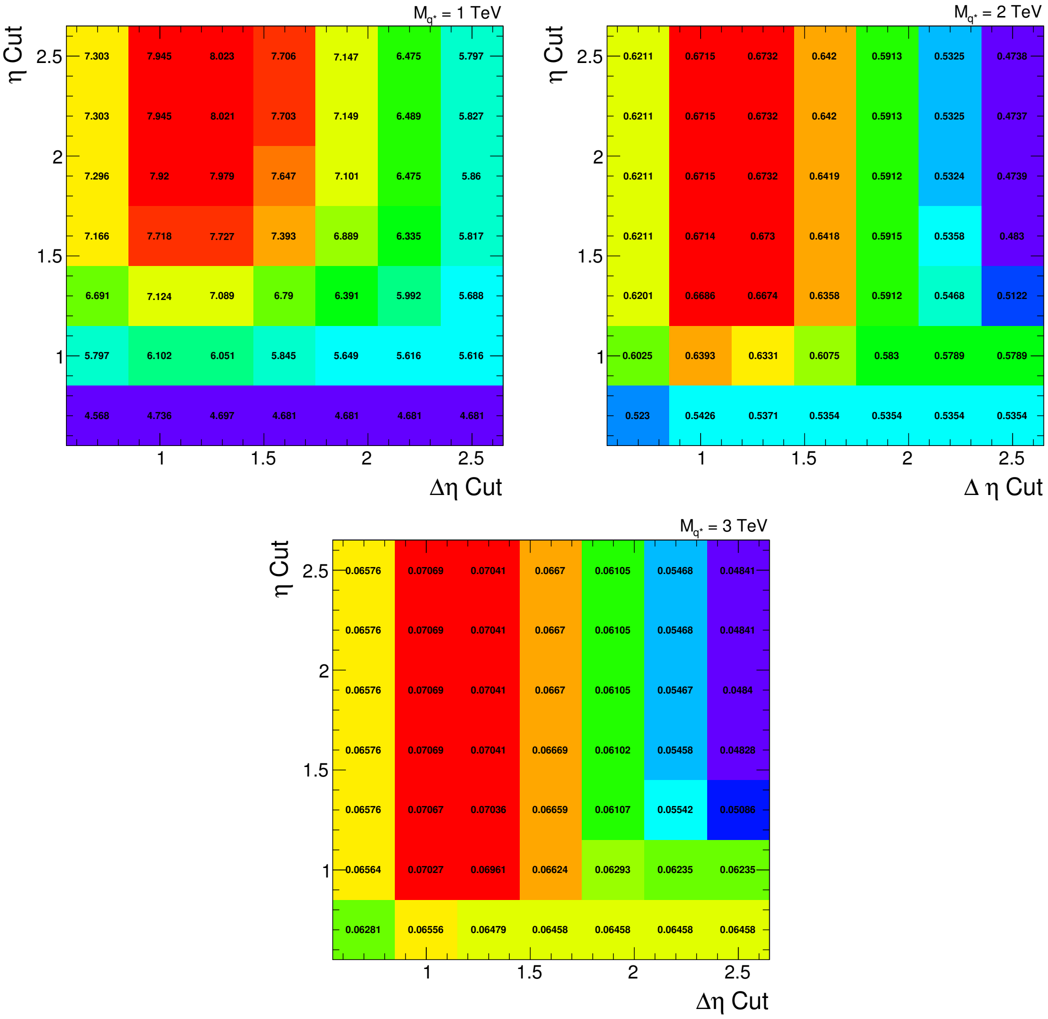

Figure 6.10. $Signal/\sqrt{Background}$ ratio of each $|\eta|$ and $|\Delta\eta|$ cuts for excited quark at masses of 1, 2 and 3 TeV.

6.3 Largest Fluctuation and Significance

The largest upward fluctuation in the dijet mass spectrum was investigated by searching for dijet resonance signal. Two simple statistical hypothesis are considered. Null-hypothesis, H_0, corresponding to only background is taken from smooth fit in Fig.5.13. Signal-hypothesis, H_s, is taken from $Background + Signal$ fit. The significance estimation from likehood-ratio is given by (Cousin, 2006)

$$S_L = \sqrt{2\ln(\frac{L_{s+b}}{L_b})} \tag{6.7}$$

where L_{s+b} is the maximum likelihood value from $Background + Signal$ fit and L_b is the maximum likelihood value from only background fit. S_L^2 is followed a χ^2 distribution with in the number of free parameter between the $Background + Signal$ fit (χ_s^2) and only background fit (χ_0^2). Thus the significance estimation can be defined as following:

$$S_L = \sqrt{-\Delta\chi^2} = \sqrt{\chi_0^2 - \chi_s^2} \tag{6.8}$$

The local significance value was calculated for resonances of excited quark with mass from 500 GeV to 2000 GeV in 1 GeV steps. The largest upward fluctuation in dijet mass distribution was found at 622 GeV with 1.86σ local significance ($\sqrt{32.33 - 28.88} = \sqrt{3.45} = 1.86$).

Fig.6.11 shows fractional difference between dijet mass distribution and $Background + Signal$ fit for resonance of excited quark at 622 GeV. The red line in Fig.6.11 is the estimated excited quark signal with mass of 622 GeV. The distribution of local significance values is shown in Fig. 6.12.

There is no evidence of dijet resonances in the dijet mass spectrum. So, 95% confidence-level upper limits on cross section are set and excluded mass limits for each dijet resonance model are calculated as will be discussed in the next section.

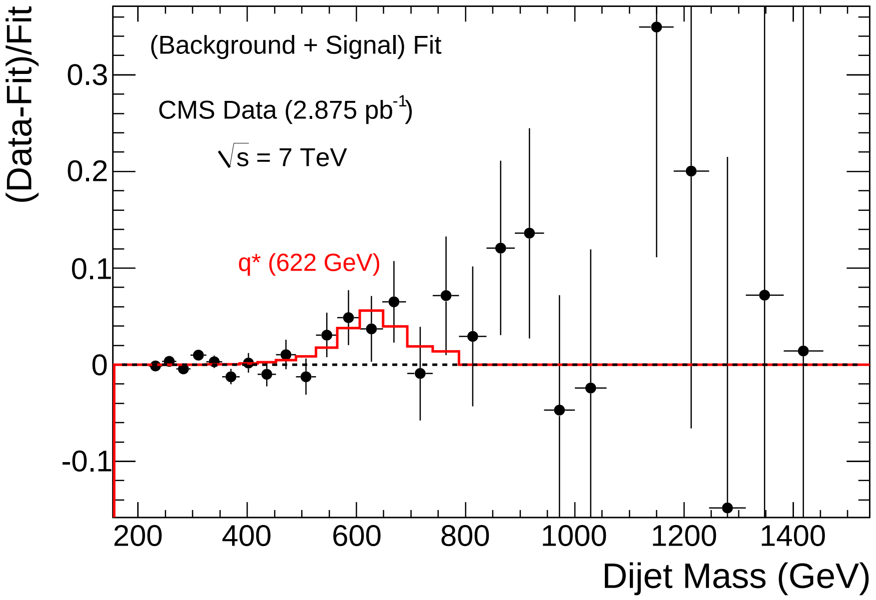

Figure 6.11. The fractional difference signal-hypothesis fit and dijet mass distribution with estimated excited quark signal (red solid line).

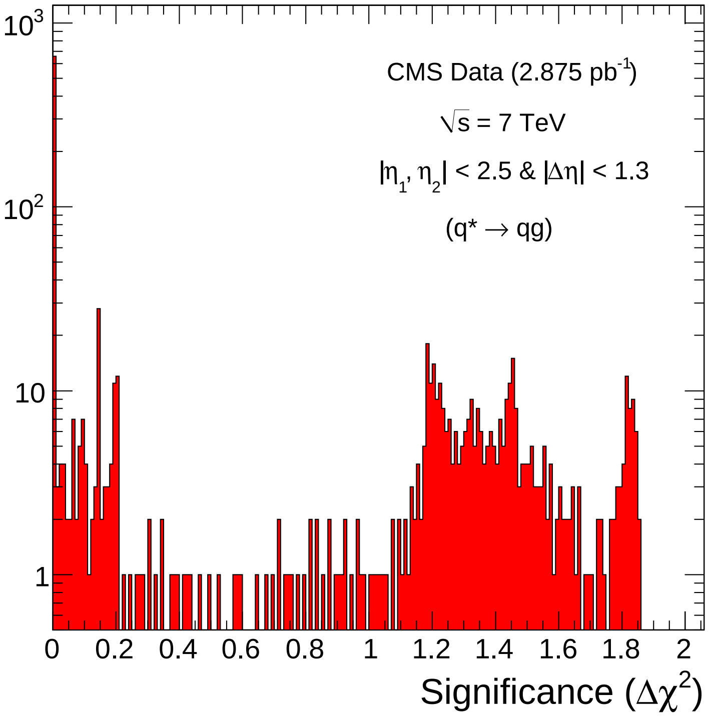

Figure 6.12. The distribution of local significance values.

6.4 Setting Cross Section Upper Limits

In the absence of any observed significant evidence of dijet resonances, a Bayesian formalism with flat prior for the cross section was used to set 95% confidence-level (CL) upper limits (Heinrich, 2004). The binned likelihood function as a function of a signal normalization constant, α, for each bin (i) of the distribution is written as:

$$L(n|\mu) = \prod_i \frac{\mu_i^{n_i} e^{-\mu_i}}{n_i!} \tag{6.9}$$

where

$$\mu_i = \alpha N_i(S) + N_i(B). \tag{6.10}$$

n_i is the measured number of events in the $i-th$ dijet mass bin, $N_i(S)$ is the number of events from signal in the $i-th$ dijet mass bin, α multiplies the signal and $N_i(B)$ is the number of expected events from background in the $i-th$ dijet mass bin. It is considered that QCD background is fixed to the best $Signal + QCD$ fit to data points and it gives the expected number of background event in the $i-th$ dijet mass bin, $N_i(B)$. This simple and conservative method takes any upward fluctuation observed in the data consistent with a resonance as an actual resonance, and finds the background beneath it from the simultaneous fit to the background parametrization plus resonance signal. It ensures that the background, $N_i(B)$, wouldn't be biased by the existence of any signal. The number of signal in the $i-th$ dijet mass bin, $N_i(S)$,comes from the interpolation technique on a signal for a qq, qg or gg resonance with arbitrary cross section. The signal range is chosen from $0.3 \cdot M_{Res}$ to $1.3 \cdot M_{Res}$ since low mass tail is effectively lost in QCD background and resonance line shapes beyond $1.3 \cdot M_{Res}$ are highly model dependent for narrow resonances and not trusted. It contains nearly all the resonance line shapes. The lowest dijet mass in the signal ranges was set as 220 GeV, since dijet mass spectrum was started from 220 GeV. The likelihood function is multiplied by a flat prior in cross section, $P(\sigma)$, and normalized to give a posterior probability density in the cross section;

$$P_{post}(\sigma) = \frac{L(n|\mu)P(\sigma)}{\int_0^\infty L(n|\mu)P(\sigma)d\sigma}. \tag{6.11}$$

The 95% confidence level upper limit on the cross section with only statistical uncertainties, $\sigma_{95\%}$, is calculated from the posterior probability density as;

$$\int_0^{\sigma_{95\%}} P_{post}(\sigma)d\sigma = 0.95. \tag{6.12}$$

The two examples of posterior probability density are shown in Fig.6.13 for *qg* resonances at mass of 0.6 TeV and 1.5 TeV. For the case of 0.6 TeV resonance, the upward fluctuation is particularly strong, roughly at the level of 2σ, and produces a peak in the posterior probability density. It also increases the upper limit significantly. For the case of 1.5 TeV resonance, the data in that region is either below or at the background fit on the average. Thus, the peak is at zero signal cross section in the posterior probability density for 1.5 TeV resonances.

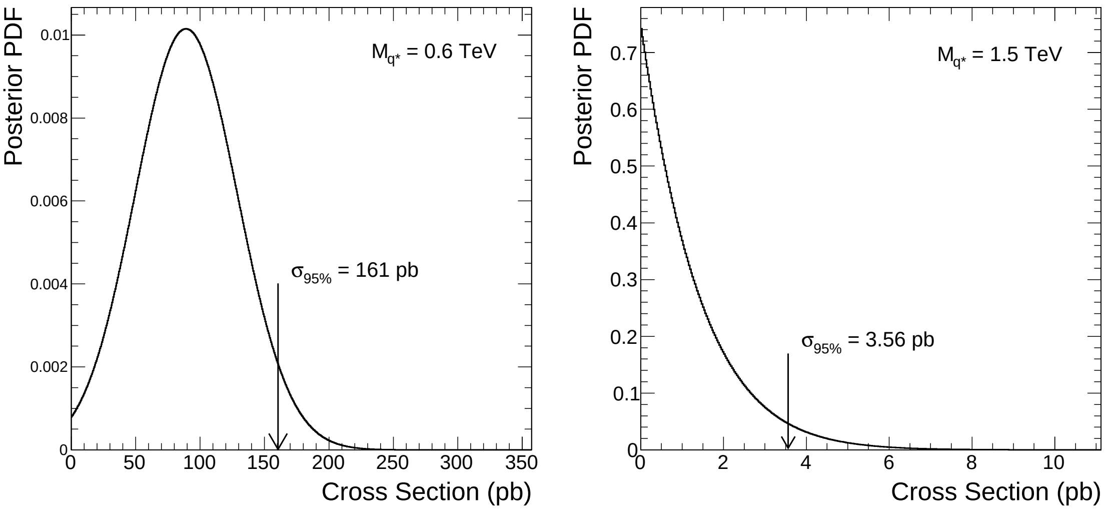

Figure 6.13. Posterior probability density with 95% C.L. cross section upper limit at mass of 0.6 TeV (left) and 1.5 TeV (right) for *qg* resonances with statistical error only.

The 95% CL upper limits on cross section were calculated for resonances with mass from 0.5 TeV to 2.6 TeV on 0.1 TeV steps. Fig.6.14 shows the 95% CL upper limit on cross section including only statistical error for *qq*, *qg* and *gg* resonances separately, which are compared to the cross section for various resonance models. The upper limits have small wiggles due to the upward and downward fluctuation in the data. The measured 95% CL upper limit values are listed in Table 6.1.

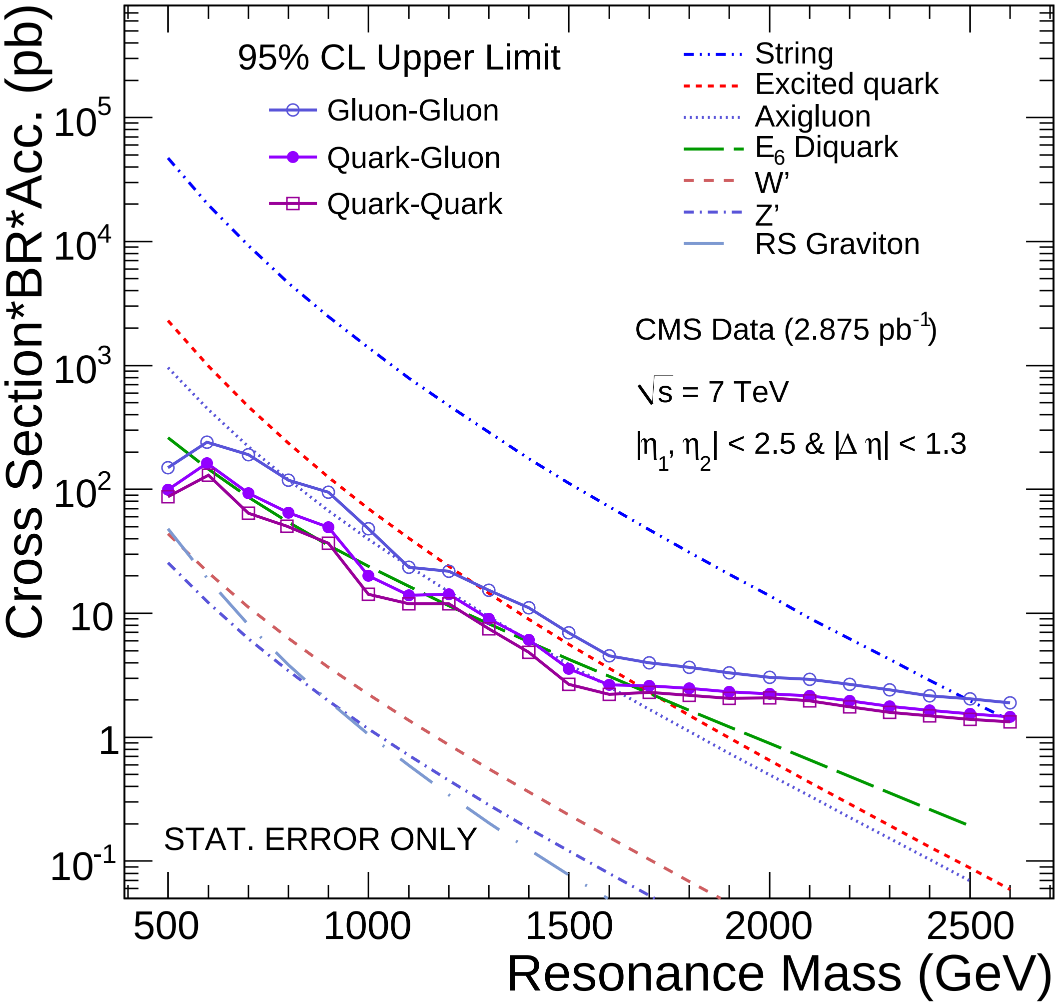

Figure 6.14. The 95% CL upper limit on cross section times branching ratio and acceptance as a function of resonance mass for *qq*, *qg* and *gg* resonances, is compared to the model cross section with statistical error only.

Mass	95% C.L. $\sigma \cdot B$ (pb) Stat. Err. Only		
(TeV)	quark-quark	quark-gluon	gluon-gluon
0.5	87.5	99.0	149
0.6	129	161	236
0.7	64.0	93.2	192
0.8	49.6	64.7	119
0.9	36.8	49.4	95.1
1.0	14.2	20.1	48.0
1.1	11.9	14.0	23.5
1.2	12.0	14.2	21.9
1.3	7.49	9.04	15.4
1.4	4.86	6.14	11.1
1.5	2.68	3.56	6.96
1.6	2.22	2.65	4.54
1.7	2.30	2.61	4.00
1.8	2.18	2.47	3.68
1.9	2.07	2.32	3.31
2.0	2.09	2.25	3.06
2.1	1.96	2.15	2.93
2.2	1.75	1.96	2.66
2.3	1.58	1.77	2.40
2.4	1.49	1.64	2.16
2.5	1.39	1.55	2.05
2.6	1.33	1.46	1.89

Table 6.1. The 95% C.L. upper limit on cross section times branching ratio and acceptance as a function of resonance mass for quark-quark, quark-gluon and gluon-gluon resonances with statistical errors only.

6.5 Systematic Uncertainties on the Search

The source of systematic uncertainties are considered as following:

- Jet Energy Scale (JES)
- Jet Energy Resolution (JER)
- Choice of Background Parametrization
- Luminosity

The procedure to evaluate the first three sources is to use a smooth fit to the QCD background as a data sample and find the cross section upper limits before and after the systematic shift. The reason of using a smooth fit to the QCD background instead of actual data is to eliminate the wiggles in the upper limit curves.

6.5.1 Jet Energy Scale

The uncertainty on JES is basically the relative error between the jets in the signal simulation and where the signal would emerge in the real data. If the simulation produces jets with too high a response, the true position of the expected peak of a given resonance mass would appear at lower mass than predicted by simulation in the actual measured dijet mass spectrum. It is assumed that the uncertainty on JES is roughly $\pm 10\%$ and the resonance signals shift by 10% in dijet mass at startup. Shifting the resonance signal 10% lower in dijet mass gives more QCD background and finding the resonance signal becomes harder. The corresponding limits will be worse.

The left plot in Fig.6.15 shows smooth cross section limit without systematics and with systematic on JES uncertainty for qg resonance. To get smooth cross section limit curve, expected events from background, $N_i(B)$, which is smooth and comes from the fit function are considered as the measured number of events, n_i, in the $i-th$ dijet mass bin. Fractional change between smooth limits with and without JES uncertainty are illustrated separately for qq, qg and gg resonances in the right plot of Fig.6.15. The systematic uncertainty decreases with resonance mass because the limits are set at the edge of the region with real data and the uncertainty is very sensitive to whether any data events are expected from background. If there is no background, there is no change with JES uncertainty. When more data are involved, the systematic uncertainty at high resonance mass should increase with integrated luminosity. The uncertainty on JES varies roughly from 40% to 15% depending on resonance mass and type.

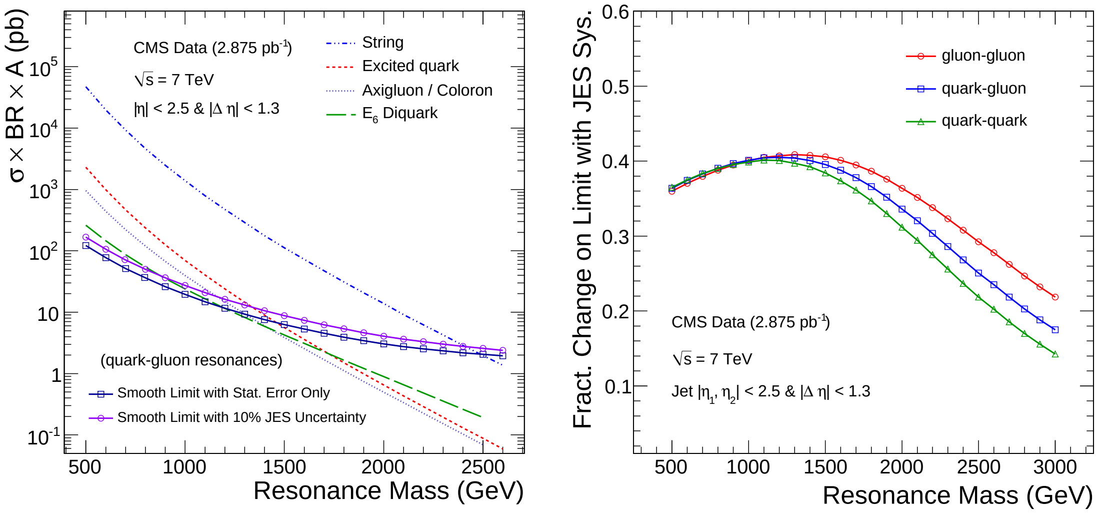

Figure 6.15. Comparison of smoothed cross section limit without systematics and with systematic on JES uncertainty (left). Fractional change on limit with JES systematic uncertainty (right).

6.5.2 Jet Energy Resolution

It is assumed that the uncertainty on JER is roughly ±10% and the signal is being smeared with a Gaussian that increases the core resolution by 10%. On the other word, the signal becomes 10% wider. The sigma of a Gaussian is chosen in terms of core resolution at particular resonance mass as follow:

$$\sigma_{Gaus} = \sqrt{(1.1^2 - 1)} \cdot \sigma_{Res}. \tag{6.13}$$

Dijet mass core resolution of the resonance signal as a function of resonance mass is illustrated in Fig.6.4. The σ_{Res} are obtained from the Equation 6.1 for each resonance masses. Fig.6.16 shows the resonance shape comparison after convolution at 1.2 TeV for each type of parton pairs. The fractional change on limit with JER systematic is illustrated in Fig.6.17. Since width of resonance shape is the narrowest for *qq* resonances, the fractional change on limit is the lowest for *qq* resonance as it is expected. The uncertainty on JER varies roughly from 22% to 8% depending on resonance mass and type.

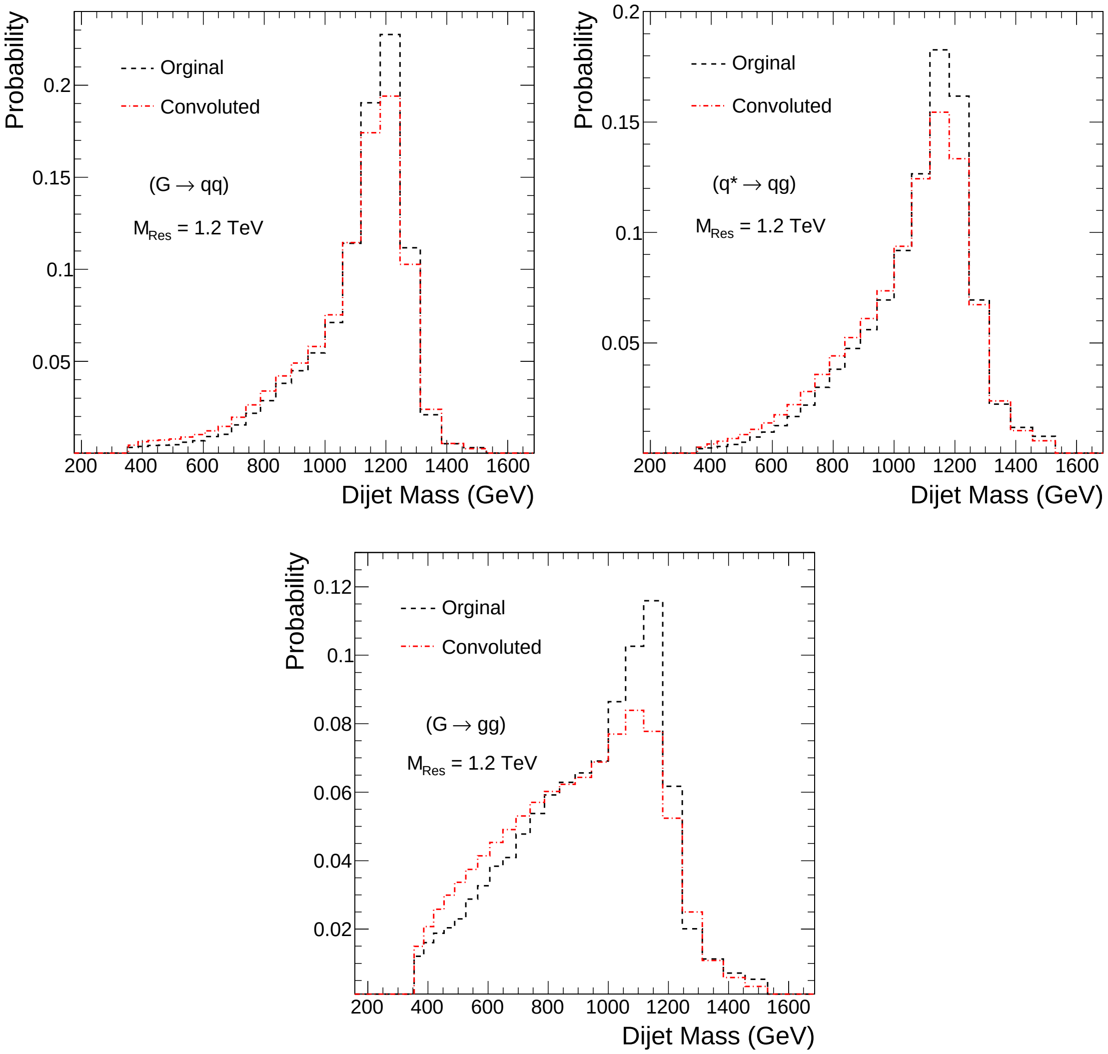

Figure 6.16. The comparison of resonance shape after convolution at 1.2 TeV for *qq* (upper left), *qg* (upper right) and *gg* (bottom) resonances.

6.5.3 Choice of Background Parametrization

The other functional forms to parametrize the QCD background were discussed in Chapter 5.3.1. The effect on limit has been determined with changing from default fit to

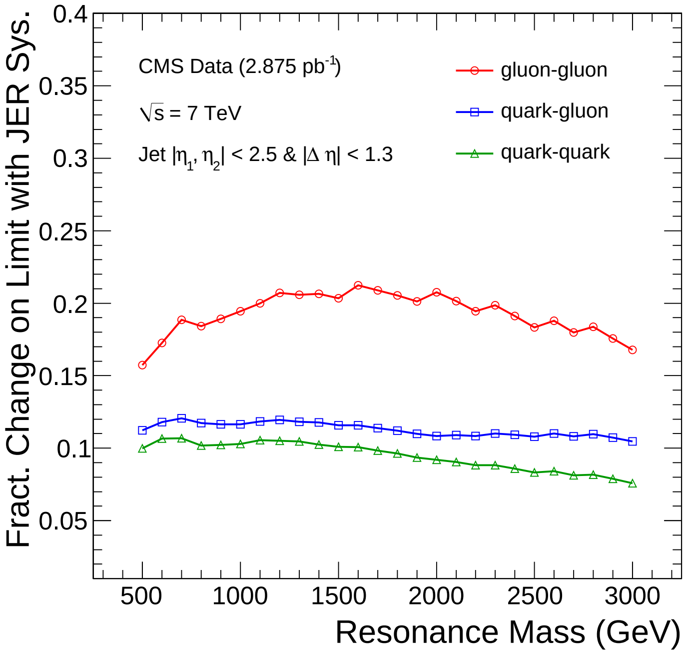

Figure 6.17. The fractional change on limit with JER systematic uncertainty.

Alternate Fit A with 4 parameters which is given by

$$\frac{d\sigma}{dm} = P_0 \cdot \frac{\left(1 - X + P_3 \cdot X^2\right)^{P_1}}{m^{P_2}}. \tag{6.14}$$

where $X = m/\sqrt{s}$. The fractional change on limit with background parameterization is shown in Fig.6.18. Fractional change at low resonance mass is small because there are a lot of events to constrain the background at low mass and gives a good fit. As the resonance mass increases, the fit is more poorly constrained by fewer events and systematic increases. The systematic decreases again at the highest resonance masses since there is no background. The uncertainty on background parameterization varies roughly from 19% to 8% depending on resonance mass and type.

6.5.4 Total Uncertainty

The change of 1σ for each systematic uncertainty in signal are added in quadrature to find total systematics as following:

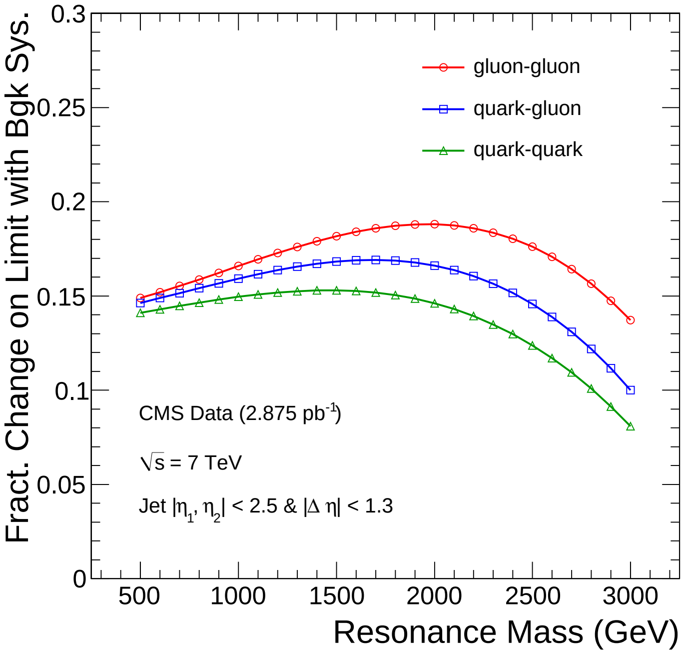

Figure 6.18. The fractional change on limit with background parametrization systematic uncertainty.

$$\sigma_{Total} = \sqrt{\sigma^2_{JES} + \sigma^2_{JER} + \sigma^2_{Background} + \sigma^2_{Luminosity}}. \tag{6.15}$$

The uncertainty on luminosity is assumed as 11%. The individual and total systematic uncertainties as a function of resonance mass are shown in Fig.6.19. The dominant source of systematic uncertainty is jet energy scale (JES). Absolute uncertainty on cross section for each mass is calculated as total fractional systematic uncertainty multiplied by upper cross section limit. The total systematic uncertainty of each type of parton pairs are also shown in Fig.6.19.

6.6 Incorporating Systematics in the Limit

The posterior probability density are convoluted with a Gaussian for each resonance mass (Demortier, 2005). The equation of convolution is

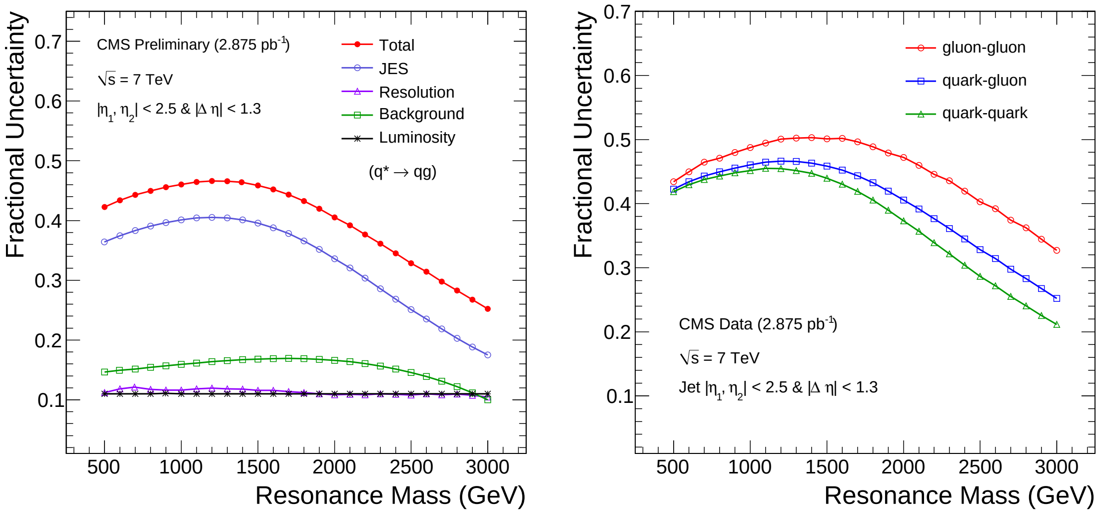

Figure 6.19. Individual fractional systematic uncertainty with the total systematic uncertainty for *qg* resonances (left). Total fractional uncertainty for *qq*, *qg* and *gg* resonances (right).

$$P_{post}(\sigma) = \int_0^{\infty} P_{post}(\sigma')G(\sigma,\sigma')d\sigma', \tag{6.16}$$

where

$$G(\sigma,\sigma') = \frac{1}{\sqrt{2\pi\sigma_{uncer}}} e^{\frac{-(\sigma'-\sigma)^2}{2\sigma_{uncer}}}, \tag{6.17}$$

and $P_{post}(\sigma')$ is the posterior density at signal cross section σ'. The width of the Gaussian, σ_{uncer} is the absolute uncertainty on cross section for each resonance mass, which is calculated as

$$\sigma_{uncer} = \sigma_{Total} \cdot \sigma_{95\%}. \tag{6.18}$$

The convoluted value $P_{post}(\sigma)$ is normalized to unit area over the range $0 < \sigma <$ inf. Fig. 6.20 shows the posterior probability densities before convolution and after convolution for *qg* resonances at mass of 0.6 TeV and 1.5 TeV. The posterior probability density including systematic uncertainties is broader and gives higher upper limit. The posterior probability densities for each resonance mass are shown in Appendix D.

The 95% CL cross section upper limit for *qg* resonances with statistical uncertainties only and including all systematic uncertainties are shown ih Fig.6.21. The effects of systematics on the cross section upper limit as a function of resonance mass is also illustrated in Fig.6.21 for each types of parton pairs. The cross section upper limits vary roughly from 50% to 16% depending on resonance mass and types and the change in the mass limits is only about 0.1 TeV for both excited quark and string resonances when systematic uncertainties are included.

The 95% CL upper limit on cross section including systematic uncertainties for *qq*, *qg* and *gg* resonances are shown in Fig.6.22 separately. The measured final 95% CL upper limit on cross section values including systematics are listed in Table 6.2.

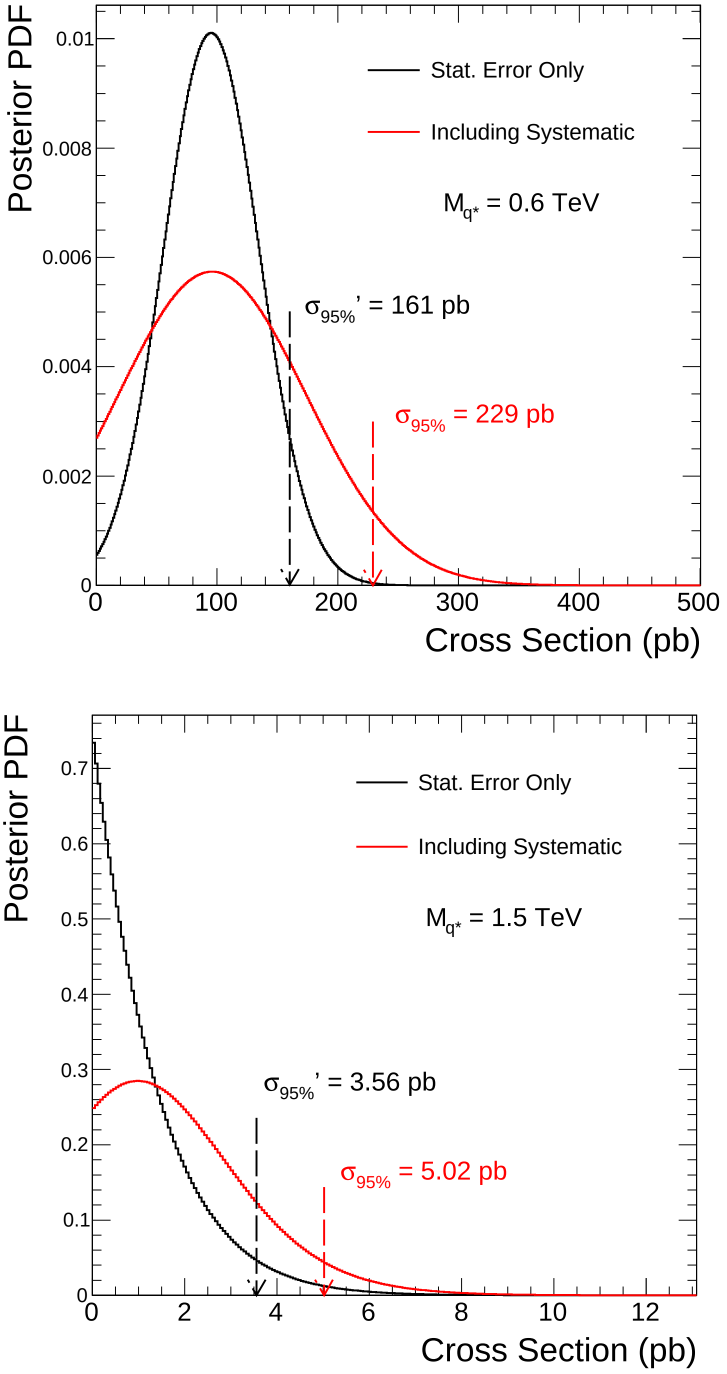

Figure 6.20. The posterior probability densities with 95% CL cross section limit at resonance masses of 0.6 TeV (top) and 1.5 TeV (bottom) including systematics.

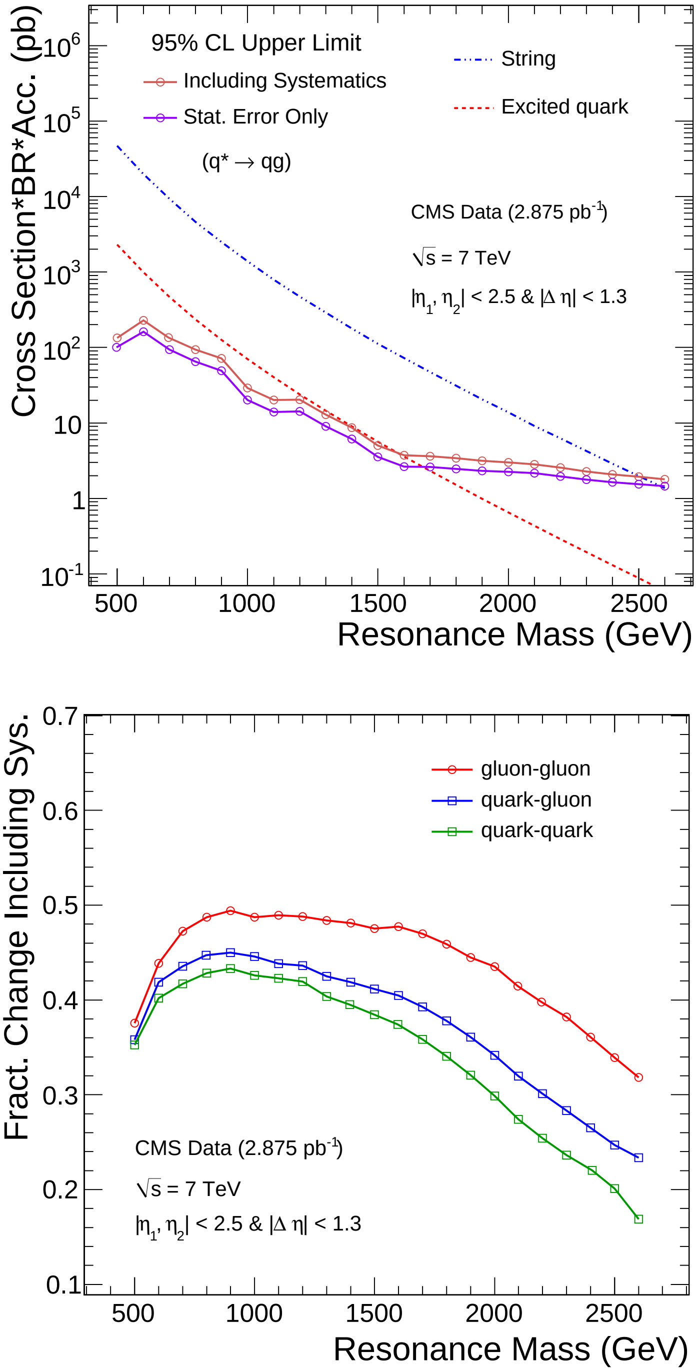

Figure 6.21. Cross section limits for qg resonance with only statistical error and including systematic uncertainties (top). The fractional change on the limits for each type of parton pairs including systematic uncertainties (bottom).

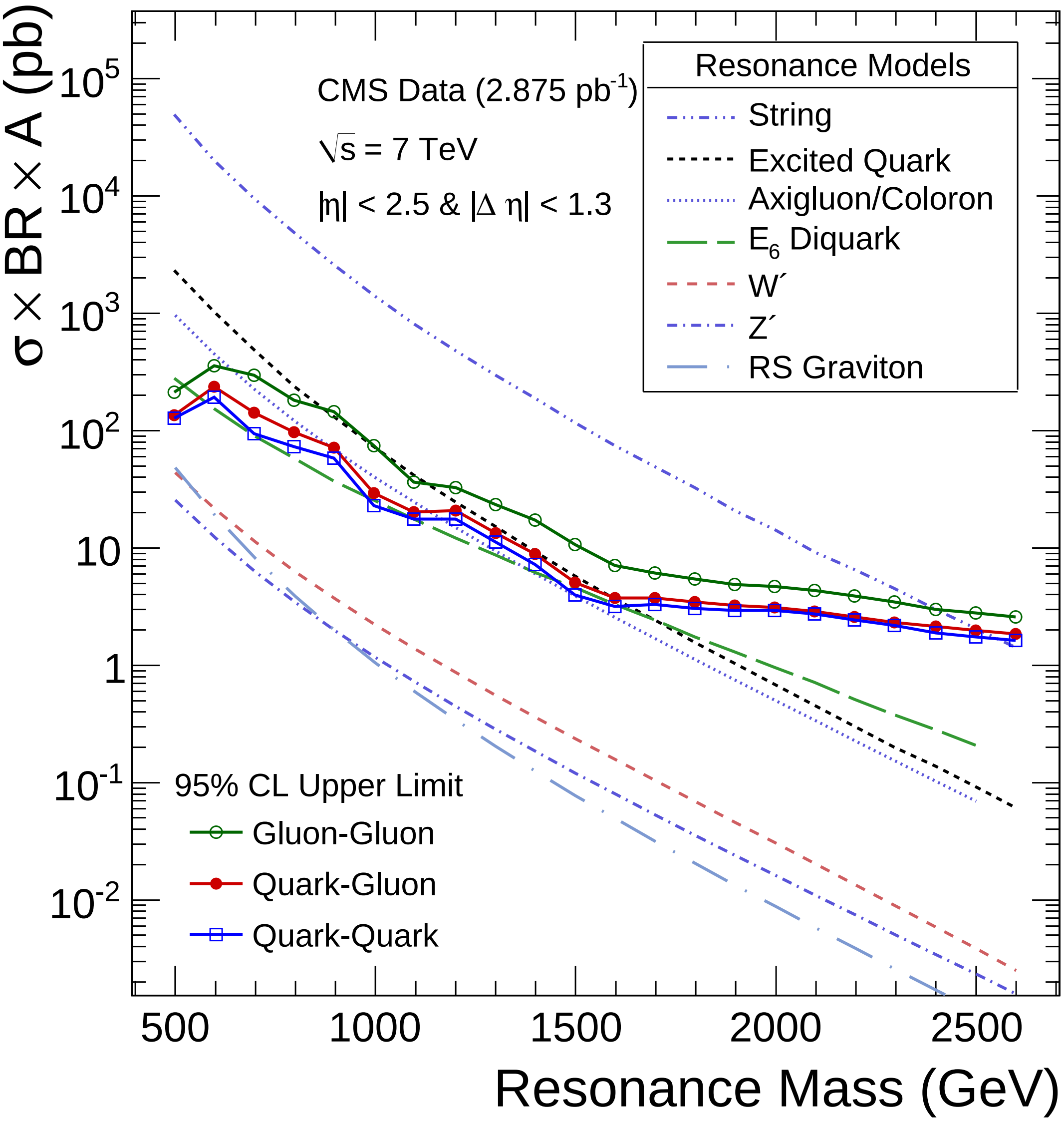

Figure 6.22. The 95% CL upper limit on cross section times branching ratio and acceptance including systematic for *qq*, *qg* and *gg* resonances, compared to the model cross section.

Mass	95% C.L. $\sigma \cdot B$ (pb)		
(TeV)	quark-quark	quark-gluon	gluon-gluon
0.5	118	134	206
0.6	182	229	339
0.7	90.7	134	281
0.8	70.8	93.5	177
0.9	52.7	71.6	142
1.0	20.3	29.0	71.4
1.1	17.0	20.1	35.1
1.2	17.0	20.4	32.5
1.3	10.5	12.9	22.8
1.4	6.77	8.71	16.4
1.5	3.71	5.02	10.3
1.6	3.05	3.72	6.71
1.7	3.13	3.64	5.88
1.8	2.92	3.41	5.37
1.9	2.73	3.15	4.78
2.0	2.71	3.02	4.39
2.1	2.50	2.84	4.15
2.2	2.20	2.55	3.69
2.3	1.96	2.28	3.32
2.4	1.79	2.08	2.94
2.5	1.67	1.93	2.74
2.6	1.55	1.80	2.50

Table 6.2. The 95% C.L. upper limit on cross section times branching ratio and acceptance for quark-quark, quark-gluon, and gluon-gluon resonances, including systematic uncertainties.

6.7 Expected Limits

It was assumed that smooth background samples without fluctuations from a smooth fit is dijet mass spectrum and use the number of events expected in each bin from this smooth fit to calculate 95% CL expected upper limit on cross section.

The expected limits on the cross section are compared to the observed limits in Fig.6.23 for *qq* and *qg* resonances. The downward fluctuations in data around 1.2 TeV allow to set 250 GeV better observed mass limit than the expected mass limit for excited quark model.

6.8 Results on Dijet Resonances

The ratio between the model cross section and 95% CL upper limit on cross section are shown in Fig.6.24. The cross section of excited quark and string resonances models are divided by upper limit on cross section of *qg* resonances since these both models decay into a quark and a gluon predominantly. The cross section of axigluon, coloron and E_6 diquark models are divided by upper limit on cross section of *qq* resonances due to the same reason.

The 95% CL excluded mass regions of the considered dijet resonance models are listed in Table 6.3. In terms of the observed data, the CMS should be sensitive to the string resonances up to 2.50 TeV, to excited quark up to 1.58 TeV.

Axigluons, colorons and E_6 diquarks have specific mass intervals due to the wiggles in the upper limit curve of *qq* resonances which are caused by upward and downward fluctuations in the dijet mass spectra. For axigluons, colorons and E_6 diquarks, 95% CL excluded mass regions can be seen in Table 6.3.

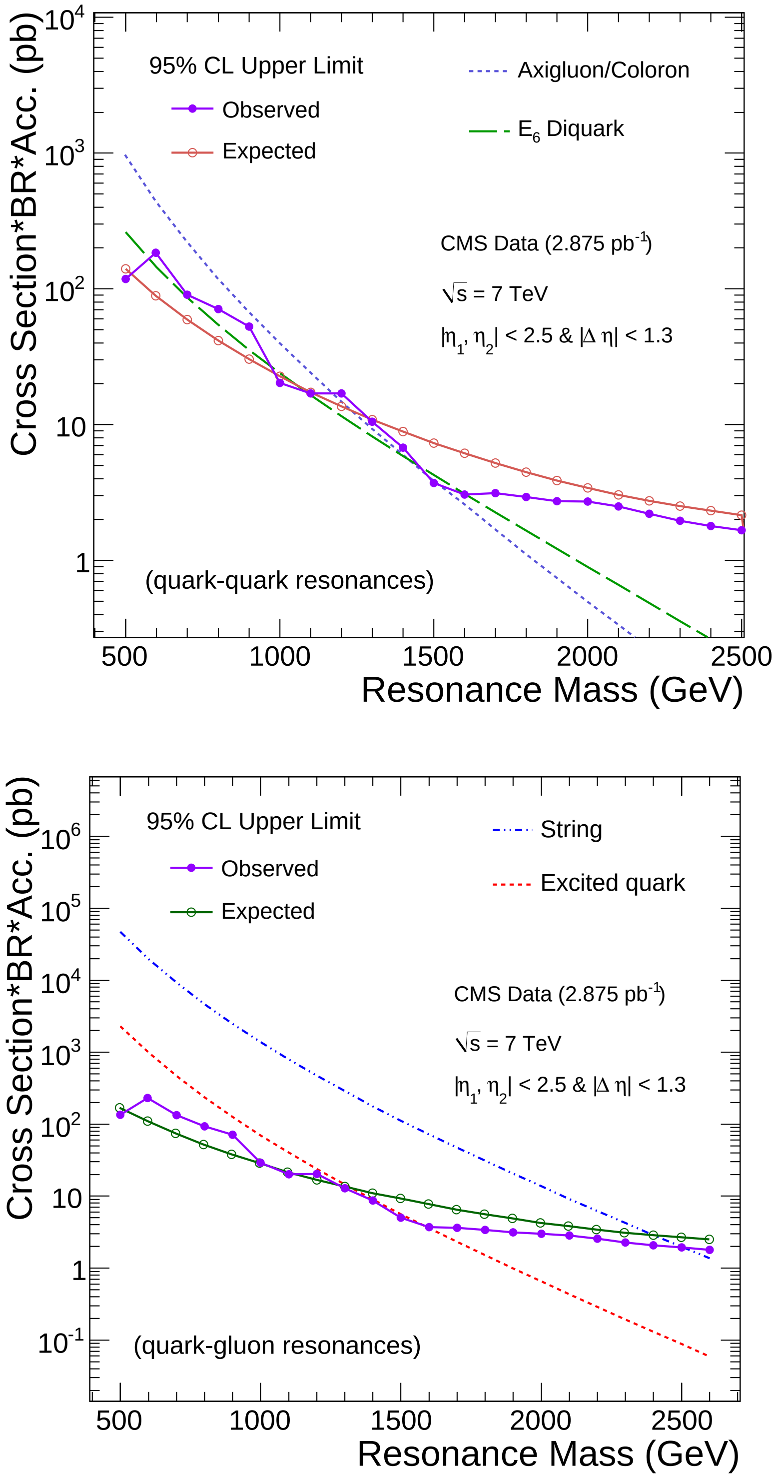

Figure 6.23. The observed 95% CL upper limit on cross section for *qq* resonances (top) and *qg* resonances (bottom), compared to expected 95% CL upper limit on cross section.

Model	Observed Mass Limit (Tev)		Expected Mass Limit (TeV)
	Including Systematics	Stat. Error Only	Including Systematics
String Resonance	$0.50 < M(S) < 2.50$	$0.50 < M(S) < 2.58$	$0.50 < M(S) < 2.40$
Excited Quark	$0.50 < M(q*) < 1.58$	$0.50 < M(q*) < 1.68$	$0.50 < M(q*) < 1.32$
Axigluon/Coloron	$0.50 < M(A) < 1.17$ & $1.47 < M(A) < 1.52$	$0.50 < M(A) < 1.63$	$0.50 < M(A) < 1.23$
E_6 Diquark	$0.50 < M(D) < 0.58$ & $0.97 < M(D) < 1.08$ & $1.45 < M(D) < 1.60$	$0.50 < M(D) < 0.87$ & $0.90 < M(D) < 1.19$ & $1.23 < M(D) < 1.70$	$0.50 < M(D) < 1.05$

Table 6.3. The excluded mass limits at 95% C.L. for the considered dijet resonance models.

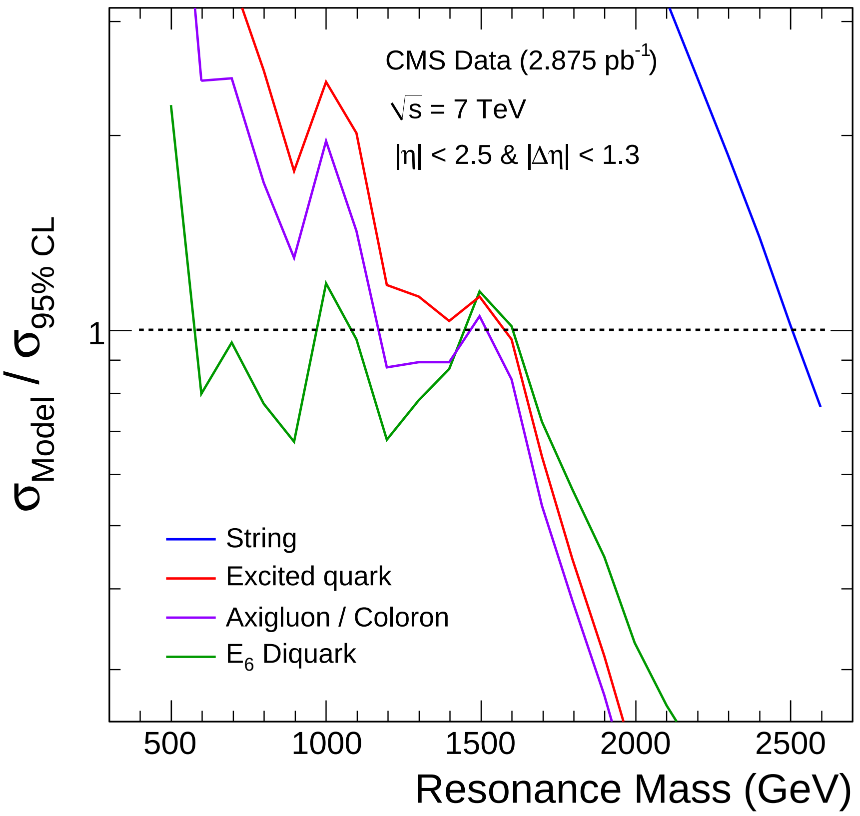

Figure 6.24. The model cross section is divided by 95% CL upper limit on cross section.

7. CONCLUSIONS

In summary, this thesis consists of two parts; the measurement of dijet mass pectrum and the search for new particles. Basically, this thesis is a bump hunting analysis. The experimental technique of this analysis can be summarized as follows:

1. Measure the dijet mass spectrum.
2. Compare the measured dijet mass spectrum to PYTHIA QCD Monte Carlo prediction.
3. Fit the measured dijet mass spectrum with a smooth function and search for resonance signals.
4. If there is no evidence for dijet resonances, calculate model independent cross section upper limit and compare with the cross section prediction of any model.
5. Set the excluded mass limits for the dijet resonance models.

Since the dijet resonance signals are searched in the dijet mass spectrum as a bump, we have measured the dijet mass spectrum as a first step. We have used 2.875 pb^{-1} of CMS data to measure the dijet mass spectrum with the following eta cuts on the two leading jets: $|\Delta\eta| < 1.3$ and $|\eta| < 2.5$. The event with the largest observed dijet mass is at 2.05 TeV. The measured dijet mass spectrum is in good agreement with a QCD prediction from PYTHIA and the full simulation of the CMS detector.

We have performed direct searches for high-mass dijet resonances in the dijet mass distribution. We have fit the dijet mass spectrum to a function containing 4 parameters. The dijet mass data is well fit by a simple parameterization. The largest upward fluctuation in dijet mass distribution has been found at 622 GeV with 1.86σ local significance and there is no significant evidence for new particle production in the data.

95% confidence level upper limits on the cross section for a dijet resonance have been set, applicable to any narrow resonance producing the following specific pairs of partons: qq, qg, and gg, which are model independent and can be applied to any model. The limits are compared with calculations of the cross section times branching ratio for dijets with the eta cuts from seven different models: String, Excited Quarks, Axigluons, Colorons, E_6 diquarks, W', Z', and RS Gravitons. The calculations use CTEQ6L1 where the lowest order strong coupling constant α_s is used. We can exclude mass points for the models with predicted cross sections greater than our 95% CL upper limit on the cross section for the appropriate parton pairs.

For string resonances we use our limits on qg resonances to exclude at 95% C.L. the mass range $0.50 < M(S) < 2.50$ TeV. For comparison, the cross section upper limits on dijet resonances from CDF imply a limit on string resonances of about 1.4 TeV. For excited quarks we use our limits on qg resonances to exclude the mass range $0.50 < M(q^*) < 1.58$ TeV, extending the previous ATLAS exclusion of $0.40 < M(q^*) < 1.26$ TeV (Aad, 2010). For axigluons or colorons we use our limits on qq resonances to exclude the mass intervals $0.50 < M(A) < 1.17$ TeV, and $1.47 < M(A) < 1.52$ TeV extending the previous CDF exclusion of $0.12 < M(A) < 1.25$ TeV (Aaltonen, 2009). For E_6 diquarks we use our limits on qq resonances to exclude the mass range $0.50 < M(D) < 0.58$ TeV, and $0.97 < M(D) < 1.08$ TeV, and $1.45 < M(D) < 1.60$ TeV, extending the previous CDF exclusion of $0.29 < M(D) < 0.63$ TeV (Aaltonen, 2009).

This study has been published in Physical Review Letters (Khachatryan, 2010) and it is the first CMS search paper and the first CMS jet paper. It has also been featured in ”Highlighted Articles” in this issue of the Physical Review Letters.

REFERENCES

AAD,G., et al., 2010, ”Search for New Particles in Two-Jet Final States in 7 TeV Proton-Proton Collisions with the ATLAS Detector at the LHC”, ATLAS Collaboration, Phys.Rev.Lett. 105, 161801 (2010)

AALTONEN,T., et al., 2009, ”Search for new particles decaying into dijets in proton-antiproton collisions at $\sqrt{(s)} = 1.96$ TeV”, CDF Collaboration, Phys.Rev.D79 112002.

ABE,F., et al., 1995, ”Search for new particles decaying to dijets in $p\bar{p}$ collisions at $\sqrt{s} =$ 1.8 TeV”, CDF Collaboration, Phys.Rev.Lett.74 3538-3543.

__________, 1997, ”Search for new particles decaying to dijets at CDF”, CDF Collaboration, Phys.Rev.D55 5263-5268.

ANCHORDOQUI,L.A., et al., 2008, ”Dijet signals for low mass strings at the LHC”, Phys.Rev.Lett. 101 241803, arXiv:0808.0497.

AZZURRI,P., et al., 2010, ”Commissioning of TrackJets in pp Collisions at 7 TeV”, The CMS Collaboration CMS-PAS-JME-10-006.

BAGGER,J., SCHMIDT,C. and KING,S., 1988, ”Axigluon Production in Hadron Collisions”, Phys. Rev.D37 1188.

BAUR,U., HINCHLIFFE,I. and ZEPPENFELD,D., 1987, ”Excited Quark Production At Hadron Colliders”, Int. J. Mod. Phys.A2 1285.

BAYATIAN, G., et al., 2000a, CMS TriDAS Project Technical Design Report Volume 1:

__________, 2006, CMS Physics Tehcnical Design Report, Volume I: Detector Performance and Software, 2006-001, CMS TDR 8.1, CERN/LHCC.

__________, 2000b, CMS TriDAS Project Technical Design Report Volume 2: The Data Acquisition System, Technical Report 2002-26, CERN/LHCC.

__________, 1997a, CMS Electromagnetic Calorimeter Project Technical Design Report, Technical Report 97-33, CERN/LHCC.

__________, 1997b, CMS Hadronic Calorimeter Project Technical Design Report, Technical Report 97-31, CERN/LHCC.

__________, 1997c, CMS Magnet Technical Design Report, Technical Report 97-10, CERN/LHCC.

__________, 2005, CMS Computing Technical Design Report 2005-023 CERN/LHCC.

BERNET,C., et al., 2009, ”Particle Flow Reconstruction of Jets, Taus, and MET”, The CMS Collaboration CMS-PAS-PFT-09-001.

BRUENING, O., 2004, LHC Design Report, Technical Report, CERN-2004-003.

CACCIARI,M., SALAM,G.P. and SOYEZ.,G., 2008, ”The Anti-kt Jet Clustering Algorithm”, JHEP0804:063,2008 and arXiv-hep-ph:0802.1189v2

CHATRCHYAN, S., et al., 2008, ”The CMS experiment at the CERN LHC”, The CMS Collaboration JINST 3 S08004.

__________, 2010, ”Search for Dijet Resonances in 7 TeV pp Collisions at CMS”, The CMS Collaboration, Phys. Rev. Lett. 105, 211801(2010).

CHIVUKULA,R.S., et al., 1996, ”New Strong Interactons at the Tevatron ?”, Phys.Lett.B. 38 92-98.

COUSINS,R., MUMFORD,J. and VALUEV,V., 2006, ”Detection of Z' Gauge Bosons in the Dimuon Decay Mode in CMS”, CMS NOTE 2006/062.

DASU,S., 2002, ”CMS Trigger and Event Selection”, EPJ direct,10.1007/s1010502cs109.

DEMORTIER,L., 2005, ”A Convolution Method for Folding Systematic Uncertainties into Likelihood Functions”, CDF/MEMO/STATISTICS/PUBLIC/5305.

DRAGOIU,C., et al., 2010, ”Measurement of the Jet Energy Resolution in 7 TeV Collision Data with the Asymmetry Method”, CMS AN-2010/134.

EICHTEN,E., et al., 1984, ”Super Collider Physics”, Rev.Mod.Phys. 56 579-707.

ELLIS,R.K., et al., 1996, ”QCD and Collider Physics”, Cambridge University Press.

ELLIS,S.D., et al., 2007, ”Jets in Hadron-Hadron Collisions”, arXiv:hep-ph/0712.2447v1.

FLUGGE, G., 1994, Yellow Reports, CERN 94-04.

HAREL,A., et al., 2009, ”Calorimeter Jet Quality Criteria for the First CMS Collision Data”, The CMS Collaboration CMS-PAS-JME-09-008.

HARRIS,R.M., et al., 2007, ”Plans for Jet Energy Corrections at CMS”, The CMS Collaboration CMS-PAS-JME-07-002.

__________, 2008, ”Determination of the Relative Jet Energy Scale at CMS from Dijet Balance”, The CMS Collaboration CMS-PAS-JME-08-003.

HARRIS,R.M and OZTURK,S. et al, 2010, ”Search for Dijet Resonances in the Dijet Mass Distribution in pp Collisions at 7 TeV”, CMS-PAS-EXO-10-001.

HARRIS,R.M and OZTURK,S. et al, 2010, ”Update on Search for Dijet Resonances in the Dijet Mass Distribution in pp Collisions at 7 TeV”, CMS-PAS-EXO-10-010.

HEINRICH,J., et al., 2004, ”Interval estimation in the presence of nuisance parameters. 1. Bayesian approach”, arXiv:physics/0409129v1 [physics.data-an].

HEWETT,J.L. and RIZZO,T.G., 1989, ”Low-Energy Phenomenology of Superstring Inspired E(6) Models”, Phys.Rept.183 193.

IASHVILI,I., et al., 2010, ”Offset Energy Correction for Cone Jets”, CMS AN-2010/150.

JEONG,C., et al, 2009, ”Dijet Resonance Shapes for 10 TeV”, CMS AN-2009/145.

KATSILIERIS,G., KORAKIANITIS,O. and VLASSOPULOS,S.D.P., 1992, ”Two-jet rates affected by exotic particles at hadron colliders”, Physics Letters B, Volume 288, Issues 1-2, Pages 221-226.

KOUSOURIS,K., et al., 2010, ”Measurement of the Relative Jet Energy Scale in CMS with pp Collisions at 7 TeV”, CMS AN-2010/139.

MANGANO, B. et al., 2009, ”Track reconstruction in the CMS Tracker”, The CMS Collaboration CMS-PAS-TRK-09-001.

NAKAMURA,K. and PARTICLE DATA GROUP, 2010, ”Review of Particle Physics”, J. Phys. G: Nucl. Part. Phys. 37 075021.

NARISON,S., 2004, ”QCD as a Theory of Hadrons: From Partons to Confinement”, Cambridge University Press.

NASON,P., 2001, ”Introduction to QCD”, http://cp3wks05.fynu.ucl.ac.be/twiki/pub/Physics/QCDUCL/nason.pdf.

NIKITENKO,A., et al., 2009, ”The Jet Plus Tracks Algorithm”, The CMS Collaboration CMS-PAS-JME-09-002

NOVAES, S.F., 2000, ”Standard Model: An Introduction”, arXiv-hep-ph:0001283v1.

OZTURK,S. et al, 2009, ”Plans to Search for New Particles Decaying to Dijets in pp Collisions at 10 TeV”, CMS AN-2009/070.

PANDOLFI,F., et al., 2010, ”Jet Response and Resolution Measurement with Photon+Jet Events at 7 TeV”, CMS AN-2010/141.

PETRUKHIN,A., 2010, ”Structure Function Measurements at HERA”, arXiv-hep-ex:1005.5612v1.

RANDALL,L. and SUNDRUM,R., 1999, ”Large Mass Hierarchy from a Small Extra Dimension”, Phys.Rev.Lett. 83 3370.

SALAM,G.P. and SOYEZ.,G., 2007, ”A practical Seedless Infrared-Safe Cone jet algorithm”, arXiv-hep-ph:0704.0292v2 and JHEP 0705:086,2007.

SALAM,G.P., 2007, ”A Practical Seedless Infrared Safe Cone Algorithm”, arXiv-hep-ph:0705.2696v1.

__________, 2010, ”Towards Jetography”, arXiv-hep-ph:0906.1833v2.

SCHIEFERDECKER,P., 2008, ”Performance of Jet Algorithms in CMS”, The CMS Collaboration CMS-PAS-JME-07-003.

SIMMONS, E.H., 1997, ”Coloron phenomenology”, Phys. Rev. D 55, 1678Ğ1683 (1997).

SJOSTRAND,T., MRENNA,S. and SKANDS,P., 2006, ”PYTHIA 6.4 Physics and Manual”, JHEP 0605:026,2006 and arXiv-hep-ph:0603175v2.

ZIELINSKI,M., et al., 2010, ”Jet Performance in pp Collisions at 7 TeV”, The CMS Collaboration CMS-PAS-JME-10-003.

CURRICULUM VITAE

I was born on January 23, 1982, in Malatya, Turkey. I finished my high school education in Malatya, 1999. I received my Bachelor's degree in Physics in 2003 from Eskişehir Osmangazi University. I got the my master degree in High energy physics from Çukurova University in 2007 and I started my PhD. study at the same year. I have been working in Çukurova University as a research and teaching assistant since 2006. I am married and I have a daughter.

APPENDIX

A. Model Cross Sections

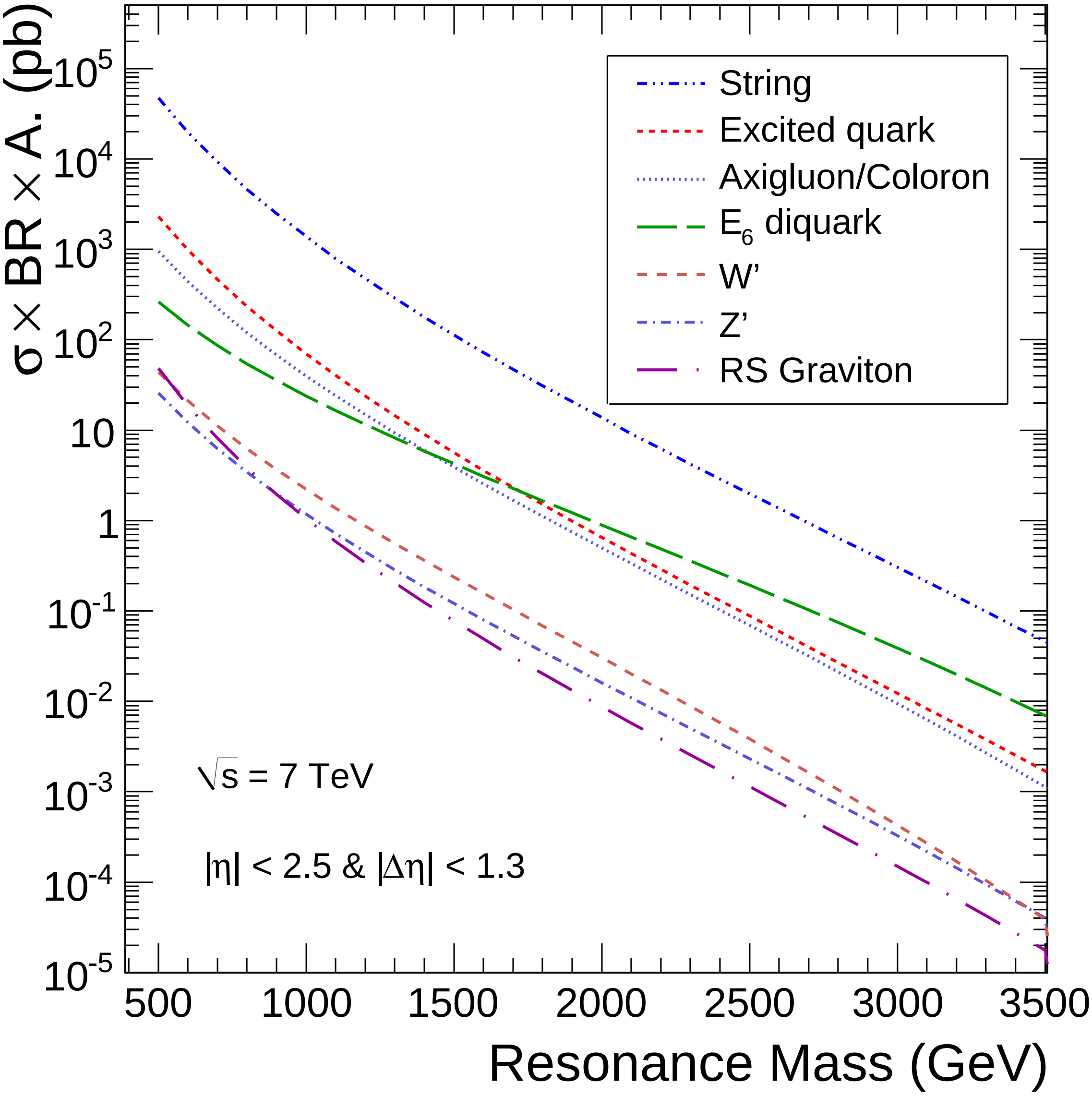

Figure A.1. Cross section for dijet resonances in pp collisions at $\sqrt{s} = 7$ TeV from the lowest order calculation with the eta cuts $|\Delta\eta| < 1.3$ and $|\eta| < 2.5$ on the two jets.

Mass (GeV)	S (pb)	q^* (pb)	A or C (pb)	D (pb)	Z' (pb)	W' (pb)	G (pb)
500.0	0.4700E+05	0.2294E+04	0.9568E+03	0.2623E+03	0.2555E+02	0.4380E+02	0.4828E+02
600.0	0.1974E+05	0.9871E+03	0.4395E+03	0.1451E+03	0.1211E+02	0.2125E+02	0.1862E+02
700.0	0.9304E+04	0.4657E+03	0.2215E+03	0.8646E+02	0.6246E+01	0.1120E+02	0.8100E+01
800.0	0.4627E+04	0.2355E+03	0.1193E+03	0.5435E+02	0.3427E+01	0.6263E+01	0.3852E+01
900.0	0.2485E+04	0.1257E+03	0.6750E+02	0.3554E+02	0.1969E+01	0.3661E+01	0.1961E+01
1000.0	0.1392E+04	0.7005E+02	0.3967E+02	0.2393E+02	0.1172E+01	0.2212E+01	0.1053E+01
1100.0	0.7879E+03	0.4039E+02	0.2400E+02	0.1648E+02	0.7171E+00	0.1372E+01	0.5905E+00
1200.0	0.4731E+03	0.2394E+02	0.1486E+02	0.1154E+02	0.4486E+00	0.8673E+00	0.3426E+00
1300.0	0.2901E+03	0.1452E+02	0.9370E+01	0.8194E+01	0.2857E+00	0.5568E+00	0.2044E+00
1400.0	0.1776E+03	0.8982E+01	0.5998E+01	0.5877E+01	0.1845E+00	0.3616E+00	0.1248E+00
1500.0	0.1119E+03	0.5645E+01	0.3887E+01	0.4249E+01	0.1206E+00	0.2369E+00	0.7770E-01
1600.0	0.7212E+02	0.3596E+01	0.2544E+01	0.3090E+01	0.7961E-01	0.1562E+00	0.4911E-01
1700.0	0.4707E+02	0.2317E+01	0.1678E+01	0.2258E+01	0.5295E-01	0.1034E+00	0.3145E-01
1800.0	0.3106E+02	0.1507E+01	0.1115E+01	0.1656E+01	0.3545E-01	0.6872E-01	0.2036E-01
1900.0	0.2060E+02	0.9889E+00	0.7442E+00	0.1217E+01	0.2386E-01	0.4572E-01	0.1330E-01
2000.0	0.1382E+02	0.6531E+00	0.4988E+00	0.8953E+00	0.1611E-01	0.3043E-01	0.8743E-02
2100.0	0.9117E+01	0.4338E+00	0.3354E+00	0.6591E+00	0.1092E-01	0.2023E-01	0.5781E-02
2200.0	0.6244E+01	0.2896E+00	0.2260E+00	0.4852E+00	0.7413E-02	0.1342E-01	0.3840E-02
2300.0	0.4238E+01	0.1940E+00	0.1525E+00	0.3569E+00	0.5039E-02	0.8884E-02	0.2559E-02
2400.0	0.2881E+01	0.1304E+00	0.1030E+00	0.2622E+00	0.3426E-02	0.5859E-02	0.1708E-02
2500.0	0.1973E+01	0.8782E-01	0.6949E-01	0.1922E+00	0.2329E-02	0.3847E-02	0.1142E-02
2600.0	0.1367E+01	0.5925E-01	0.4684E-01	0.1406E+00	0.1580E-02	0.2513E-02	0.7635E-03
2700.0	0.9342E+00	0.4002E-01	0.3152E-01	0.1025E+00	0.1070E-02	0.1632E-02	0.5101E-03
2800.0	0.6449E+00	0.2704E-01	0.2116E-01	0.7449E-01	0.7231E-03	0.1053E-02	0.3402E-03
2900.0	0.4450E+00	0.1828E-01	0.1415E-01	0.5392E-01	0.4867E-03	0.6744E-03	0.2264E-03
3000.0	0.3040E+00	0.1234E-01	0.9428E-02	0.3885E-01	0.3261E-03	0.4287E-03	0.1501E-03
3100.0	0.2120E+00	0.8329E-02	0.6250E-02	0.2786E-01	0.2174E-03	0.2702E-03	0.9913E-04
3200.0	0.1439E+00	0.5613E-02	0.4119E-02	0.1987E-01	0.1440E-03	0.1688E-03	0.6512E-04
3300.0	0.9920E-01	0.3776E-02	0.2698E-02	0.1408E-01	0.9477E-04	0.1044E-03	0.4253E-04
3400.0	0.6700E-01	0.2535E-02	0.1754E-02	0.9920E-02	0.6190E-04	0.6403E-04	0.2759E-04
3500.0	0.4624E-01	0.1698E-02	0.1131E-02	0.6938E-02	0.4007E-04	0.3886E-04	0.1775E-04
3600.0	0.3136E-01	0.1135E-02	0.7222E-03	0.4815E-02	0.2570E-04	0.2335E-04	0.1133E-04
3700.0	0.2140E-01	0.7559E-03	0.4568E-03	0.3315E-02	0.1631E-04	0.1390E-04	0.7157E-05
3800.0	0.1415E-01	0.5021E-03	0.2858E-03	0.2261E-02	0.1024E-04	0.8199E-05	0.4475E-05
3900.0	0.9559E-02	0.3325E-03	0.1767E-03	0.1528E-02	0.6349E-05	0.4796E-05	0.2766E-05
4000.0	0.6426E-02	0.2195E-03	0.1079E-03	0.1022E-02	0.3889E-05	0.2787E-05	0.1689E-05

Table A.1. Cross section for dijet resonances in pp collisions at $\sqrt{s} = 7$ TeV from the lowest order calculation with the eta cuts $|\Delta\eta| < 1.3$ and $|\eta| < 2.5$ on the two jets. The models are String Resonances (S) as described in this note and Excited Quark (q*), Axigluon or Coloron (A or C), E_6 diquark (D), Z', W' and Randall-Sundrum Graviton (G).

B. Resonance Shapes

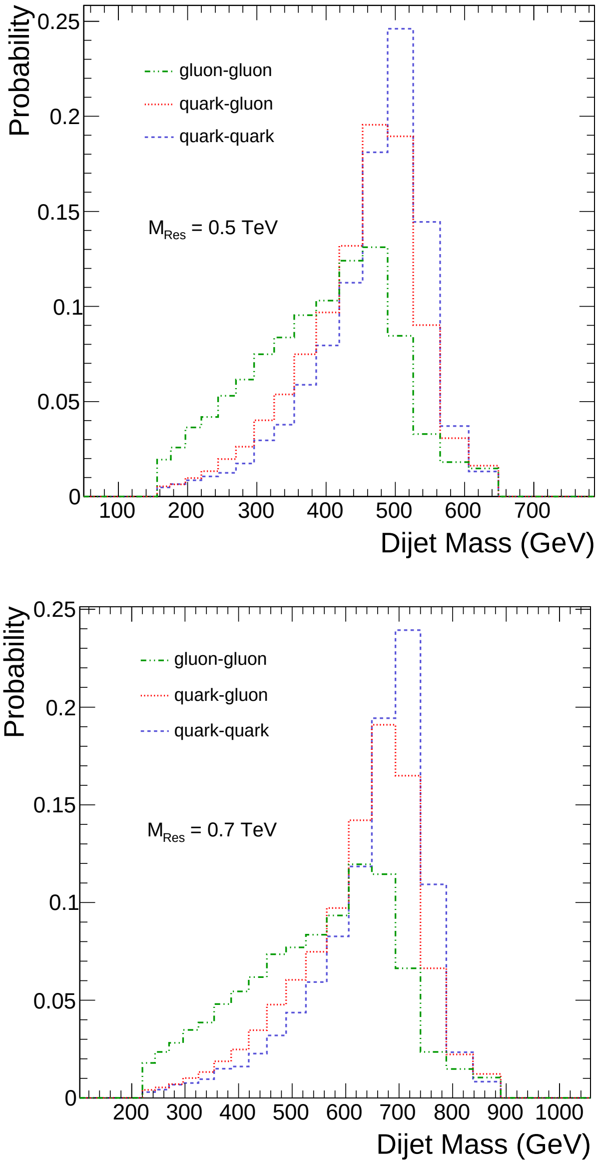

Figure B.1. Dijet mass distribution for $q\bar{q}$ (qq), qg and gg resonances at 0.5, 0.7 TeV resonance mass.

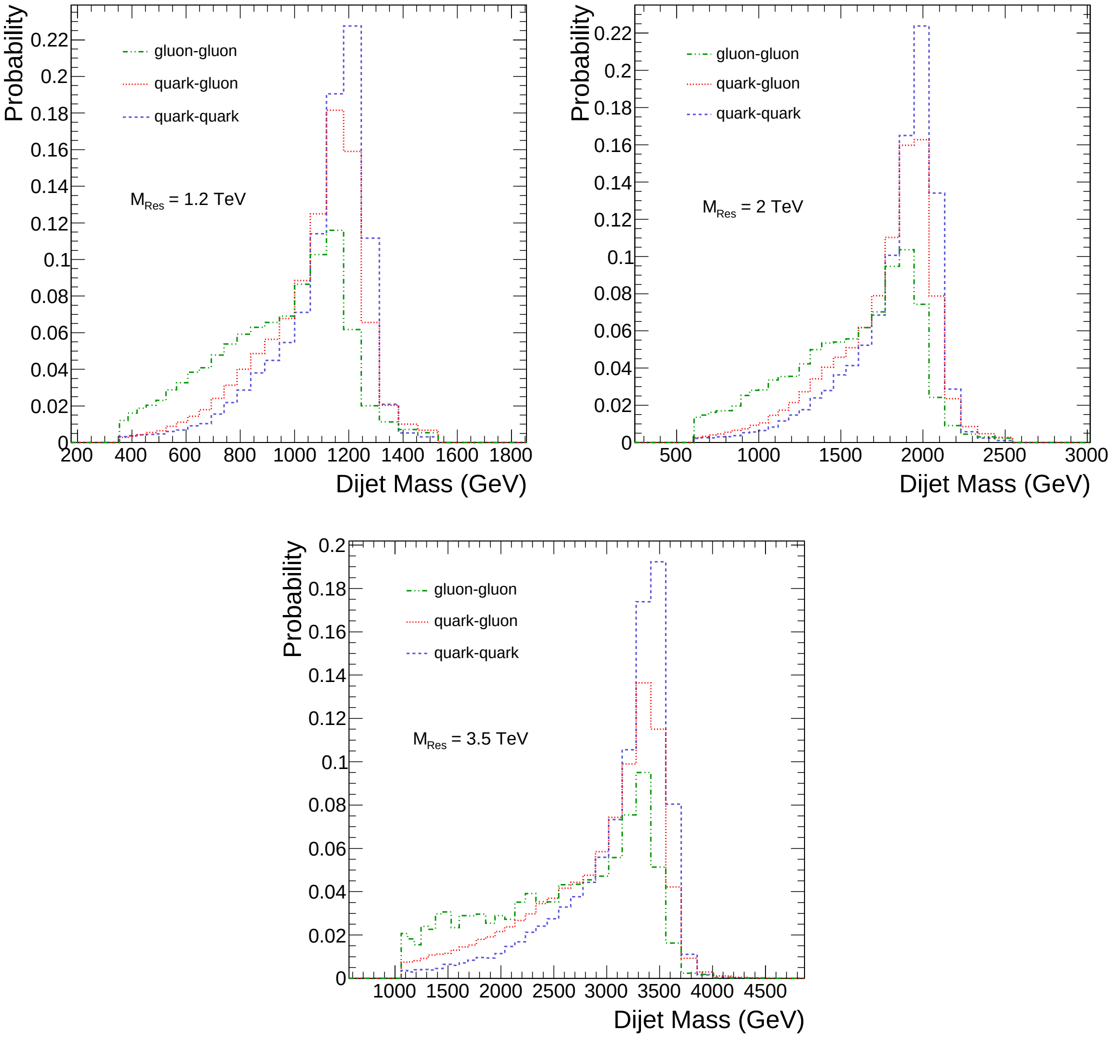

Figure B.2. Dijet mass distribution for $q\bar{q}$ (qq), qg and gg resonances at 1.2, 2 and 3.5 TeV resonance mass.

C. Interpolation Technique

The resonance shape at resonance mass values between the generated values are obtained using an interpolation technique. First, a new parameter is defined as $x = \frac{M_{jj}}{M_{Res}}$ where M_{jj} is dijet mass and M_{Res} is resonance mass. Then the x distribution is generated of any resonance mass between generated Monte Carlo resonance masses. Finally for resonances of mass M between generated samples for resonances of mass M_1 and M_2, the equation

$$Prob_M(x) = Prob_{M_1}(x) + \left[Prob_{M_2}(x) - Prob_{M_1}(x)\right] \cdot \frac{M - M_1}{M_2 - M_1} \tag{C.1}$$

is applied. For example, If we want to generate the x distribution of resonances with a mass at 1 TeV, we use the equation below. Since 1 TeV is between 0.7 TeV and 1.2 TeV, the MC samples were used masses at 0.7 TeV and 1.2 TeV. It gives the probability in each x bins of mass at 1 TeV.

$$Prob_{1TeV}(x) = Prob_{0.7TeV}(x) + \left[Prob_{1.2TeV}(x) - Prob_{0.7TeV}(x)\right] \cdot \frac{1 - 0.7}{1.2 - 0.7} \tag{C.2}$$

Finally, the x distribution was converted to variable dijet mass bins using interpolation technique to get the resonance shape at any resonance mass. A C++ function has been written for this purpose and it can be seen in the below link. This function returns the probability at a given value of resonance mass and dijet mass.

`http://cmssw.cvs.cern.ch/cgi-bin/cmssw.cgi/UserCode/Sertac/DijetResonance/HeaderFiles/Quark_Gluon/QstarBinned_qg.h?revision=1.1&view=markup&pathrev=MAIN`

D. Posterior Probability Densities

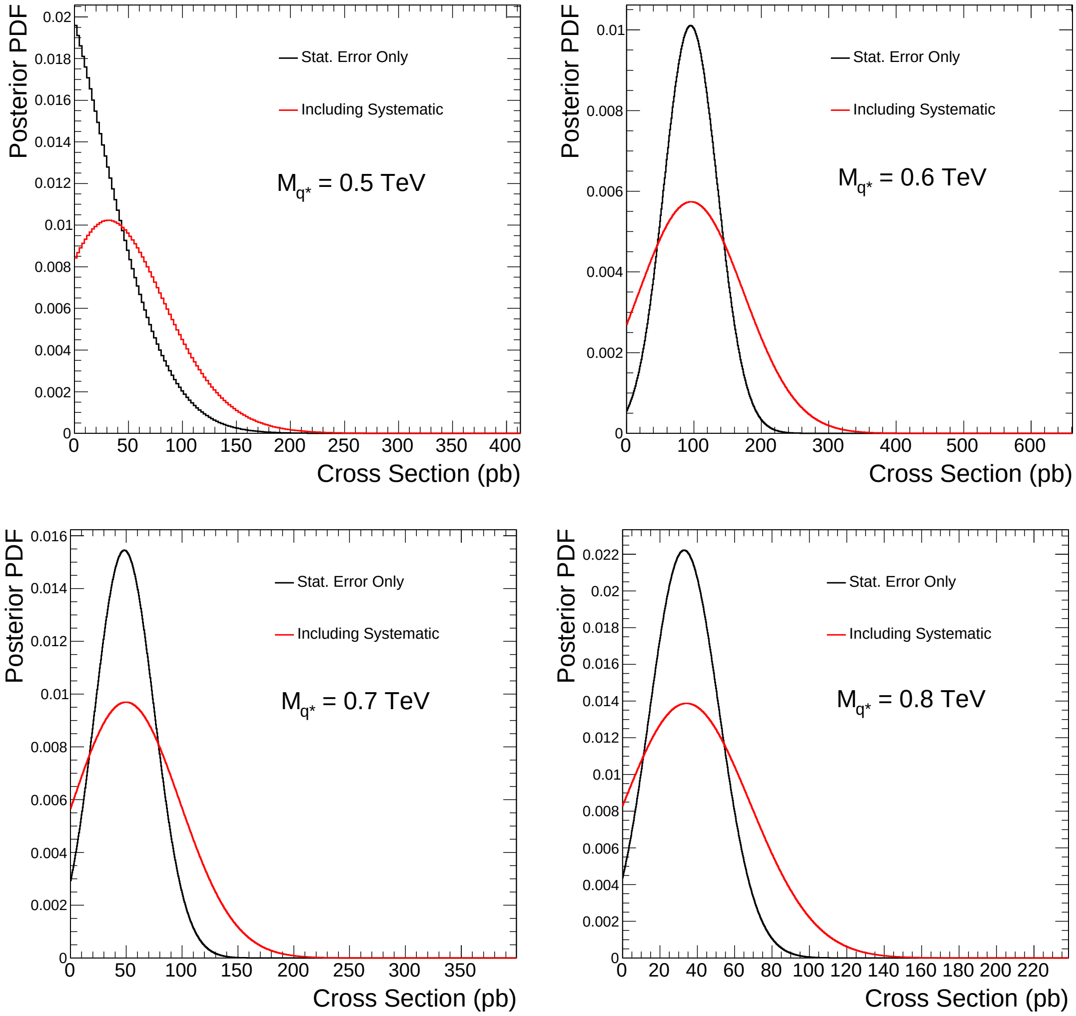

Figure D.1. Posterior probability densities at various excited quark resonance masses. Black histogram includes statistical uncertainties only, red histogram includes both statistical and systematic uncertainties.

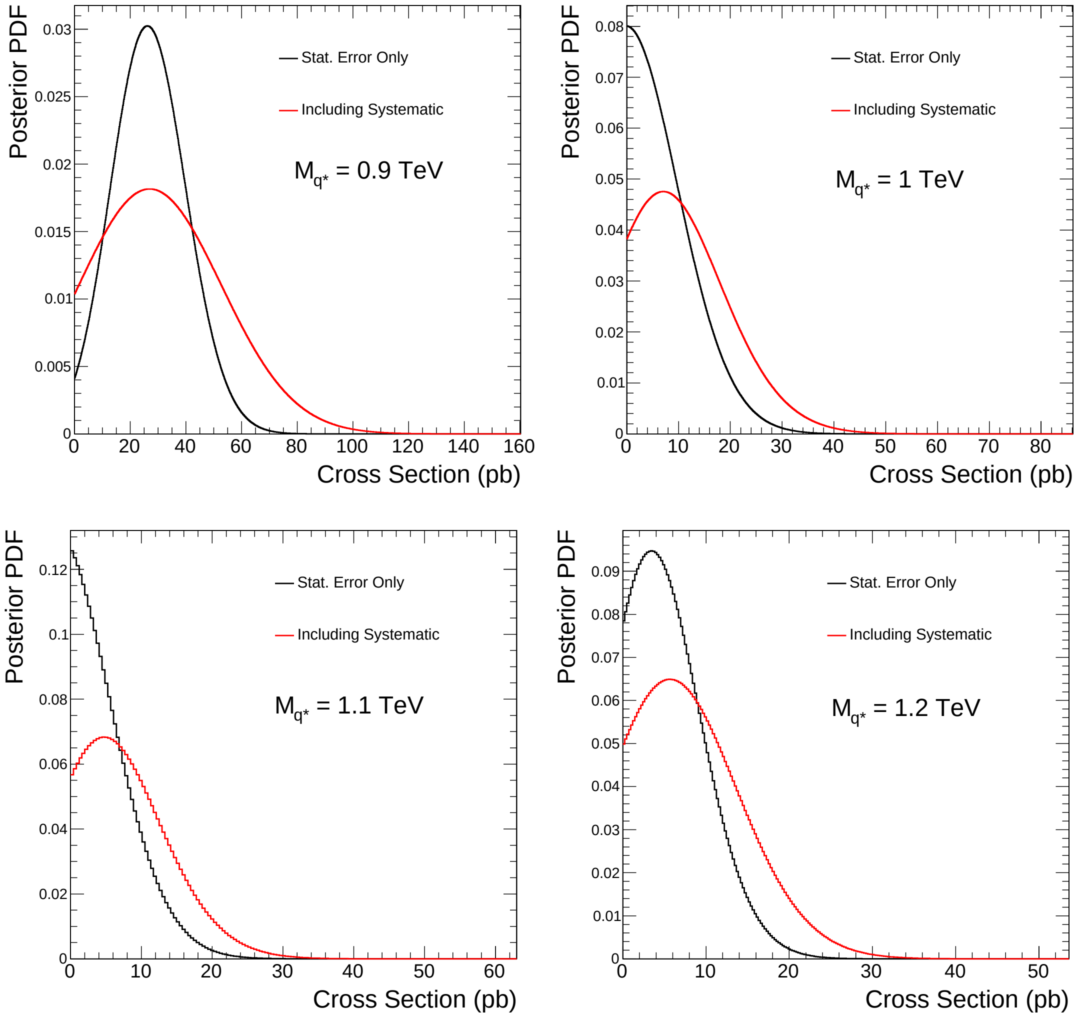

Figure D.2. Posterior probability densities at various excited quark resonance masses. Black histogram includes statistical uncertainties only, red histogram includes both statistical and systematic uncertainties.

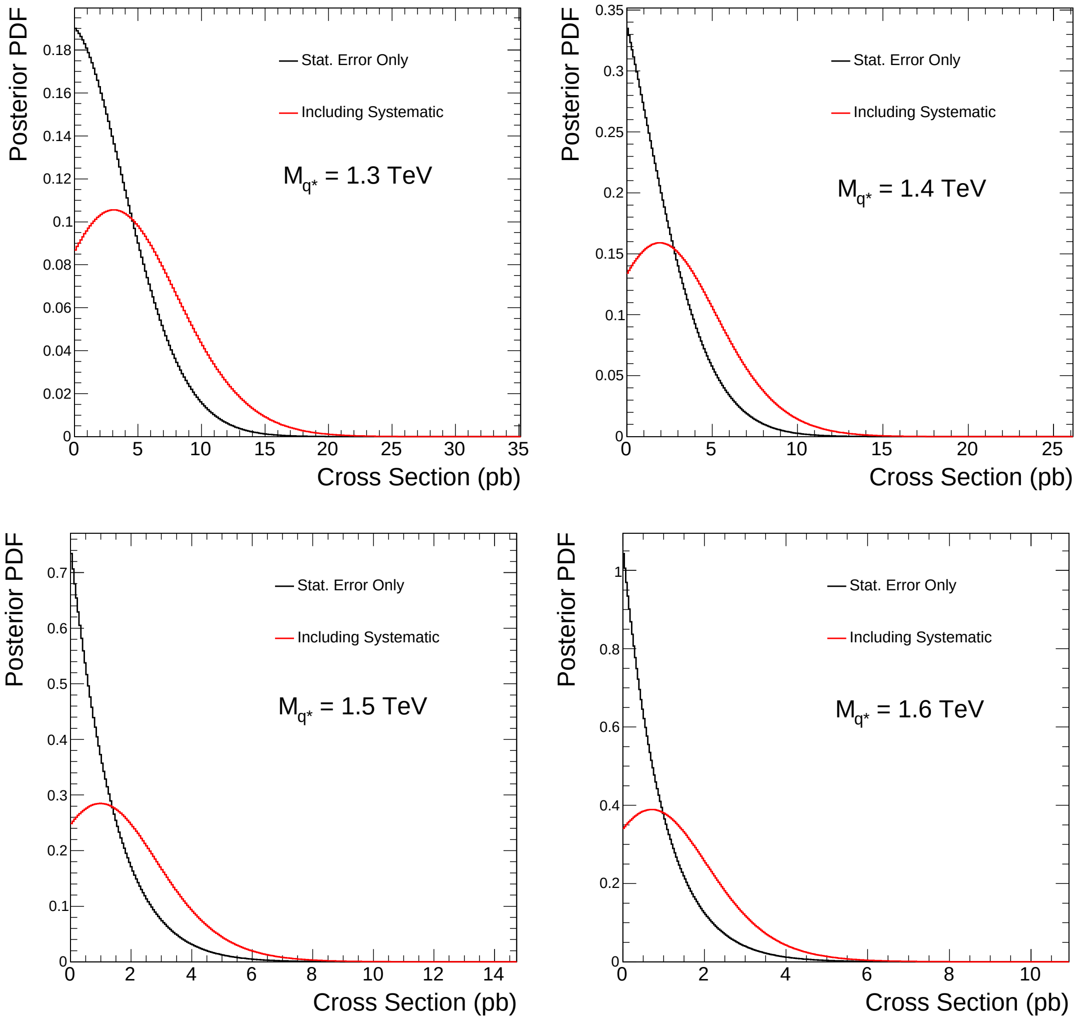

Figure D.3. Posterior probability densities at various excited quark resonance masses. Black histogram includes statistical uncertainties only, red histogram includes both statistical and systematic uncertainties.

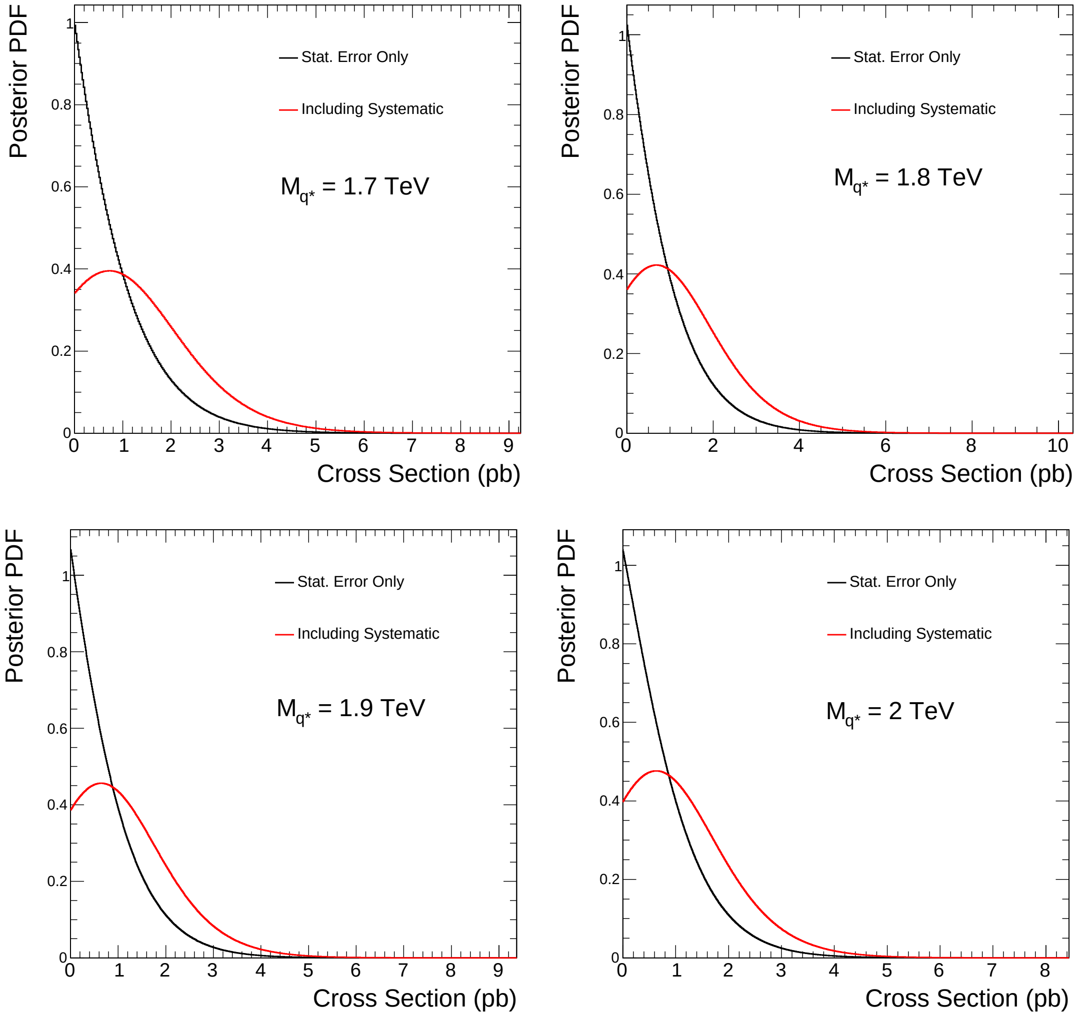

Figure D.4. Posterior probability densities at various excited quark resonance masses. Black histogram includes statistical uncertainties only, red histogram includes both statistical and systematic uncertainties.

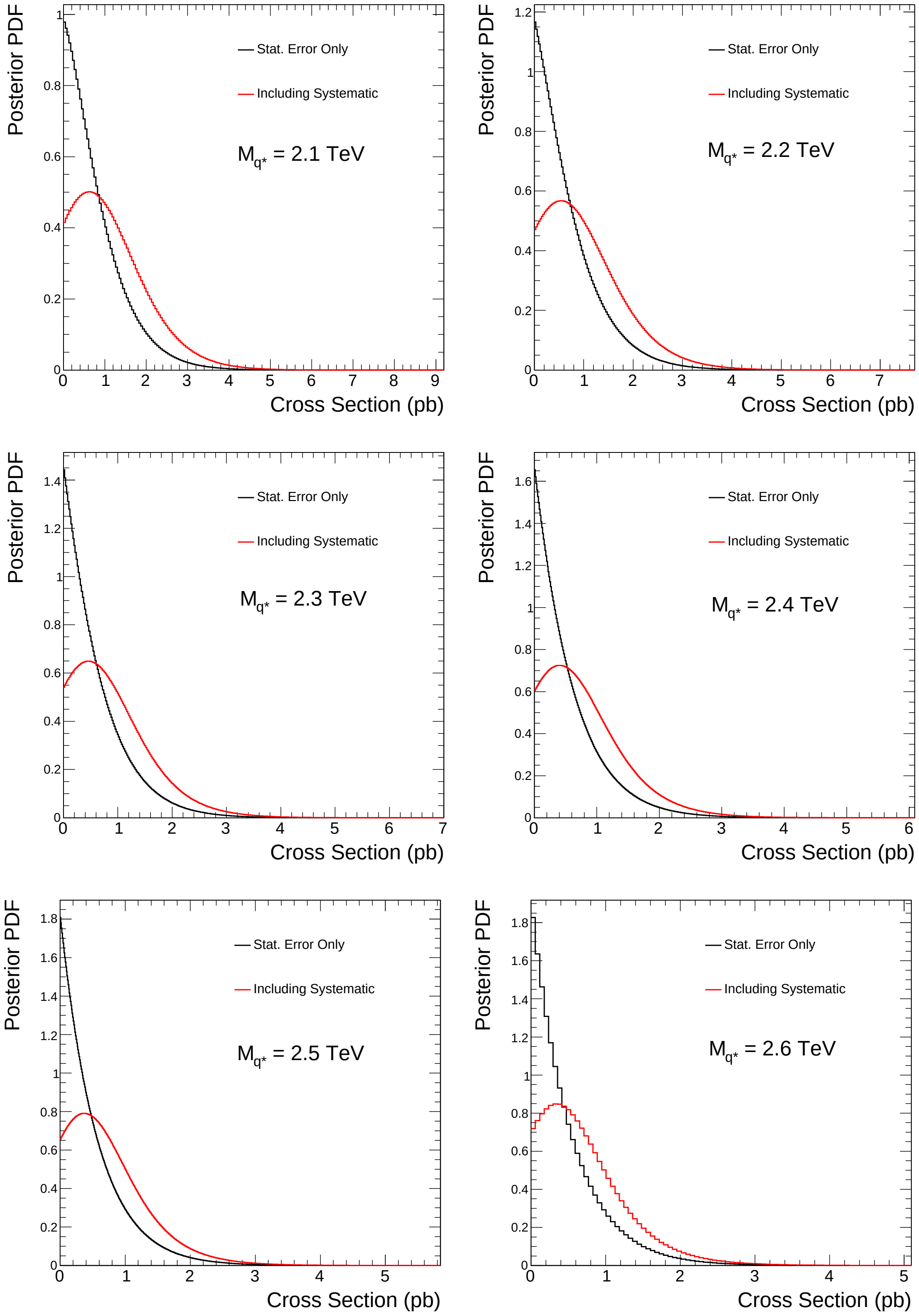

Figure D.5. Posterior probability densities at various excited quark resonance masses. Black histogram includes statistical uncertainties only, red histogram includes both statistical and systematic uncertainties.

E. Error Propagation

Basically, error is an uncertainty in a measurement or distribution. The Poisson distribution applies to a wide range of phenomena in the sciences. It describes the probabilities inherent when an event occurs with a constant probability per unit time. Poisson distribution is given by

$$P(n,N) = \frac{n^N e^{-n}}{N!} \tag{E.1}$$

where n is the average number of events obtained over many repeated trial intervals, N is the number of events which occur during a particular trial interval. For each n value, sum of all probabilities is equal to 1. It should be emphasized that the Poisson distribution is not a continuous function, but rather gives the probabilities for discrete values of N. If n becomes a large number, the Poisson distribution asymptotically approaches a Gaussian density function which is given by

$$G(n,N) = \frac{1}{\sqrt{2\pi n}} e^{[-(N-n)^2/2n]} \tag{E.2}$$

For n is usually 25 or more, the Poisson distribution approaches the normal or Gaussian distribution. Thus, Poisson uncertainties are used in each dijet mass bin, i, where n_i is less than 25, and Gaussian uncertainties are used where n_i is equal or greater than 25.

For Gaussian distributed n, the error is defined $\sigma = \sqrt{n}$. For the case of Poisson distributed n, the upper and lower limits on the mean value ν are given by (Nakamura, 2010)

$$\nu_{lo} = \frac{1}{2} F^{-1}_{\chi^2}(\alpha_{lo}; 2n), \tag{E.3}$$

$$\nu_{up} = \frac{1}{2} F^{-1}_{\chi^2}(1-\alpha_{up}; 2(n+1)), \tag{E.4}$$

where the upper and lower limits are at confidence levels of $1-\alpha_{lo}$ and $1-\alpha_{up}$ respectively. For central confidence intervals at confidence level (%68.822), $1-\alpha$, set $\alpha_{lo}=\alpha_{up}=\alpha/2=0.3173/2$.

The functions for error propagation in the analysis code can be seen below.

```
double getLowerError(double n)
{
   double a = 0.3173/2;
   if (n>=25) return sqrt(n);
   else return n-0.5*TMath::ChisquareQuantile(a,2*n);
}
```

```
double getUpperError(double n)
{
   double a = 0.3173/2;
   if (n>=25) return sqrt(n);
   else return 0.5*TMath::ChisquareQuantile(1-a,2*(n+1))-n;
}
```